

OPTIMISATION OF THE GUIDED WAVE TECHNOLOGY FOR
INSPECTION AND HEALTH MONITORING OF POLYMER MATRIX
COMPOSITES

by

KENA RACHEL JOLLEY

A thesis submitted to the University of Birmingham for the degree of DOCTOR
OF PHILOSOPHY

School of Engineering
Department of Metallurgy
and Materials
University of Birmingham
August 2018

UNIVERSITY OF
BIRMINGHAM

University of Birmingham Research Archive

e-theses repository

This unpublished thesis/dissertation is copyright of the author and/or third parties. The intellectual property rights of the author or third parties in respect of this work are as defined by The Copyright Designs and Patents Act 1988 or as modified by any successor legislation.

Any use made of information contained in this thesis/dissertation must be in accordance with that legislation and must be properly acknowledged. Further distribution or reproduction in any format is prohibited without the permission of the copyright holder.

Abstract

Polymer Matrix Composites (PMCs) are widely used in weight sensitive sectors (such as aircraft and wind turbine blades) where sudden failure of the structures can have a significant impact on the economy and more importantly, can cause life threatening situations. PMCs fail due to various defects, which can arise during the manufacturing stage and can continue growing during the component's service life until its often unexpected failure.

Delaminations are the most common defects in fibre-composites and several Non-destructive testing (NDT) techniques are available for their detection, however they generally require having access to all parts of the components to guarantee defect detection. The Guided Wave Testing (GWT) method can be used to inspect the component without requiring access to all that component however, it still needs further development before it can be accepted as a standard inspection and health monitoring technique for PMCs.

The main goal of this thesis is to assess the defect detection capability of GWT for delamination and especially during three-point loading by validating experimental protocols designed for a specific GFRP sample. One of these protocols will also help to identify the potential precursors or warning signs of an imminent failure in composites.

Acknowledgments

All my praises to my Lord Jesus-Christ without who I could not have reached this milestone in my life. Thank you for giving me Love, Strength, and Faith each single day.

I would like to thank my parents, Yvette Blandine Massamba-Ndilou and Benjamin Makaya for teaching me to be strong and to never give up. I love you both more than you can ever imagine. I would like to thank my fiancé Ashley Jolley, who supported me all these years and showed a great deal of patience – thank you for your everlasting love. I also would like to thank the entire Nkounkou and Makaya families, particularly my brothers, sisters: Freddy, Franck, Magaly, Rinala, and Aymard.

I would like to thank both my academic and industrial supervisors, Professor Claire Davis and Mr Peter Mudge, for their guidance, advice, positivity and encouragements throughout this entire PhD.

This thesis was copy edited for conventions of language, spelling and grammar by Professor Claire Davis and Dr Alexander Haig.

I would like to give a very special thanks to:

- Dr Bhavin Engineer for coaching me on a daily basis the past few years to push me to complete this thesis.
- Dr Alexander Haig who took over Bhavin's coaching, gave me precious advice, especially on how to handle stress during the writing-up period.
- Dr Shehan Lowe, for teaching me on how to use the laser vibrometer and for helping me over the phone during my very late nights and weekends in the laboratory.

I would like to thank my very own A-team for the endless mental support and for boosting my mood when I needed it the most: Dorothee, Kamer, Matthew, Hugo, Shiva and Sina.

And finally, I would like to thank the Engineering and Physical Sciences Research Board (EPSRC), the University of Birmingham and TWI Ltd for giving me the opportunity to carry out this PhD.

Contents

Chapter 1: INTRODUCTION	1
1.1 Industry needs.....	2
1.2 Survey of Non-Destructive Testing methods for composites	3
1.3 Summary.....	8
1.4 Industrial NDT approaches for composites	9
1.5 Thesis objectives.....	10
Chapter 2: BACKGROUND KNOWLEDGE ON POLYMER MATRIX COMPOSITES AND GUIDED WAVE TESTING.....	12
2.1 Background information on PMC	13
2.1.1 Introduction.....	13
2.1.2 Matrix and reinforcement.....	13
2.1.3 The interface.....	15
2.1.4 Manufacturing processes	16
2.1.5 Elasticity principles.....	17
2.1.6 Polymer Matrix Composites defects and failure modes.....	21
2.1.7 Key industry sectors for Polymer Matrix Composites.....	22
2.2 Background information on Guided Wave Testing.....	23
2.2.1 Ultrasonic Testing.....	23
2.2.2 Guided Wave Testing.....	26
2.2.3 Dispersion curves.....	28
2.2.4 Testing method	32
2.2.5 GWT applications	33
Chapter 3: LITERATURE REVIEW	35
3.1 The propagation of ultrasonic waves in non-defective composites	36
3.2 Sensors, actuators and transducers	37
3.2.1 Piezoelectricity	37
3.2.2 Polarisation	37
3.2.3 Sensors	39
3.2.4 Actuators.....	39
3.2.5 Transducers	40
3.2.6 Typical applications	40
3.3 Baseline subtraction approaches to damage detection	40
3.4 Composite defect detection based solely on the transmitted S_0 mode	42
3.4.1 Detection via the amplitude and velocity of the transmitted S_0 mode.....	42
3.4.2 Detection via the conversion of the S_0 mode.....	45
3.4.3 Detection via the reflection of the S_0 mode.....	48
3.5 Composite defect detection based solely on the transmitted A_0 mode.....	49

3.6	Composite defect detection based on the S_0 and A_0 wave modes transmitted at once.....	55
3.6.1	Monitoring of elastic moduli reconstructed from the S_0 and A_0 modes velocities	55
3.6.2	Through-thickness displacement caused by the S_0 and A_0 modes.....	60
3.7	Summary.....	61
Chapter 4: TRANSDUCER DIRECTIONALITY STUDY IN WOVEN GFRP COMPONENTS		63
4.1	Introduction	64
4.2	Experimental protocol	66
4.2.1	Specimen manufacture	66
4.2.2	Scanning Laser Vibrometry for plotting wavenumbers and dispersion curves of a Woven GFRP plate: “ON” and “OFF” fibre signal generation.....	67
4.2.3	Scanner Laser Vibrometry for sensor assessment	69
4.3	Data collection and plotting protocols	71
4.3.1	Wavenumber plots and dispersion curves	71
4.3.2	Sensor assessment.....	74
4.4	Results and discussion	75
4.4.1	Wavenumbers and dispersion curves of a Woven GFRP plate: “ON” and “OFF” fibre signal generation 75	
4.4.2	Sensor assessment.....	85
4.4.3	Performance comparison between the Thickness-shear PZT element, Thickness-shear PZT element with backing mass and MFCs	90
4.5	General discussion	93
4.6	Conclusion	96
Chapter 5: GUIDED WAVE TESTING OF A GFRP CROSS-PLY LAMINATE CONTAINING A DELAMINATION.....		97
5.1	Introduction.....	98
5.2	Experimental protocol	98
5.2.1	Specimen manufacture	98
5.2.2	UltraLAB system for plotting dispersion curves of a Cross-Ply GFRP plate	98
5.2.3	Velocity profile of fundamental Lamb waves in Chapter5_Specimen001	101
5.2.4	MFC frequency response	102
5.2.5	Guided Wave Testing for delamination detection (single excitation frequency)	102
5.2.6	Guided Wave Testing for delamination detection (sweep frequency)	104
5.2.7	Validation technique: Scanning Laser Vibrometry for delamination detection	105
5.3	Results and discussion	106
5.3.1	UltraLAB system for plotting dispersion curves of a Cross-Ply GFRP plate	106
5.3.2	Velocity profile of fundamental Lamb waves in Chapter5_Specimen001	108
5.3.3	MFC frequency response	109
5.3.4	Guided Wave Testing for delamination detection (single excitation frequency)	110
5.3.5	Guided Wave Testing for delamination detection (sweep frequency)	113
5.3.6	Validation technique: Scanning Laser Vibrometry for delamination detection	118
5.4	General discussion	118
5.5	Conclusion	121

Chapter 6: GUIDED WAVE MONITORING OF WOVEN GFRPS UNDER THREE-POINTS LOADING..	123
6.1 Introduction	124
6.2 Experimental protocol	125
6.2.1 Specimen manufacture	125
6.2.2 Scanning Laser Vibrometry pre-loading and pre-damage insertion - Phase One.....	125
6.2.3 Guided wave testing pre-, during and post loading– Phase Two	127
6.2.4 Scanning Laser Vibrometry post loading – Phase Three	130
6.2.5 Validation techniques	130
6.3 Results and discussion	130
6.3.1 Scanning Laser Vibrometry pre-loading and pre-damage insertion - Phase One.....	130
6.3.2 Guided wave testing pre-, during and post loading – Phase Two	132
6.3.3 Baseline subtraction approach to damage detection	138
6.3.4 Scanning Laser Vibrometry post loading – Phase Three	140
6.3.5 Validation techniques	141
6.4 General discussion	144
6.5 Conclusion	147
Chapter 7 CONCLUSION	148
7.1 Thesis Summary and Conclusion.....	149
7.2 Contribution to knowledge.....	151
7.3 Future Work	152
REFERENCES	154
APPENDIX.....	174
Appendix A – Polytec Scanning Vibrometer Instruction.....	175
Appendix B - MFC frequency response for [0/90] ₁₆ GFRP circular plates.....	179
Appendix C - Images of the S ₀ and A ₀ modes interacting with the delamination from Surface B	180

Figures

Figure 1: Plate waves ^[50]	27
Figure 2: Dispersion curves of a $[0/90]_{2s}$ laminate ^[54]	29
Figure 3: An example of hysteresis loop for polarisation of a crystal	38
Figure 4 Experimental protocol for dispersion curves with thickness-shear PZT element	69
Figure 5 (a) Experimental set up for transducer directionality plots; (Thickness-Shear PZT element); (c) Thickness-Shear PZT element with backing mass; (d) M2814-P1 MFC	70
Figure 6: Localised bath acetone	71
Figure 7 A-scans in the Cartesian and Polar coordinates, for signal transmission parallel to the fibres and collected off-fibre direction - 66kHz excitation frequency	73
Figure 8 Data collection diagram for on-fibre (45°) signal excitation	73
Figure 9 Data collection diagram for off-fibre (0°) signal transmission	74
Figure 10 Wavenumber plot at 0° for signal transmission parallel to the fibres (45°).....	75
Figure 11 Wavenumber plot at 10° for signal transmission parallel to the fibres (45°).....	76
Figure 12 Wavenumber plot at 20° for signal transmission parallel to the fibres (45°).....	76
Figure 13 Wavenumber plot at 30° for signal transmission parallel to the fibres (45°).....	76
Figure 14 Wavenumber plot at 40° for signal transmission parallel to the fibres (45°).....	77
Figure 15 Wavenumber plot at 50° for signal transmission parallel to the fibres (45°).....	77
Figure 16 Wavenumber plot at 60° for signal transmission parallel to the fibres (45°).....	77
Figure 17 Wavenumber plot at 70° for signal transmission parallel to the fibres (45°).....	78
Figure 18 Wavenumber plot at 80° for signal transmission parallel to the fibres (45°).....	78
Figure 19 Wavenumber plot at 90° for signal transmission parallel to the fibres (45°).....	78
Figure 20 S_0 (A), A_0 (B), SH_{01} (C), SH_{02} (D) phase velocities from signal transmission parallel to fibres (45°) .	79
Figure 21 Wavenumber plot at 0° for signal transmission off-fibre (Plate X-axis).....	80
Figure 22 Wavenumber plot at 10° for signal transmission off-fibre (Plate X-axis).....	80
Figure 23 Wavenumber plot at 20° for signal transmission off-fibre (Plate X-axis).....	81
Figure 24 Wavenumber plot at 30° for signal transmission off-fibre (Plate X-axis).....	81
Figure 25 Wavenumber plot at 40° for signal transmission off-fibre (Plate X-axis).....	81
Figure 26 Wavenumber plot at 50° for signal transmission off-fibre (Plate X-axis).....	82
Figure 27 Wavenumber plot at 60° for signal transmission off-fibre (Plate X-axis).....	82
Figure 28 Wavenumber plot at 70° for signal transmission off-fibre (Plate X-axis).....	82
Figure 29 Wavenumber plot at 80° for signal transmission off-fibre (Plate X-axis).....	83
Figure 30 Wavenumber plot at 90° for signal transmission off-fibre (Plate X-axis).....	83
Figure 31 S_0 (A), A_0 (B), SH_{01} (C), SH_{02} (D) phase velocities from signal transmission off fibres (X-Axis).....	84
Figure 32 S_0 mode directionality from signal transmission parallel to fibres at 66 kHz (A&B) and 130 kHz (C&D) – PZT element.....	86
Figure 33 A_0 mode directionality from signal transmission parallel to fibres at 66 kHz (A&B) and 130 kHz (C&D) – PZT element.....	87
Figure 34 S_0 mode directionality from signal transmission parallel to fibres at 66 kHz (A) and 130 kHz (B) – Teletest Transducer	88
Figure 35 A_0 mode directionality from signal transmission parallel to fibres at 66 kHz (A) and 130 kHz (B) – Teletest Transducer	88
Figure 36 S_0 mode directionality from signal transmission parallel to fibres at 66 kHz (A) and 130 kHz (B) - MFC	89
Figure 37 A_0 mode directionality from signal transmission parallel to fibres at 66 kHz (A) and 130 kHz (B) - MFC	89
Figure 38 Comparison of the S_0 mode in- plane displacements between transducers – transmission parallel to fibres (66kHz)	90
Figure 39 Comparison of the SH_{01} modes between transducers – transmission parallel to fibres (66kHz).....	90
Figure 40 Comparison of the S_0 mode out-plane displacement between transducers– transmission parallel to fibres (66kHz)	91
Figure 41 S_0 mode directionality from signal transmission off-fibre at 66 kHz (A) and 130 kHz (B) – PZT element	92
Figure 42 S_0 mode (in-plane)	92
Figure 43 Shear wave SH_{01}	93
Figure 44 S_0 mode (out of plane).....	93
Figure 45 ULTRALAB equipment	99

Figure 46 A-scan with centre frequency of 40 kHz.....	99
Figure 47 A-scan with centre frequency of 50 kHz.....	100
Figure 48 A-scan with centre frequency of 60 kHz.....	100
Figure 49 Experimental setup for directional MFC frequency response.....	102
Figure 50 Experimental setup for series of South-North scans (pitch-catch tests).....	103
Figure 51 MFC coupling method.....	104
Figure 52 Experimental setup for the West-East scan.....	104
Figure 53: Experimental set-up with PSV-400 Laser Vibrometer.....	106
Figure 54 Contour plot for off axis direction 45° - GFRP laminate 0°/90° with no defects.....	107
Figure 55 Dispersion curves for on axis direction 0° - GFRP laminate 0°/90° with no defects.....	107
Figure 56 Comparison between on-fibre and off-fibre propagation of the S ₀ and A ₀ modes.....	107
Figure 57 Comparison between on-fibre and off-fibre propagation of the A ₁ and S ₁ modes.....	108
Figure 58 The S ₀ and A ₀ modes velocities in the defect free GFRP laminate.....	109
Figure 59 MFC frequency response for [0/90] ₁₆ GFRP circular plates.....	109
Figure 60 Peak to peak amplitude variation of the S ₀ mode along 0 mm axis.....	110
Figure 61 Peak to peak amplitude variation of the S ₀ mode at 40mm offset on the left and right side of the paper insert.....	110
Figure 62 Peak to peak amplitude variation of the S ₀ mode at 50mm offset on the left and right side of the paper insert.....	111
Figure 63 Peak to peak amplitude variation of the S ₀ mode at 60mm offset on the left and right side of the paper insert.....	111
Figure 64 Variation of signal amplitude at multiple positions around the defect and at P50 from West to East.....	112
Figure 65 Variation of signal amplitudes at fixed receiving point between P23 and P24 and from West to East.....	113
Figure 66 Amplitude variation of the S ₀ mode around the paper insert for 40 kHz (a) and 80 kHz (b) excitation frequency – <i>Surface A</i>	114
Figure 67 Amplitude variation of the A ₀ mode around the paper insert for 40 and 80 kHz excitation frequency – <i>Surface A</i> ; (a), (b) normalised amplitude scale; (c), (d) enlarged view of (a) and (b).....	115
Figure 68 Amplitude variation of the S ₀ mode around the paper insert for 40 and 80 kHz excitation frequency – <i>Surface B</i>	116
Figure 69 Amplitude variation of the A ₀ mode around the paper insert for 40 and 80 kHz excitation frequency – <i>Surface B</i>	117
Figure 70 Test results from using Vibrometer.....	118
Figure 71 GFRP beams.....	125
Figure 72 Phase One and Phase Three Test Set Up.....	127
Figure 73 Set-up of three-point loading test.....	129
Figure 74 Test results for Beam no.14092/9 for 106 kHz excitation frequency.....	131
Figure 75 Test results for Beam no.14092/11 for 106 kHz excitation frequency.....	131
Figure 76 Test results for Beam no.14092/12 for 106 kHz excitation frequency.....	131
Figure 77 Data collected pre three-point loading – Specimen 14092-25 – 106kHz.....	132
Figure 78 Data collected pre three-point loading – Specimen 14092-25 – 114kHz.....	132
Figure 79 Data collected pre three-point loading – Specimen 14092-25 – 122kHz.....	133
Figure 80 Data collected pre three-point loading – Specimen 14092-25 – 130kHz.....	133
Figure 81 Control Specimen 14092/10 during loading of Specimen 14092/25.....	133
Figure 82 Control Specimen 14092/10 during loading of Specimen 14092/26.....	134
Figure 83 Control Specimen 14092/10 during loading of Specimen 14092/27.....	134
Figure 84 Raw data from Specimen 14092/25 pre loading - 130kHz.....	135
Figure 85 Pre-during-post loading GW data relative S ₀ velocity - 8 mm deflection.....	136
Figure 86 Pre-during-post loading GW data relative SH ₀₂ velocity - 8 mm deflection.....	136
Figure 87 Pre-during-post loading GW data relative SH ₀₁ velocity - 8 mm deflection.....	137
Figure 88 Pre-during-post loading GW data relative A ₀ velocity - 8 mm deflection.....	137
Figure 89 S ₀ Amplitude Drop over Bending.....	138
Figure 90 SH ₀₂ Amplitude Drop over Bending.....	139
Figure 91 SH ₀₁ Amplitude Drop over Bending.....	139
Figure 92 A ₀ Amplitude Drop over Bending.....	139
Figure 93 Vibrometry testing pre three-point loading.....	140
Figure 94 Vibrometry testing post three-point loading for 8 mm deflection.....	141
Figure 95 Visual inspection of specimen 14092/25-26.....	141

Figure 96 Visual inspection of specimen 14092/28-31.....	142
Figure 97 Test set-up for X-ray tomography of Specimen 14092/27 - post loading	143
Figure 98 X-ray tomography results for Specimen 14092/27 - post loading.....	143
Figure 99 Setting Laser to Centre Beam	175
Figure 100 Geometry Scan Point	175
Figure 101 2D alignment step	176
Figure 102 3D alignment step	177
Figure 103 3D alignment Target Quality	177
Figure 104 Defining scan points	178

“Where the mind goes, the man follows”

Interpretation of Proverbs 23:7 (*For as he thinks in his heart, so is he*) by Joyce Meyer

Chapter 1: INTRODUCTION

1.1 Industry needs

Over the past few decades, mechanical engineers have witnessed a significant reduction in the use of metallic structures for applications where weight saving is critical because of the rising popularity of composite materials. The interest in the performance of composites, particularly polymer matrix composites (PMCs), was generated by their significant advantages over metals. One of PMCs' main benefits is their capability to be manipulated during manufacturing processes, in order to deliver products with anisotropic properties along directions targeted by designs. Their other important benefit is their high strength-to-weight ratio, which is a very crucial quality for weight sensitive sectors such as aircraft, aerospace and offshore renewable energy. PMCs also have various disadvantages and one of the most crucial is the wide variety of defects they can experience. These defects can arise during manufacturing or during service and increase the probability of a sudden and catastrophic failure of the structure. Although this is a very important issue, the implementation of these materials has become a priority for many major industries.

Therefore, it is not surprising that the high demand for composites has led to a surge in the development of suitable techniques for successfully inspecting and health monitoring composite components. The inspection of composites requires specialised and advanced techniques because their anisotropic properties make the process of defect detection extremely challenging.

There is a need for reliable and time-efficient inspection and health monitoring techniques to ensure the integrity of large composite structures. The need for inspection not only applies during service, but also pre-service, soon after the manufacturing stage. Such techniques should not only be capable of detecting the presence of defects, but should also provide information on defect size in order to help assess the risk of failure.

1.2 Survey of Non-Destructive Testing methods for composites

Several Non-Destructive Testing (NDT) methods ^[1,2] are currently being used for the inspection of composite parts. Some of these techniques are time-consuming, thus must impact on productivity and profit within high profile industry sectors (such as aerospace, marine and renewable energy). The following NDT methods have been used for testing composite components, but these techniques have some limitations:

Acoustic emission (AE)

The AE technique requires the use of piezoelectric transducers in order to record mechanical “events” which generate elastic stress waves (acoustic waves) in the material. Acoustic waves are generated (i) when a material is under stress (such as tension, compression, torsion, bending or impact), (ii) during growth of an existing defect or (iii) by noise (vibration entering the structure from its environment). One of the greatest challenges facing AE is that of differentiating defect related signals from signals from other sources, particularly noise. It often requires the use of multiple sensors and trilateration methods to determine the source of an event, therefore to dissociate stress waves generated by noise, a defect or negligible changes. Although AE is recommended for Structural Health Monitoring (SHM) ^[1, 2], in most cases it is not suitable for inspection since it must be applied at the time of defect inception or growth. In some cases, an active sensor is needed to generate the stress waves. This technique is called Acousto-Ultrasonics (AU) ^[3, 4]. The receiver (passive sensor) records the first set of data from a healthy sample (or a healthy known area of the component) to use as a baseline signal ^[3] which is afterwards compared with data retrieved from other areas of the material. Data can then be analysed using AE-based signal processing methods. Breaking the lead pencils on the component surface can also be used as an active known source to generate stress waves in the

material under inspection, which is a method often used in AE for calibration. This technique is called the pencil-lead break test ^[1, 5 -6].

Thermography

Thermography is based on the principle that each component's feature possesses a specific thermal signature. Therefore, the technique produces images which depict the overall thermal condition of the component under investigation. It can involve observing the heating or cooling of the component under test with a thermal camera and the identification of areas with anomalous characteristics. It was reported ^[7] that thermography was not suitable for detecting manufacturing defects (such as inclusion, porosity) and was more appropriate to finding defects such as cracks and impact damage. The application is limited to very thin structures, reportedly ^[1] up to 8 mm thick approximately.

Electrostatic technique

During the fabrication of a composite material, interdigitated sensors ^[8] can be used to monitor the curing process. The sensors allow measurement of the capacitance of the material, which is proportional to the dielectric permittivity (ϵ') of the resin matrix. Elevated curing temperatures will increase the viscosity of the resin matrix, which in turn will cause the material conductivity to drop, decreasing the dielectric permittivity of the resin matrix ^[2]. This technique is called the *dielectric testing method* and can further be used to (i) assess the quality of an adhesive bond between components and (ii) monitor the ageing process of the bond, which can be accelerated by water absorption ^[2]. Dielectric measurement methods are limited to electrically conductive composites (honeycomb sandwich structures and Carbon Fibre Reinforced Polymer – *CFRP* - laminates).

Microwave and radio wave methods

Another method of assessing the quality of a bond by measuring permittivity is to transmit microwaves (0.3-300GHz)^[2, 7] into the material. The microwave technique is reported^[2] to be most suited for the inspection of Glass Fibre Reinforced Polymers (GFRPs) rather than CFRPs. The Ground Penetrating Radar (GPR) is another recognised method for testing low-conductive materials such as CFRPs. Originally the technique was developed for geology^[9] but it has now been used for testing composites by transmitting and receiving radio waves (0.015-2.5GHz)^[2,9].

Electromagnetic methods

The Eddy current technique consists in using coils to create an electromagnetic field in the material being tested. Defects create a change of impedance in a material which in turn will affect the impedance of a receiving coil^[2, 10] located in the proximity of the component. The electromagnetic method can only be applied to CFRPs which are conductive enough for the technique to be used^[5].

Tap Testing

Tap testing is reportedly^[9,11] the most widely used NDT technique for testing composite aircraft structures. The method consists of listening to the response of a material after it has been impacted with a hammer, which generates sound in the audible frequency range (10-20Hz). Therefore, the structure has to be located in an isolated area to enable the inspector to detect the defects (delamination and disbonds only) whose presence will be indicated by a hollow sound^[2, 10]. Over the years, the technique has evolved to a more advanced stage where a special tool fitted with a sensor is used to record the response of the material to impact (digital tap testing). The technique has been claimed^[5,11] to be limited to very thin components (no more than 1 mm thick or up to 4 plies), and is highly recommended for the inspection of honeycomb structures.

Mechanical impedance testing

The mechanical impedance method is mainly used for testing honeycomb structures for the detection of (i) disbonds between panels (or skins) and the honeycomb (or core of the structure) and (ii) delaminations in the skin. An impedance probe is mounted on an X-Y scanning system [2,12] to produce a C-scan image of the honeycomb structure. The existence of a defect is confirmed by a decrease of the recorded resonance frequencies. Cawley [12] reported that the sensitivity of the method is linked to the thickness of the honeycomb (the technique is not recommended for sandwich structures with skins thinner than 10mm).

Leak Testing

This method was primarily designed to test closed containers of fluids (gas and liquids) to detect leakage but it can now be applied to open components, as long as they are sprayed first with a tracer fluid (gas or penetrant liquid) and then placed in a pressure chamber [1]. Several different methods have been used to detect leakage and their rate. A leak can be detected by (i) immersing a composite structure in a specific liquid or inserting the component in vacuum box, after the component has been covered with a specific solution (bubble leak testing)^[1, 13], (ii) pressuring the fluid (water, chemicals, halogen gas, helium or hydrogen) inside the closed component. The leak testing methods^[1, 14-16] respectively for the fluids previously mentioned are: hydrostatic, chemical penetrant, halogen gas, mass spectrometer and thermal conductivity. Leakages can be indicated by (i) outside reaction of the escaping fluid with a chemical agent or (ii) using an automated device (for the mass spectrometry^[15] and thermal conductivity^[1, 16] only). The leakage of a fluid will certainly emit noise; therefore, passive NDT techniques such as AE can also be used as a screening method as demonstrated by Holland^[17] who reported the development of a passive PZT sensor, for the detection of air leak from spacecraft. Leak testing methods are limited to the detection of leaks only rather than internal defects^[1].

Radiography

Radiography consists of scanning a component with X-rays to produce a 2D image for the visualisation of defects (such as voids) affecting the density ^[5,11] of the material under inspection. Because these defects need to be as parallel as possible to the X-ray beam, the technique is reportedly ^[1,5,11] insensitive to delaminations, which are common defects in polymer matrix composites. The main downside of this technique is the endangerment of the operators caused by the use of X-rays. Alternatively, Computed Tomography (CT) can be used to generate a 3D image of the inside of the component, rather than the 2D image produced by basic radiographic inspection. It was reported ^[1] that CT was time consuming, costly and not suitable for large area coverage.

Shearography

The shearography method uses interferometry principles to detect anomalies such as residual stress ^[18] in composite components subjected to load variability. The results (highly dependent on the material surface condition ^[1]) are images describing axisymmetric fringe patterns called *speckle patterns*. Residual stresses are detected when non-axisymmetric speckle patterns occur ^[18]. Pre-tests are required before load changes to obtain baseline images for comparison with subsequent test results.

Ultrasonic Testing (UT)

UT is based on the propagation of bulk waves and their methods of intercepting discontinuities. The advantage of this technique is that it is the second-best ^[1] (after computed tomography) technique in terms of sensitivity to most of composite defects. But, unless the location of the defects is already known, UT is a time-consuming NDT technique. The other limitations of the technique are the use of coupling agents and the condition of the surface of inspection, which

is required to be as smooth as possible. UT can also be used to detect leaks which will cause refraction and reflection of ultrasonic waves. The ultrasound technique will be considered in more detail in this thesis.

1.3 Summary

Each of these NDT methods will not, on their own, detect all of the composite defects but, the combination of some of them, can help not only improve the sensitivity range but can also extend the validity of a technique from the manufacturing stage to throughout the service life of the component. Although they will not be suitable for all type of structure and defect types, most techniques mentioned in section 1.2 are more or only suitable to the manufacturing stage and for inspection purpose, than during in-service stage, especially for the structure requiring condition health monitoring. Computed tomography and ultrasonic testing would be the primary choice for inspection purposes, as they reportedly ^[1] detect most of the composite defects in comparison with the rest of the NDT methods. But it will be more convenient, practical and cheaper to use UT than CT: the main inconveniences in using UT are the surface condition and use of coupling agents where CT is branded time consuming, costly and dangerous due to the use of X-rays. CT applications are confined to laboratory environment where UT can be used both in laboratory and during site inspections. These two techniques are ideal for post manufacturing stage. Others can also be used soon after manufacture but they are far more limited than UT and CT:

- Radiography is recommended for void detection. Like CT, it is more for a laboratory application (post manufacture) than a site inspection
- Tap and mechanical impedance testing for delamination and disbonds in honeycomb structures but the former is only suitable for laminate thinner than 1 mm where the latter

is more appropriate to thicknesses greater than 10 mm. More suitable for laboratory environments.

- Electromagnetic methods for carbon fibre reinforced polymers only. Suitable both for laboratory and off-sites environments.
- Thermography for structure thicker than 8 mm but only ideal for inspections during service life of the component as the technique is not recommended for manufacturing defects (contamination, damaged filaments, inclusion, leaks, porosity, etc)
- Leak testing is more appropriate for post manufacturing stage but is only sensitive to leaks and voids.

Due to the types of defects they are sensitive to, some of the NDT methods for composites have an advantage over others, because they can be used both during and post manufacture. While the techniques mentioned above are for inspection purposes after manufacture, these methods can be used during the manufacturing process: the electrostatic, microwave and radio wave techniques.

From all the composites NDT methods discussed so far in this chapter, only shearography and acoustic emission will be appropriate and ideal for structural health monitoring. But AE is a more advantageous technique than shearography when it comes to SHM because, AE could easily and discreetly be used during the in-service life stage of a structure (outside a laboratory) while shearography would be limited to laboratory environment. And most importantly, AE detects more composite defects than shearography ^[1].

1.4 Industrial NDT approaches for composites

There are various NDT devices commercially available for the inspections of composite structures. These devices can reportedly detect composite defects such as delamination ^[19-23],

disbond ^[19-20, 22-29], porosity ^[19,22], impact damage ^[19-20, 22-23] and void ^[30]. Most of these NDT devices are based on ultrasonic testing ^[19, 24-26, 30-31] and also phased array ^[27,32], a special UT application. Like UT, the phased array technique is based on the propagation of bulk waves but the main difference between the two technique is in the probes: UT probes are made of a single crystal while in phased array ^[33], the probe contains many crystal elements which can operate simultaneously and independently of each other.

Few companies use NDT approaches such as mechanical impedance ^[28-29], shearography ^[20] and thermography ^[21-23]. All these devices are mainly designed for inspection purposes only (not structural health monitoring).

1.5 Thesis objectives

For decades, researchers studying the propagation of ultrasonic waves in materials, concentrated their attention on metals. Structures such as strips, plates, cylinders, rods and railway tracks were widely studied to understand the behaviour of ultrasonic waves, in media with and without boundaries and containing discontinuities. NDT techniques based on ultrasound propagation (UT, AE, Guided Wave Testing (GWT), etc...) were developed to provide industries (such as oil & gas, transport and aerospace) with reliable techniques for the inspection and SHM of commonly used metallic structures. For example, a few guided waves systems are commercially available for the inspection of pipelines from the oil and gas sector. These systems have been developed to inspect metallic pipelines over a relatively long distance and especially when access is limited; these systems are dedicated to the detection of features such as wall thickness loss due to internal or external corrosion. As the ultrasonic guided waves can travel long distances through the entire thickness of a material, the GWT method could be suitable for the inspection and health monitoring of large polymer matrix composite structures but, GWT is not an established method yet for the inspection of polymer matrix composites.

The overall aim of this thesis is to recommend new testing methods for the detection of delaminations during an inspection and the detection of growing defect (such as fibre/matrix cracks as well as delaminations) during SHM. This target will be met by achieving the following objectives:

- An assessment of the characteristics and performance of three transducers, specifically chosen because they are used in the Teletest Focus+ ^[34], the first commercially available guided wave system for pipeline inspection. Their performance will be compared and this work is reported in the chapter four of this thesis.
- An assessment of a guided wave testing technique for the inspection of composites, focussing on the detection of the delamination. Guided waves will be generated using one of the transducers studied in chapter four. The interaction of guided waves with the delamination will be studied with aim to identify advantages/disadvantages of guided wave testing compared with information related to the literature.
- An assessment a guided wave testing technique for the SHM of composites, during the three-point loading test of a glass fibre reinforced polymer (GFRP) material. The objective here is to establish a technique which enables guided wave monitoring to detect events occurring in laminates and to identify the precursors or warning to imminent failure. The results are discussed in chapter six

Chapter 2: BACKGROUND KNOWLEDGE ON POLYMER MATRIX COMPOSITES AND GUIDED WAVE TESTING

2.1 Background information on PMC

2.1.1 Introduction

A composite component is a result of the combination of several materials, carefully selected based on their mechanical properties, to create a high-performance structure designed for a specific application. Schwartz^[35] highlighted that any media can be called “composite”, when it is looked at an atomic, molecular (micro-composite) or structural (macro-composite) level. This thesis focuses on the LRUT of macro-composite materials used in the engineering sector. Composites are defined by three principal elements: the *matrix*, the *reinforcement* and the *interface* between the matrix and reinforcement. The matrix is the foundation of a composite component and can be made from metal, polymer or ceramic. The mechanical properties of the matrix are coupled with those of the “reinforcement”, through various manufacturing processes, and like the matrix, the reinforcement can be metallic, polymeric or ceramic and of various shapes^[35-36]: short/long fibres, particles, fillers, laminae and flakes. The quality of a bond between plies is a crucial detail as the bond allows the load transfer between the matrix and the reinforcement, providing a balance of stress distribution across the component under load. Most composites are anisotropic, meaning that their mechanical properties vary depending on the direction they are measured. The properties reportedly^[37] known to vary with fibre directionality are: the material’s electrical conductivity, moisture expansion, permeability, Poisson ratio, stiffness, strength, thermal conductivity and expansion. Not all mechanical properties depend on the fibre orientation; it was further reported^[37] that some factors remain unchanged throughout the entire material. Daniel^[37] reported that these factors are density, absorptivity and emittance.

2.1.2 Matrix and reinforcement

There are three main composite groups:

(a) The Metal Matrix Composites (MMC) for which the matrix ^[37] is made of metals such as aluminium, magnesium, titanium or copper. The reinforcement ^[37] used is typically boron, borsic, graphite, silicon carbide or alumina.

(b) The Ceramic Matrix Composites (CMC) are reportedly the preferred material when it comes to high temperature applications. Silicon carbide, alumina, glass-ceramic or silicon nitride are used to form the matrix ^[37] which can be reinforced ^[37] with whiskers of silicon carbide, alumina or silicon nitride.

(c) The Polymer Matrix Composites (PMC) for which the matrix is either thermosetting resins or thermoplastics, reinforced with either glass (mainly Electric E-glass type ^[36]) fibres of 10-20 μm ^[36-37] nominal diameter, carbon fibres (graphite) of 7-8 μm diameter ^[36] and finally boron or aramid (Kevlar) fibres of 12 μm diameter ^[36-37]. The thermoplastics commonly in use are the poly-propylene, Nylon 6.6 and poly-carbonate; and for thermosetting resins, the choice remains between epoxy and polyester. PMCs are the most commonly used composites in industry, more precisely the epoxy resins-type ^[37].

The main advantages of Fibre Reinforced Polymer (FRP) are their high strength-to-weight ratio and, their resistance to corrosion and fatigue damage. Although FRPs are heavily used in high profile sectors, they remain incompatible with high temperature applications and their ultimate failures are often unpredictable and thus can present a high safety risk.

An important parameter to take into consideration while studying composite behaviour is the fibre-to-resin ratio (or Fibre Volume Fraction – FVF). The higher the FVF, the stronger the material. The manufacturing process is a key factor to the performance of the final composite product and the FVF highly depends on it.

The stacking sequence is another key factor contributing to the performance and anisotropic nature of composites. It is described as the arrangement of plies within a material

and is always annotated as follows: $[A_x/B_y]_n$. A and B represent different angles of the plies while the subscripts x and y represent the number of layers orientated at these angles, respectively. The subscript “n” represents the number of times the sequence is repeated in the laminate. The subscript “n” can be accompanied with an “s” meaning the laminate is symmetric. The different sequences which can be found ^[37] in the literature are:

- Unidirectional laminate: All plies are orientated in one direction only. For a laminate containing 8 plies for example, the stacking sequence will be noted as $[0/0/0/0/0/0/0/0] = [0]_8$.
- Angle-ply laminate: When the fibres are orientated at any angle but 0° and 90° as follows. E.g. $[30/-30/-30/30] = [\pm 30]_s$ or $[45/-45/45/-45/45/-45/-45/45/-45/45/-45/45] = [\pm 45]_{3s}$.
- Cross-ply laminate: Plies only orientated at 0° and 90° : E.g. $[0/90/0/90] = [0/90]_2$.
- For multidirectional laminates, plies could be stacked in any directions. For example $[0/0/0/30/-30/0/0/0/0/0/0/0/-30/30/0/0/0] = [0_3/\pm 30/0_3]_s$.
- Quasi-isotropic: A composite tends to become less and less anisotropic when plies are stacked in the 0° , 45° and 90° angle orientation.

2.1.3 The interface

The interface is a very crucial parameter in composites and is controlled during manufacturing processes. It is the link between the reinforcement and the matrix, the element which hold all components altogether. The interface has an important mechanical effect ^[35,38] on the performance of composites: a weak interface decreases the material stiffness and strength but will improve its resistance to fracture; a strong bond will increase stiffness and strength but will make the material brittle. In the case of PMCs, the bond is usually achieved by using adhesives such epoxy resins or polyester. The interface or bond can be reinforced by adding coupling agents which create an additional constituent to the material, defined as the interphase.

2.1.4 Manufacturing processes

The manufacturing of fibre reinforced polymers is divided into two groups: the first group consists of open moulding techniques of which the most recognised is called the *hand lay-up* method. This method can be carried out wet or dry^[38]. The “wet” process consists of mixing the reinforcement and matrix in the open mould until the desired structural shape is achieved; the “dry” process consists in creating individual laminae or ply called *prepeg* (meaning pre-impregnated mainly with resin) which are in turn stacked together using either the *vacuum bag*, *pressure bag* or *autoclave* techniques. With the vacuum bag method, laminae (single ply) are assembled into a laminate by enveloping the prepeg in a vacuum bag which is exposed to atmospheric pressure. It was reported^[38] that the technique was limited to 1.5mm thick material and a pressure of 0.1MPa. For materials requiring a little bit more pressure, the pressure bag moulding technique is recommended. This technique is similar to the vacuum bag but compressed air is used instead of a vacuum, and the pressure bag is placed into a chamber instead of being exposed to atmospheric pressure. The autoclave method is used to fabricate the composite component intended for high performance applications^[38]. This technique consists of placing the prepeg in a vacuum bag which in turn is placed in a tank or a vessel filled with compressed gas.

Composite materials can also be fabricated by:

- Spraying short fibre and resin simultaneously into a mould by using specific equipment (the *spray-up method*);
- Twisting fibres (initially immersed in resin) into specific directions, using a mandrel (the *filament winding method*);
- Inserting fibres, in the resin matrix according to the orientation, which are controlled by a rotating mould (the *centrifugal casting method*).

The second group of manufacturing techniques is the closed mould processes. They consist of:

(a) The compression moulding technique, which consists of stacking prepegs using metallic moulds which can be cold or hot, hence the so-called methods *hot* and *cold* press moulding;

(b) The *Resin Transfer Moulding* (RTM) technique, reportedly ^[38] a cost-saving method, which consists of injecting resin in a closed mould already containing fibres (not prepeg) orientated according to structural design requirements;

(c) The pultrusion technique, which is a process that requires fibres to go through a bath of resin and a heated die (in that order) before the product is cut into its final shape. All these processes, designed to produce high performance components, have a common downside: they cannot guarantee the non-existence of manufacturing defects.

2.1.5 Elasticity principles

One of the main rules resulting from composite manufacturing process is the rule of mixture, also known as the Parallel (Voigt) model ^[37]:

$$\mathbf{C}_M = V_f \mathbf{C}_f + V_m \mathbf{C}_m$$

Equation 1: Rule of mixture ^[36-37]

With: $C_{M,f,m}$ – Longitudinal Modulus (Pa) of the composite, fibre and matrix respectively;

V_f - fibre volume fraction.

$V_m = 1 - V_f$, matrix volume fraction

The following equations (Equations 2-8) ^[37] illustrate the relationship between the stress and strain for composite materials, based on *Hooke's Law* and according to their level of anisotropy.

$$\boldsymbol{\sigma}_{ij} = \mathbf{C}_{ijkl} \boldsymbol{\varepsilon}_{kl} + \mathbf{C}_{ijkl} \alpha \Delta T \boldsymbol{\delta}_{ij}$$

$$\boldsymbol{\varepsilon}_{ij} = \mathbf{S}_{ijkl} \boldsymbol{\sigma}_{kl} + \alpha \Delta T \boldsymbol{\delta}_{ij}$$

$$\Delta T = T - T_0$$

Equation 2: Hooke's Law ^[37]

σ_{ij} – stress; ϵ_{ij} – strain; C_{ijkl} - Stiffness components; S_{ijkl} - Compliance components

α = Thermal expansion coefficient; $\Delta T = T - T_0$; δ_{ij} = Kronecker delta= 0 if $i \neq j$ or 1 if $i = j$

From this point onwards, α and ΔT are often considered negligible, because unless there is a severe change in the material's temperature, there is no need to include the thermal expansion and difference in temperature in the equations. Hooke's Law can further be developed based on the different levels of anisotropy of a material. For a general anisotropic material, Hooke's Law becomes:

$$\begin{bmatrix} \sigma_{11} \\ \sigma_{22} \\ \sigma_{33} \\ \sigma_{23} \\ \sigma_{31} \\ \sigma_{12} \\ \sigma_{32} \\ \sigma_{13} \\ \sigma_{21} \end{bmatrix} = \begin{bmatrix} C_{1111} & C_{1122} & C_{1133} & C_{1123} & C_{1131} & C_{1112} & C_{1132} & C_{1113} & C_{1121} \\ C_{2211} & C_{2222} & C_{2233} & C_{2223} & C_{2231} & C_{2212} & C_{2232} & C_{1113} & C_{1121} \\ C_{3311} & C_{3322} & C_{3333} & C_{3323} & C_{3331} & C_{3312} & C_{3332} & C_{3313} & C_{3321} \\ C_{2311} & C_{2322} & C_{2333} & C_{2323} & C_{2331} & C_{2312} & C_{2332} & C_{2313} & C_{2321} \\ C_{3111} & C_{3122} & C_{3133} & C_{3123} & C_{3131} & C_{3112} & C_{3132} & C_{3113} & C_{3121} \\ C_{1211} & C_{1222} & C_{1233} & C_{1223} & C_{1231} & C_{1212} & C_{1232} & C_{1213} & C_{1221} \\ C_{3211} & C_{3222} & C_{3233} & C_{3223} & C_{3231} & C_{3212} & C_{3232} & C_{3213} & C_{3221} \\ C_{1311} & C_{1322} & C_{1333} & C_{1323} & C_{1331} & C_{1312} & C_{1332} & C_{1313} & C_{1321} \\ C_{2111} & C_{2122} & C_{2133} & C_{2123} & C_{2131} & C_{2112} & C_{2132} & C_{2113} & C_{2121} \end{bmatrix} \begin{bmatrix} \epsilon_{11} \\ \epsilon_{22} \\ \epsilon_{33} \\ \epsilon_{23} \\ \epsilon_{31} \\ \epsilon_{12} \\ \epsilon_{32} \\ \epsilon_{13} \\ \epsilon_{21} \end{bmatrix}$$

Or

$$\begin{bmatrix} \epsilon_{11} \\ \epsilon_{22} \\ \epsilon_{33} \\ \epsilon_{23} \\ \epsilon_{31} \\ \epsilon_{12} \\ \epsilon_{32} \\ \epsilon_{13} \\ \epsilon_{21} \end{bmatrix} = \begin{bmatrix} S_{1111} & S_{1122} & S_{1133} & S_{1123} & S_{1131} & S_{1112} & S_{1132} & S_{1113} & S_{1121} \\ S_{2211} & S_{2222} & S_{2233} & S_{2223} & S_{2231} & S_{2212} & S_{2232} & S_{1113} & S_{1121} \\ S_{3311} & S_{3322} & S_{3333} & S_{3323} & S_{3331} & S_{3312} & S_{3332} & S_{3313} & S_{3321} \\ S_{2311} & S_{2322} & S_{2333} & S_{2323} & S_{2331} & S_{2312} & S_{2332} & S_{2313} & S_{2321} \\ S_{3111} & S_{3122} & S_{3133} & S_{3123} & S_{3131} & S_{3112} & C_{3132} & S_{3113} & S_{3121} \\ S_{1211} & S_{1222} & S_{1233} & S_{1223} & S_{1231} & S_{1212} & C_{1232} & S_{1213} & S_{1221} \\ S_{3211} & S_{3222} & S_{3233} & S_{3223} & S_{3231} & S_{3212} & C_{3232} & S_{3213} & S_{3221} \\ S_{1311} & S_{1322} & S_{1333} & S_{1323} & S_{1331} & S_{1312} & C_{1332} & S_{1313} & S_{1321} \\ S_{2111} & S_{2122} & S_{2133} & S_{2123} & S_{2131} & S_{2112} & C_{2132} & S_{2113} & S_{2121} \end{bmatrix} \begin{bmatrix} \sigma_{11} \\ \sigma_{22} \\ \sigma_{33} \\ \sigma_{23} \\ \sigma_{31} \\ \sigma_{12} \\ \sigma_{32} \\ \sigma_{13} \\ \sigma_{21} \end{bmatrix}$$

Equation 3: Hooke's Law for anisotropic material (81 independent stiffness or compliance constants)

For materials with 36 distinctive stiffness/compliance constants or with 21 distinctive constants (triclinic material) due to symmetry, Hooke's Law becomes:

$$\begin{bmatrix} \sigma_{11} \\ \sigma_{22} \\ \sigma_{33} \\ \sigma_{23} \\ \sigma_{31} \\ \sigma_{12} \end{bmatrix} = \begin{bmatrix} C_{1111} & C_{1122} & C_{1133} & C_{1123} & C_{1131} & C_{1112} \\ C_{2211} & C_{2222} & C_{2233} & C_{2223} & C_{2231} & C_{2212} \\ C_{3311} & C_{3322} & C_{3333} & C_{3323} & C_{3331} & C_{3312} \\ C_{2311} & C_{2322} & C_{2333} & C_{2323} & C_{2331} & C_{2312} \\ C_{3111} & C_{3122} & C_{3133} & C_{3123} & C_{3131} & C_{3112} \\ C_{1211} & C_{1222} & C_{1233} & C_{1223} & C_{1231} & C_{2112} \end{bmatrix} \begin{bmatrix} \epsilon_{11} \\ \epsilon_{22} \\ \epsilon_{33} \\ \epsilon_{23} \\ \epsilon_{31} \\ \epsilon_{12} \end{bmatrix}$$

Or

$$\begin{bmatrix} \epsilon_{11} \\ \epsilon_{22} \\ \epsilon_{33} \\ \epsilon_{23} \\ \epsilon_{31} \\ \epsilon_{12} \end{bmatrix} = \begin{bmatrix} S_{1111} & S_{1122} & S_{1133} & S_{1123} & S_{1131} & S_{1112} \\ S_{2211} & S_{2222} & S_{2233} & S_{2223} & S_{2231} & S_{2212} \\ S_{3311} & S_{3322} & S_{3333} & S_{3323} & S_{3331} & S_{3312} \\ S_{2311} & S_{2322} & S_{2333} & S_{2323} & S_{2331} & S_{2312} \\ S_{3111} & S_{3122} & S_{3133} & S_{3123} & S_{3131} & S_{3112} \\ S_{1211} & S_{1222} & S_{1233} & S_{1223} & S_{1231} & S_{1212} \end{bmatrix} \begin{bmatrix} \sigma_{11} \\ \sigma_{22} \\ \sigma_{33} \\ \sigma_{23} \\ \sigma_{31} \\ \sigma_{12} \end{bmatrix}$$

Equation 4: Hooke's Law for anisotropic/triclinic materials (36/21 independent constants)

The matrices can further be simplified by rearranging the numbers in subscript:

$$\begin{bmatrix} \sigma_1 \\ \sigma_2 \\ \sigma_3 \\ \tau_4 \\ \tau_5 \\ \tau_6 \end{bmatrix} = \begin{bmatrix} C_{11} & C_{12} & C_{13} & C_{14} & C_{15} & C_{16} \\ C_{21} & C_{22} & C_{23} & C_{24} & C_{25} & C_{26} \\ C_{31} & C_{32} & C_{33} & C_{34} & C_{35} & C_{36} \\ C_{41} & C_{42} & C_{43} & C_{44} & C_{45} & C_{46} \\ C_{51} & C_{52} & C_{53} & C_{54} & C_{55} & C_{56} \\ C_{61} & C_{62} & C_{63} & C_{64} & C_{65} & C_{66} \end{bmatrix} \begin{bmatrix} \epsilon_1 \\ \epsilon_2 \\ \epsilon_3 \\ \gamma_4 \\ \gamma_5 \\ \gamma_6 \end{bmatrix}$$

Or

$$\begin{bmatrix} \epsilon_1 \\ \epsilon_2 \\ \epsilon_3 \\ \gamma_4 \\ \gamma_5 \\ \gamma_6 \end{bmatrix} = \begin{bmatrix} S_{11} & S_{12} & S_{13} & S_{14} & S_{15} & S_{16} \\ S_{21} & S_{22} & S_{23} & S_{24} & S_{25} & S_{26} \\ S_{31} & S_{32} & S_{33} & S_{34} & S_{35} & S_{36} \\ S_{41} & S_{42} & S_{43} & S_{44} & S_{45} & S_{46} \\ S_{51} & S_{52} & S_{53} & S_{54} & S_{55} & S_{56} \\ S_{61} & S_{62} & S_{63} & S_{64} & S_{65} & S_{66} \end{bmatrix} \begin{bmatrix} \sigma_1 \\ \sigma_2 \\ \sigma_3 \\ \tau_4 \\ \tau_5 \\ \tau_6 \end{bmatrix}$$

The remaining equations represent Hooke's Law for materials with nine stiffness constants (orthotropic or orthorhombic material), five (transversely isotropic material or hexagonal), three (cubic material) and with two constants (isotropic material).

$$\begin{bmatrix} \sigma_1 \\ \sigma_2 \\ \sigma_3 \\ \tau_4 \\ \tau_5 \\ \tau_6 \end{bmatrix} = \begin{bmatrix} C_{11} & C_{12} & C_{13} & 0 & 0 & 0 \\ C_{21} & C_{22} & C_{23} & 0 & 0 & 0 \\ C_{31} & C_{32} & C_{33} & 0 & 0 & 0 \\ 0 & 0 & 0 & C_{44} & 0 & 0 \\ 0 & 0 & 0 & 0 & C_{55} & 0 \\ 0 & 0 & 0 & 0 & 0 & C_{66} \end{bmatrix} \begin{bmatrix} \epsilon_1 \\ \epsilon_2 \\ \epsilon_3 \\ \gamma_4 \\ \gamma_5 \\ \gamma_6 \end{bmatrix}$$

$$\begin{bmatrix} \varepsilon_1 \\ \varepsilon_2 \\ \varepsilon_3 \\ \gamma_4 \\ \gamma_5 \\ \gamma_6 \end{bmatrix} = \begin{bmatrix} S_{11} & S_{12} & S_{13} & 0 & 0 & 0 \\ S_{21} & S_{22} & S_{23} & 0 & 0 & 0 \\ S_{31} & S_{32} & S_{33} & 0 & 0 & 0 \\ 0 & 0 & 0 & S_{44} & 0 & 0 \\ 0 & 0 & 0 & 0 & S_{55} & 0 \\ 0 & 0 & 0 & 0 & 0 & S_{66} \end{bmatrix} \begin{bmatrix} \sigma_1 \\ \sigma_2 \\ \sigma_3 \\ \tau_4 \\ \tau_5 \\ \tau_6 \end{bmatrix}$$

Equation 5: Hooke's Law for orthotropic or orthorhombic material (9 constants)

$$\begin{bmatrix} \sigma_1 \\ \sigma_2 \\ \sigma_3 \\ \tau_4 \\ \tau_5 \\ \tau_6 \end{bmatrix} = \begin{bmatrix} C_{11} & C_{12} & C_{12} & 0 & 0 & 0 \\ C_{12} & C_{22} & C_{23} & 0 & 0 & 0 \\ C_{12} & C_{23} & C_{22} & \frac{C_{22} - C_{23}}{2} & 0 & 0 \\ 0 & 0 & 0 & 0 & C_{55} & 0 \\ 0 & 0 & 0 & 0 & 0 & C_{55} \\ 0 & 0 & 0 & 0 & 0 & 0 \end{bmatrix} \begin{bmatrix} \varepsilon_1 \\ \varepsilon_2 \\ \varepsilon_3 \\ \gamma_4 \\ \gamma_5 \\ \gamma_6 \end{bmatrix}$$

$$\begin{bmatrix} \varepsilon_1 \\ \varepsilon_2 \\ \varepsilon_3 \\ \gamma_4 \\ \gamma_5 \\ \gamma_6 \end{bmatrix} = \begin{bmatrix} S_{11} & S_{12} & S_{13} & 0 & 0 & 0 \\ S_{12} & S_{22} & S_{23} & 0 & 0 & 0 \\ S_{13} & S_{23} & S_{33} & 0 & 0 & 0 \\ 0 & 0 & 0 & 2(S_{22} - S_{23}) & 0 & 0 \\ 0 & 0 & 0 & 0 & S_{55} & 0 \\ 0 & 0 & 0 & 0 & 0 & S_{55} \end{bmatrix} \begin{bmatrix} \sigma_1 \\ \sigma_2 \\ \sigma_3 \\ \tau_4 \\ \tau_5 \\ \tau_6 \end{bmatrix}$$

Equation 6: Hooke's Law for transversely isotropic material or hexagonal material (5 constants)

$$\begin{bmatrix} \sigma_1 \\ \sigma_2 \\ \sigma_3 \\ \tau_4 \\ \tau_5 \\ \tau_6 \end{bmatrix} = \begin{bmatrix} C_{11} & C_{12} & C_{12} & 0 & 0 & 0 \\ C_{12} & C_{11} & C_{12} & 0 & 0 & 0 \\ C_{12} & C_{12} & C_{11} & 0 & 0 & 0 \\ 0 & 0 & 0 & C_{44} & 0 & 0 \\ 0 & 0 & 0 & 0 & C_{44} & 0 \\ 0 & 0 & 0 & 0 & 0 & C_{44} \end{bmatrix} \begin{bmatrix} \varepsilon_1 \\ \varepsilon_2 \\ \varepsilon_3 \\ \gamma_4 \\ \gamma_5 \\ \gamma_6 \end{bmatrix}$$

Equation 7: Hooke's Law for cubic material (3 constants)

$$\begin{bmatrix} \sigma_1 \\ \sigma_2 \\ \sigma_3 \\ \tau_4 \\ \tau_5 \\ \tau_6 \end{bmatrix} = \begin{bmatrix} C_{11} & C_{12} & C_{12} & 0 & 0 & 0 \\ C_{12} & C_{11} & C_{12} & 0 & 0 & 0 \\ C_{12} & C_{12} & C_{11} & 0 & 0 & 0 \\ 0 & 0 & 0 & \frac{C_{11} - C_{12}}{2} & 0 & 0 \\ 0 & 0 & 0 & 0 & \frac{C_{11} - C_{12}}{2} & 0 \\ 0 & 0 & 0 & 0 & 0 & \frac{C_{11} - C_{12}}{2} \end{bmatrix} \begin{bmatrix} \varepsilon_1 \\ \varepsilon_2 \\ \varepsilon_3 \\ \gamma_4 \\ \gamma_5 \\ \gamma_6 \end{bmatrix}$$

Equation 8: Hooke's Law for isotropic material (2 constants)

These equations are the foundations of the study and modelling of displacement of ultrasonic waves in materials.

2.1.6 Polymer Matrix Composites defects and failure modes

A non-exhaustive list^[1,39] of defects caused by (a) manufacturing processes, (b) recurrent load variation during service life and (c) exposure to environment, is given below (by alphabetic order):

- **Buckling** is the physical deformation of a component due to constant subjection to load or thermal variation. Buckling affects both the health condition of the reinforcement and matrix.
- **Contamination** is caused by the presence of unwanted fluids such as oil or water. This will occur during fabrication when the material is vulnerably exposed to the environment.
- **Filament damage (fibre breakage)** can be caused by impact and tensile loading. As the filament is a strand of the reinforcement, this defect will be very small in comparison to the overall size of the structure.
- **Delamination** is the physical detachment of prepegs due to poor curing process, impact or fatigue of the component. As previously mentioned, this is the most common defect.
- **Disbond or debonding** is like delamination but is more relevant to the separation of large components from within the same structure. For example, the detachment of the spar box or cap from the shell of a wind turbine blade is due to debonding.
- **Fatigue damage** occurs during tension-tension, tension-compression or compression-compression loading. It results in the combination of several defects (matrix cracks, fibre breaks, delamination, etc.) occurring simultaneously or successively and over a long period of time.

- **Fibre wrinkling** is a surface defect reportedly ^[39] caused by the vacuum bag manufacturing method.
- **Fibre misalignment** occurs when the fibres are not orientated in directions specified by structural designs. The manufacturing defect is a precursor to fibre breakage.
- **Inclusion** describes the presence of an unwanted bodily solid and occurs by poorly controlled manufacturing process.
- **Matrix cracking** is caused by repeat loading, buckling or impact damage. This defect is a precursor to leaks.
- **Resin poor/fibre rich area** (also described as thickness variation) is the portion of the component which differs from the fibre volume fraction recommended by structural design.
- **Residual stress** is another manufacturing defect occurring when the temperature within the material suddenly drops (for example from curing to atmospheric temperature).
- **Voids** are defined by empty space between laminates. It was explained ^[39] that an increase in density of voids will create porosity (another type of polymer defect).

2.1.7 Key industry sectors for Polymer Matrix Composites

PMC are used in many high-profile sectors. It was reported that 40% of aircraft and aerospace structures are made of polymer matrix composites ^[40]. They are used in wings, fuselage, landing gears, radome, tail and stabilisers. They are also used for the manufacture of helicopter blades. In the marine sector, boat hulls, decks and masts are made of composite materials. The transport sector also found PMCs of a great use and importance. They make most of the body parts and the interior of vehicles. The chemical sector uses pipes, tanks and pressure vessels made of PMCs. One of the latest, but not least, sectors to benefit from using PMCs is the renewable energy sector, where panels of turbine blades are made of GFRPs.

2.2 Background information on Guided Wave Testing

2.2.1 Ultrasonic Testing

The sound spectrum is divided into three regions: the infrasonic range (< 20Hz), the audible range (20Hz–20kHz) and the ultrasonic range (>20kHz). Ultrasonic testing generally operates in the 0.5-20MHz^[41] frequency range. When the ultrasonic wavelengths are much smaller than the material thickness they are travelling in, they are called *bulk waves*. In this scenario the material can be considered as an infinite media for the purpose of studying the wave behaviour. Bulk waves consist of two types: (i) compression waves, where the material displacement due to vibration is parallel to the direction of wave propagation and (ii) shear waves where the displacement is perpendicular to the direction of propagation. The mode shapes of their displacement can be numerically modelled by solving two main equations: The Navier-Stokes and Christoffel equations for isotropic and anisotropic materials respectively. Solving the Navier-Stokes equation allows the determination of the (compression or shear) wave characteristics by calculating their velocity:

$$(\lambda + \mu)u_{j,ij} + \mu u_{i,jj} + \rho f_i = \rho \ddot{u}_i \quad (i,j = 1,2,3);$$

Equation 9: Navier-Stokes equation^[42]

For $i = 1$, the Navier equation gives:

$$(\lambda + \mu) \left(\frac{\partial u_1}{\partial x_1} \frac{\partial}{\partial x_1} + \frac{\partial u_2}{\partial x_1} \frac{\partial}{\partial x_2} + \frac{\partial u_3}{\partial x_1} \frac{\partial}{\partial x_3} \right) + \mu \left(\frac{\partial u_1}{\partial x_1} \frac{\partial}{\partial x_1} + \frac{\partial u_1}{\partial x_2} \frac{\partial}{\partial x_2} + \frac{\partial u_1}{\partial x_3} \frac{\partial}{\partial x_3} \right) + \rho f_1 = \rho \frac{\partial^2 u_1}{\partial t^2}$$

For $i = 2$;

$$(\lambda + \mu) \left(\frac{\partial u_1}{\partial x_2} \frac{\partial}{\partial x_1} + \frac{\partial u_2}{\partial x_2} \frac{\partial}{\partial x_2} + \frac{\partial u_3}{\partial x_2} \frac{\partial}{\partial x_3} \right) + \mu \left(\frac{\partial u_2}{\partial x_1} \frac{\partial}{\partial x_1} + \frac{\partial u_2}{\partial x_2} \frac{\partial}{\partial x_2} + \frac{\partial u_2}{\partial x_3} \frac{\partial}{\partial x_3} \right) + \rho f_2 = \rho \frac{\partial^2 u_2}{\partial t^2}$$

For $i = 3$;

$$(\lambda + \mu) \left(\frac{\partial u_1}{\partial x_3} \frac{\partial}{\partial x_1} + \frac{\partial u_2}{\partial x_3} \frac{\partial}{\partial x_2} + \frac{\partial u_3}{\partial x_3} \frac{\partial}{\partial x_3} \right) + \mu \left(\frac{\partial u_3}{\partial x_1} \frac{\partial}{\partial x_1} + \frac{\partial u_3}{\partial x_2} \frac{\partial}{\partial x_2} + \frac{\partial u_3}{\partial x_3} \frac{\partial}{\partial x_3} \right) + \rho f_3 = \rho \frac{\partial^2 u_3}{\partial t^2}$$

By neglecting the forces^[42], the equation becomes:

$$(\lambda + \mu) \nabla * \nabla * \vec{u} + \mu \nabla^2 \vec{u} = \rho \frac{\partial^2 \vec{u}}{\partial t^2}$$

Equation 10: Navier-Stokes equation in scalar Cartesian^[42]

$$\text{With } \nabla = \vec{J}_1 \frac{\partial}{\partial x_1} + \vec{J}_2 \frac{\partial}{\partial x_2} + \vec{J}_3 \frac{\partial}{\partial x_3}; \nabla^2 = \frac{\partial^2}{\partial x_1^2} + \frac{\partial^2}{\partial x_2^2} + \frac{\partial^2}{\partial x_3^2}; \vec{u} = (u_1, u_2, u_3)$$

Rose demonstrated^[42] that the Navier-Stokes equation can be solved by using the vector identity and the Helmholtz decomposition:

$$\nabla^2 \vec{u} = \nabla * \nabla * \vec{u} - \nabla \times \nabla \times \vec{u}$$

Equation 11: The Vector identity^[42]

$$\vec{u} = \nabla * \phi + \nabla \times \psi, \quad \nabla * \psi = 0$$

Equation 12: The Helmholtz decomposition^[42]

with $\vec{u} = \text{the vector displacement}$;

$$\nabla * \phi = \left(\vec{i}_1 \frac{\partial}{\partial x_1} + \vec{i}_2 \frac{\partial}{\partial x_2} + \vec{i}_3 \frac{\partial}{\partial x_3} \right) * \phi$$

$$\nabla \times \psi = \begin{vmatrix} \vec{i}_1 & \vec{i}_2 & \vec{i}_3 \\ \frac{\partial}{\partial x_1} & \frac{\partial}{\partial x_2} & \frac{\partial}{\partial x_3} \\ \psi & \psi & \psi \end{vmatrix}$$

By inserting the vector identity and the Helmholtz decomposition in Equation 9, the equations of motion for the compression and shear waves can be determined:

$$(\lambda + \mu) \nabla * \nabla * \vec{u} + \mu (\nabla * \nabla * \vec{u} - \nabla \times \nabla \times \vec{u}) = \rho \frac{\partial^2 \vec{u}}{\partial t^2}$$

$$\xrightarrow{\text{yields}} (\lambda + 2\mu) \nabla * \nabla * \vec{u} - \mu \nabla \times \nabla \times \vec{u} = \rho \frac{\partial^2 \vec{u}}{\partial t^2}$$

$$\xrightarrow{\text{yields}} [(\lambda + 2\mu) \nabla * \nabla * (\nabla \phi + \nabla \times \psi)] - \mu \nabla \times \nabla \times [\nabla * \phi + \nabla \times \psi] = \rho \frac{\partial^2 (\nabla * \phi + \nabla \times \psi)}{\partial t^2}$$

$$\xrightarrow{\text{yields}} (\lambda + 2\mu) \nabla * \nabla^2 \phi + (\lambda + 2\mu) \nabla \nabla * \nabla \times \psi - \mu \nabla \times \nabla \times \nabla * \phi - \mu \nabla \times \nabla \times \nabla \times \psi -$$

$$\rho \nabla \frac{\partial^2 \phi}{\partial t^2} - \rho \nabla \times \frac{\partial^2 \psi}{\partial t^2} = 0$$

The equation above can be simplified by applying the identities ^[42] below:

$$\nabla \times \nabla \times \nabla * \phi = \mathbf{0}; \quad \nabla * \nabla \times \psi = \mathbf{0}.$$

$$\left[(\lambda + 2\mu) \nabla * \nabla^2 \phi - \rho \nabla * \frac{\partial^2 \phi}{\partial t^2} \right] + \left[\mu \nabla \times \nabla^2 \psi - \rho \nabla \times \frac{\partial^2 \psi}{\partial t^2} \right] = \mathbf{0}$$

$$\xrightarrow{\text{yields}} \nabla * \left[(\lambda + 2\mu) \nabla^2 \phi - \rho \frac{\partial^2 \phi}{\partial t^2} \right] + \nabla \times \left[\mu \nabla^2 \psi - \rho \frac{\partial^2 \psi}{\partial t^2} \right] = \mathbf{0}$$

The equation above is null if both terms in the equation are also null:

$$\text{For } (\lambda + 2\mu) \nabla^2 \phi - \rho \frac{\partial^2 \phi}{\partial t^2} = \mathbf{0} \rightarrow (\lambda + 2\mu) \nabla^2 \phi = \rho \frac{\partial^2 \phi}{\partial t^2} \rightarrow \nabla^2 \phi = \frac{\rho}{(\lambda + 2\mu)} \frac{\partial^2 \phi}{\partial t^2}$$

$$\rightarrow \nabla^2 \phi = \frac{1}{\frac{(\lambda + 2\mu)}{\rho}} \frac{\partial^2 \phi}{\partial t^2} \xrightarrow{\text{yields}}$$

$$\nabla^2 \phi = \frac{1}{C_L^2} \frac{\partial^2 \phi}{\partial t^2}$$

Equation 13: Equation of motion for compressional waves in isotropic materials ^[42]

$$\text{For } \mu \nabla^2 \psi - \rho \frac{\partial^2 \psi}{\partial t^2} = \mathbf{0} \rightarrow \nabla^2 \psi = \frac{\rho}{\mu} \frac{\partial^2 \psi}{\partial t^2}$$

$$\xrightarrow{\text{yields}} \nabla^2 \psi = \frac{1}{\frac{\mu}{\rho}} \frac{\partial^2 \psi}{\partial t^2}$$

Equation 14: Equation of motion for shear waves in isotropic materials ^[42]

C_L and C_T represent the velocities of the compression wave and the shear wave respectively.

$$C_L^2 = \frac{\lambda + 2\mu}{\rho}$$

Equation 15: Velocity for the Compression wave in isotropic materials ^[42]

$$C_T^2 = \frac{\mu}{\rho}$$

Equation 16: Velocity for the Shear wave in isotropic materials ^[42]

In Engineering, ultrasonic testing is widely used for the inspection of welds in plates and pipes.

The inspection is conducted by transmitting mechanical vibrations to a component by using

transducers requiring coupling agents (mostly gel but water and air are also used) to optimise the energy transmission.

2.2.2 Guided Wave Testing

When the ultrasonic wavelength is greater than the component thickness, the energy becomes constrained within the boundaries of the material, causing ultrasonic waves to propagate in specific patterns. The component is then called a waveguide, hence the denomination *guided wave*. GWT is also known as Long Range Ultrasonic Testing (LRUT), as sound waves can travel many metres in elongated objects, through their entire thickness. The testing frequency is between 20kHz and 500kHz. They propagate in (i) longitudinal, torsional or flexural patterns in pipes ^[43-45], wires ^[46-47] and railway tracks ^[48-49]. They are called Rayleigh waves when travelling on the surface and Stonely waves when propagation occurs at an interface between two surfaces. Guided waves in plates can either take the form of longitudinal waves (also known as Lamb waves) or shear horizontal waves.

Lamb waves are divided into two categories: the symmetric (S) and asymmetric (A) wave modes according to the displacement pattern of the mid plane of the plate. In the ultrasonic frequency range, many modes exist and are distinguished from one another with different numbers. Shear horizontal modes can also take the form of being either symmetric (SH) or asymmetric (AH). The fundamental Lamb waves are called the symmetric and asymmetric zero-order modes, S_0 and A_0 respectively, which coexist along with another fundamental mode, the shear-horizontal, SH_0 . As the frequency-thickness product increases, other modes (such as S_1 , S_2 , A_1 , A_2 and so on) are possible. These different modes of vibration are shown in Figure 1.

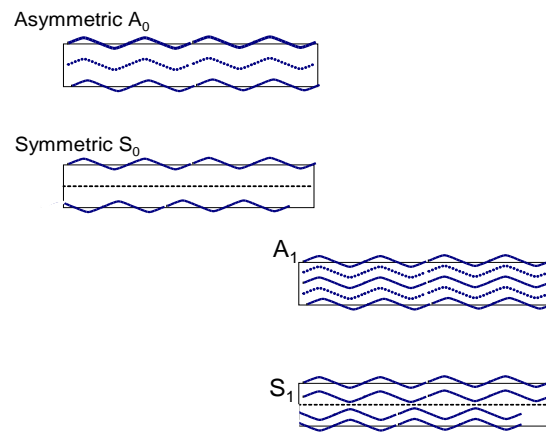


Figure 1: Plate waves ^[50]

The energy distribution throughout the thickness of a material can be determined by studying wave displacement. Because of dispersion, the shape of the ultrasonic wave will vary with the frequency-thickness product ($f*t$). Rose explained ^[42] that a varying $f*t$ will affect the proportion between in-plane and out-of-plane displacements of each symmetric and asymmetric modes. Lamb waves can detect defects such as corrosion, cracks and notches in metallic plates and their sensitivity to defects is increased if they intersect with a defect whose size is at least larger than one wavelength ^[51-52].

$$\lambda = \frac{\text{Wave Velocity}}{\text{frequency}} = \frac{C_w}{f}$$

Equation 17: Wavelength

The main and crucial advantage of GWT over ultrasonic testing is the large area coverage. In UT, only the volume directly under or in the vicinity of the probe is inspected, which leads to the requirement that the structure is manually swept with the probe for large area inspection. This is often impractical for the whole structure and so there is a need to apply UT selectively. GWT on the other hand can screen large volumes of a structure (often up to many tens of meters from the probe) without the need for the probe being swept.

GWT also allow inspection of areas with difficult access. Guided wave systems are also available as permanently installed tools for the continuous health monitoring of structures during their service life.

2.2.3 Dispersion curves

An ultrasonic signal is made up of a band of frequencies. It is common to transmit only a short pulse. Each frequency in the bandwidth propagates with its own speed, known as the phase velocity. The net effect of each frequency in the bandwidth propagating is that the envelope of the pulse is propagated. Since equipment tends to transmit and record signals in the time domain, it is the propagation of the pulse that is usually observed. The velocity of propagation of the pulse is known as the *Group Velocity*. When the phase velocity is the same for all frequencies in the bandwidth, the phase velocity will equal the group velocity. However, if the phase velocity varies over the bandwidth, the envelope of the pulse will change shape over time. This phenomenon is called *Dispersion*, and is a very significant aspect of GWT. The propagation characteristic of all-orders of guided waves in plates are obtained by plotting velocities against the frequency-thickness product $f*t$. These plots are called *dispersion curves* and are derived:

- (i) analytically by methods of continuum mechanics (such as by using the commercially available software Disperse^[53])
- (ii) experimentally by being directly measured from a wave propagating in a real specimen or,
- (iii) numerically using Finite Element methods. All but one of the possible guided waves in plates are known to be dispersive.

Examples of dispersion curves for 2 mm-thick laminate are shown in Figure 2.

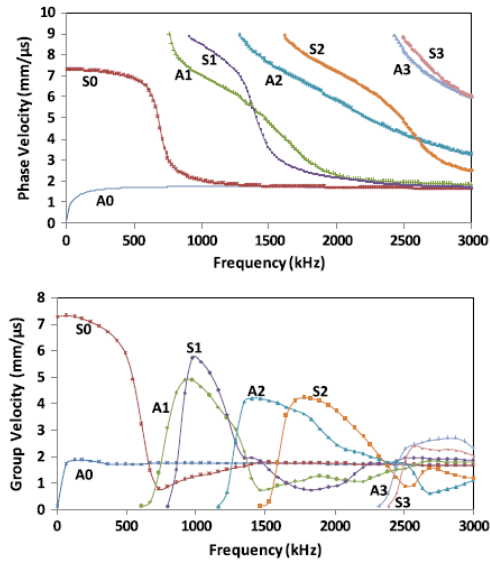


Figure 2: Dispersion curves of a $[0/90]_{2s}$ laminate ^[54]

Most guided wave techniques are carried out with the aim to minimise dispersion since distortion to the pulse shape during propagation hinders the interpretation of results ^[55].

An analytical method for obtaining dispersion curves can also be found in Rose's book ^[42]. He explained how to get the *dispersion relations* equations also known as the *Rayleigh-Lamb frequency relations* equations. Rose ^[42] considered one of the simplest case scenarios, which is an isotropic plate in a two-dimensional (x_1, x_3) plane. The dispersions relations were obtained by starting looking at the strain-stress relationship for isotropic material and the Helmholtz decomposition mentioned earlier (Equation 12):

$$\sigma_{ij} = \lambda \varepsilon_{kk} \delta_{ij} + 2\mu \varepsilon_{ij}$$

Equation 18: Strain-stress relationship for isotropic material under uniaxial load ^[37]

$$\text{With } \varepsilon_{ij} = \frac{1}{2} (u_{i,j} + u_{j,i}) = \frac{1}{2} \left(\frac{\partial u_i}{\partial x_j} + \frac{\partial u_j}{\partial x_i} \right);$$

$$\varepsilon_{kk} = (u_{i,i} + u_{j,j}) = \left(\frac{\partial u_i}{\partial x_i} + \frac{\partial u_j}{\partial x_j} \right);$$

In the two-dimensional (x_1, x_3) plane, the coordinates of the vector displacement $\vec{u} = (u_1, 0, u_3)$ can be expressed as follows through the Helmholtz decomposition (Equation 12):

$$u_1 = \frac{\partial \phi}{\partial x_1} + \frac{\partial \psi}{\partial x_3}$$

$$u_3 = \frac{\partial \phi}{\partial x_3} - \frac{\partial \psi}{\partial x_1}$$

Equation 19: Coordinates of \vec{u}

By inserting the coordinates above in Equation 18, the stress-strain relationship becomes:

$$\sigma_{31} = 2\mu\varepsilon_{31} = \mu \left(\frac{\partial u_3}{\partial x_1} + \frac{\partial u_1}{\partial x_3} \right) = \mu \left(\frac{\partial^2 \phi}{\partial x_1 \partial x_3} - \frac{\partial^2 \psi}{\partial^2 x_1} + \frac{\partial^2 \psi}{\partial x_3^2} \right);$$

$$\sigma_{33} = \lambda(u_{1,1} + u_{3,3}) + 2\mu\varepsilon_{33} = \lambda \left(\frac{\partial u_1}{\partial x_1} + \frac{\partial u_3}{\partial x_3} \right) + 2\mu \left[\frac{1}{2} \left(\frac{\partial u_3}{\partial x_3} + \frac{\partial u_3}{\partial x_3} \right) \right] = \lambda \left(\frac{\partial u_1}{\partial x_1} + \frac{\partial u_3}{\partial x_3} \right) +$$

$$2\mu \frac{\partial u_3}{\partial x_3} = \lambda \left(\frac{\partial^2 \phi}{\partial^2 x_1} + \frac{\partial^2 \phi}{\partial^2 x_3} \right) + 2\mu \left(\frac{\partial^2 \phi}{\partial^2 x_3} - \frac{\partial^2 \psi}{\partial x_1 \partial x_3} \right)$$

Equation 20: Strain-stress relationship after manipulation ^[42]

In order to solve a system of differential equations, it is very practical to first consider the solution to be in a complex form ^[42]. Rose ^[42] assumed the following forms:

$$\phi = \phi(x_3)e^{i(kx_1 - wt)} \text{ and } \psi = \psi(x_3)e^{i(kx_1 - wt)}$$

Where $\phi(x_3)$ and $\psi(x_3)$ are the unknown parameters. Their explicit forms can be obtained through the ‘‘method of potential’’ ^[42]. This method consists in substituting ϕ and ψ in Equation 13 and Equation 14, which represent respectively the motion for compression and shear waves in isotropic materials. After the substitution and numerous manipulations, a system of linear differential equations of the second order will be obtained. As ϕ and ψ are of a complex form, the general solutions for $\phi(x_3)$ and $\psi(x_3)$ are:

$$\phi(x_3) = A_1 \sin(px_3) + A_2 \cos(px_3)$$

$$\psi(x_3) = B_1 \sin(qx_3) + B_2 \cos(qx_3)$$

Equation 21: Explicit forms for $\phi(x_3)$ and $\psi(x_3)$ ^[56]

With A_1, A_2, B_1 and B_2 constants, $p^2 = \frac{w^2}{c_L^2} - k^2$ and $q^2 = \frac{w^2}{c_T^2} - k^2$

It was reported^[42,57] that **Equation 21** can be split into two equation systems, one representing the symmetric mode and the other, the antisymmetric mode. Rose^[42] further added that the split of equations can only occur if the ultrasonic waves are propagating in a structure containing an axis of symmetry:

$$\phi(x_3) = A_2 \cos(px_3)$$

$$\psi(x_3) = B_1 \sin(qx_3)$$

Equation 22: Explicit forms for $\phi(x_3)$ and $\psi(x_3)$ for symmetric modes^[42,57]

$$\phi(x_3) = A_1 \sin(px_3)$$

$$\psi(x_3) = B_2 \cos(qx_3)$$

Equation 23: Explicit forms for $\phi(x_3)$ and $\psi(x_3)$ for antisymmetric modes^[42,57]

By substituting the explicit forms of ϕ and ψ in Equation 20, the strain-stress relationships for the symmetric and antisymmetric modes are obtained:

$$\sigma_{31} = \mu [-2ikpA_2 \sin(px_3) + (k^2 - q^2)B_1 \sin(qx_3)]$$

$$\sigma_{33} = -\lambda(k^2 + p^2)A_2 \cos(px_3) - 2\mu[p^2A_2 \cos(px_3) + ikqB_1 \cos(qx_3)]$$

Equation 24: Strain-stress relationship – symmetric modes^[42]

$$\sigma_{31} = \mu [2ikpA_1 \cos(px_3) + (k^2 - q^2)B_2 \cos(qx_3)]$$

$$\sigma_{33} = -\lambda(k^2 + p^2)A_1 \sin(px_3) - 2\mu[p^2A_1 \sin(px_3) - ikqB_2 \sin(qx_3)]$$

Equation 25: Strain-stress relationship – antisymmetric modes^[42]

Rose^[42] considered that $\sigma_{31} = \sigma_{33} = 0$ and $x_3 = \pm h$ (traction-free boundary condition). From this assumption and after numerous equation manipulations and substitutions, the dispersion relation equations are obtained:

$$\frac{\tan qh}{\tan ph} = - \frac{4k^2pq}{(q^2 - p^2)^2}$$

Equation 26: Dispersion relation for symmetric modes^[42]

$$\frac{\tan qh}{\tan ph} = - \frac{(q^2 - p^2)^2}{4k^2pq}$$

Equation 27: Dispersion relation for antisymmetric modes ^[42]

The term “k” is called the wavenumber. It is defined as the number of waves i.e., the number of wavelengths per meter or per second. The term k is expressed as:

$$k = \frac{\omega}{c_p} = \frac{2\pi f}{c_p}$$

Equation 28: Wavenumber formula

By substituting k in Equation 26 and Equation 27 and for set angular frequencies, the variation of phase/group velocities against frequency can be plotted, i.e. the dispersion curves can be generated.

Equation 26 and Equation 27 are reported ^[42] to be specific to isotropic materials. For other types of materials, different assumptions would be made to generate dispersion relations. This process is extremely complicated and would be even more for anisotropic materials. Therefore, researchers would use software packages such as Disperse to generate disperse curves, or they will use experimental methods. Because the specimens investigated in this thesis are composite materials, the experimental method were used in order to obtain the disperse curves. The method is further explained in Chapter 4.

2.2.4 Testing method

The main measurement methods for GWT are the Pulse-Echo, Pitch-Catch, and Through Transmission methods. Each of these are explained below.

Pulse-Echo

The Pulse-Echo technique consists of using the same probe for transmitting and receiving ultrasonic waves.

Pitch-Catch

The Pitch-catch method uses separate probes for transmitting and receiving signals. Flaws will disrupt the transmitted signal, and this disruption can be materialised by attenuation and scattering. Separate probes solely acting as receivers will allow recording of these changes in the transmitted pulse.

Through-Transmission

The Through-Transmission method is a specific kind of pitch-catch. It requires probes to be mounted on opposite side of the test component (one transmits and the other receives). Defects will be intercepted when transmitted energy levels are reduced or arrival times are changed.

2.2.5 GWT applications

For many years, GWT has been mainly focussing on the inspection of pipelines from the oil and gas industry. For more than a decade, only three guided wave systems were made commercially available for the detection of cracks, erosion, pitting and (internal and external) corrosion. These systems are:

- **Teletest Focus+** ^[34], the first commercially available guided wave system for pipeline inspection; it was developed by The Welding Institute (TWI) and now supplied by Eddyfi;
- **Wavemaker** ^[58], developed by Imperial College London and supplied by Guided Ultrasonics Limited (GUL);
- And the **MsS** system ^[59]. The technology was developed by Southwest Research Institute[®] (SwRI[®]) and the system supplied by Guided Wave Analysis LLC.

More recently, other companies have produced guided wave systems, such as Olympus which has released the UltraWave LRT ^[60].

The experimental work presented in this thesis has been supported with the use of the Teletest Focus + hardware and software.

Chapter 3: LITERATURE REVIEW

3.1 The propagation of ultrasonic waves in non-defective composites

The research work on the capabilities of guided waves to detect defects in composites started with studying and understanding their propagation in this type of material. As previously mentioned, GWT is not a standard NDT technique for PMC laminates, therefore, extensive research work is continually being carried out in this field. The calculation of wave velocities in isotropic structures can be complex and it is even more complicated in anisotropic materials. Most of the research work from the literature has been focussed on the lowest frequency range that could be feasibly used for inspection in order to limit the number of wave modes existing in the material. There was particular interest in the propagation of the fundamental Lamb waves (S_0 and A_0). The velocity of some wave modes is not only dependent on the frequency-thickness product (like in isotropic materials), but is also dependent on the direction of propagation as mechanical properties vary with fibre orientations. This was demonstrated ^[61-62] numerically and experimentally for the S_0 mode, which reportedly travels faster in directions parallel to the main reinforcement (direction in which a composite is cut) than in directions across the main reinforcement. On the other hand, the velocity of the A_0 mode is independent of fibre orientation ^[51,63] but significantly affected by the volume ^[64] of fibres (i.e. fibre volume fraction) within fibre-reinforced composites.

Before highlighting the different guided wave inspection techniques (numerical and experimental) based on the excitation of the fundamental Lamb waves for the detection of composite defects, further background information is given on details which will be mentioned in the technical chapters of this thesis. These details are the sensors and baseline subtraction methods.

3.2 Sensors, actuators and transducers

3.2.1 Piezoelectricity

Piezoelectric transducers are widely used with ultrasonic inspection systems. The lead-zirconate-titanate (PZT) transducers is the most commonly used for ultrasonic testing techniques because they have a good sensitivity and high operating temperatures in comparison with other transducers types ^[65]. This thesis focusses on this type of transducers. Therefore, before defining sensors and their poling characteristics, it is necessary to understand the piezoelectricity phenomenon and its reverse effect. Piezoelectricity ^[65-67] occurs when an electric field results from a crystal element subjected to a mechanical strain or stress. Inverse piezoelectricity occurs when the crystal element exhibits mechanical strain or stress in a presence of an electrical field. Piezoelectricity was discovered in 1880 by Jacques and Pierre Curie ^[65-67].

3.2.2 Polarisation

The polar domains in a crystal are aligned in random directions when a crystal element is in its natural state. To make this crystal suitable to a specific need, its polarisation will be required. A crystal becomes polarised ^[65-67] (or poled) when it is subjected to an electrical field causing the re-alignment of its polar domains in the same direction of the electrical field. This phenomenon can also cause the crystal to lengthen or shorten to directions either parallel or perpendicular to the axis of polarisation. The polarisation of a crystal can be categorised by a parameter called the piezoelectric constant charge ^[65] ‘ d ’. This parameter gives details on the axis of both mechanical strain and electric field. For example, “ d_{xy} ” is the constant for a deformation occurring in direction y and caused by electric field applied in direction x.

The polarisation process can be further explained through its hysteresis loop ^[65, 67-68]. The loop illustrates the effect of the electric field on the crystal polarisation:

When a crystal is polarised for the first time, the process will follow the red line ^[68]. As the electric field E increases, the number of aligned polar domains increases until polarisation reaches a point of saturation P_s , i.e., all polar domains in the crystal are aligned with E .

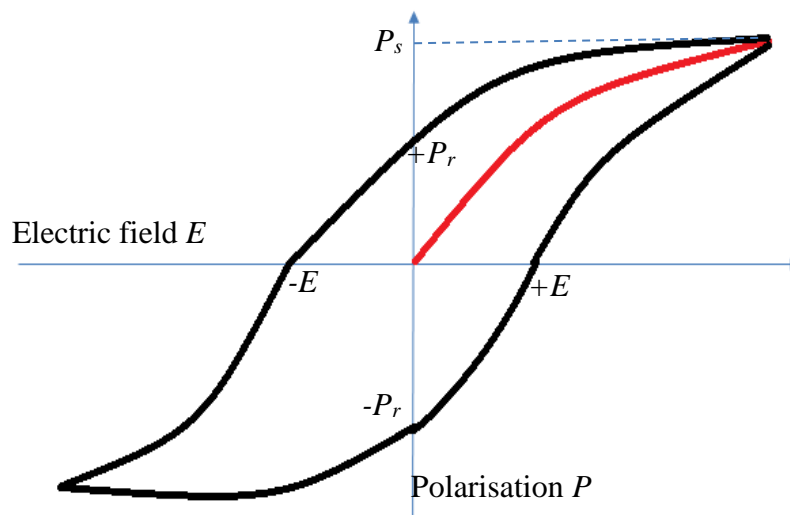


Figure 3: An example of hysteresis loop for polarisation of a crystal

- When the crystal is removed from the electrical field, i.e. E equals zero, the polarisation saturation will drop to a point called remanent polarisation P_r ^[65]. This demonstrates that the crystal will not entirely go back to its natural state when outside the electric field but it will retain most of its polarisation characteristics.
- If the electrical field is reversed, it can cause the crystal material to return to its initial states, i.e. it becomes completely depolarised. In this case, E reaches a negative value while P equals zero.
- A crystal can be also be polarised in an opposite direction, with P reaching values such as ' $-P_s$ ' or ' $-P_r$ '.

- A positive electric field can be re-applied to depolarise the crystal and then further increased until P reaches $+P_s$ again i.e. the hysteresis loop will be closed.

3.2.3 Sensors

A sensor is a product which functionality is solely based on piezoelectricity: Its role is to detect a mechanical strain or stress and to convert it into an electrical signal. There are two types of sensors [65]:

- The axial type is the one sensitive to mechanical strain parallel to a polarisation resulting from a parallel electrical field. When the strain and electrical field are generated in the same direction 'x', these sensors are then called d_{xx} sensors.
- The bending type is the one sensitive to mechanical strain occurring in a plane perpendicular to a polarisation resulting from a parallel electrical field. If the strain occurs along the y-axis and the electrical field in the x-axis, these sensors will then be called d_{xy} sensors.

3.2.4 Actuators

The functionality of an actuator is solely based on inverse piezoelectricity, i.e. the actuator exhibits mechanical strain following the application of an electrical field. There are three types of actuators [65]:

- As for the sensors, the axial types are the d_{xx} mode.
- The transversal type is the one sensitive to electrical field parallel to the direction of polarisation but generating a displacement perpendicular to the direction of polarisation. They are the d_{xy} - mode.

- The bending type is also is the one sensitive to electrical field parallel to the direction of polarisation but generating a displacement in a plane perpendicular to the direction of polarisation. But these are also called d_{xy} – mode

3.2.5 Transducers

A transducer is a product that exhibit both the piezoelectricity and reverse piezoelectricity. The transducers will respond both to electrical signals and mechanical strain.

3.2.6 Typical applications

In engineering, sensors are used in applications such as conventional ultrasonic testing (UT) for the non-destructive testing (NDT) of plate ^[69-72] and pipe wall thickness ^[73-75] and welds ^[76-81]. In acoustic-emission (AE), sensors are used well beyond the scope of inspection of plates ^[82-85] and pipes ^[86-87]. With AE, the sensors can be further used on structures such as heat exchangers ^[88-89] and rails ^[90-94]. Like the sensors used in conventional UT and AE, guided wave testing sensors are used for the NDT of plates ^[95-97], pipes ^[98-104], heat exchangers ^[105] and rails ^[48-49, 106-107]. These sensors have further benefited the research work on guided wave testing of steam generators ^[108-109] and multiwire cables ^[47, 110-113]. As acousto-ultrasonic (AU) is a combination of AE and conventional UT, it can be stated that the AU sensors can be used for the NDT of plates, pipes, welds and heat exchanger. In recent years, there has been a surge in the usage of AU sensors for the inspection of composite laminates ^[114-119].

3.3 Baseline subtraction approaches to damage detection

In recent years, the baseline subtraction technique has been widely used in structural health monitoring methods using guided ultrasonic waves. This technique consists in collecting a very first dataset (baseline data or signals), at any time and state of the material, and then consist in subtracting it from every signal subsequently recorded during a monitoring period, which can

last for years. The subtraction is continuously carried out until the residual signal starts showing changes. This will further be demonstrated in the sixth chapter of this thesis.

The advantage of the baseline subtraction is that it allows removal of any known features from the data analysis process, so the focus is only on unexpected changes in ultrasonic signals. These changes could indicate the presence of anomalies. But as interesting as this technique sounds, it is not without challenges. Some parameters can affect the reliability of the data interpretation: the environmental and operational factors. For example, temperature ^[120-123], which can cause changes in wave velocities and signal amplitudes. These changes can create anomalies in the residual signal, which in turn can mistakenly suggest the presence of a defect. Another important environmental factor is load variability which can affect ^[120, 124] the elastic properties of a material therefore, causing changes in wave speed thus in ultrasonic signals collected overtime. Load variability can also affect the state of a damage, making it appear worse or better than its actual severity. Wet conditions ^[120, 125], as well as inner pressure or water flow rate in pipes, can influence ultrasonic signals. The operational factors affecting the data interpretation could be the degradation of a transducer over time, a change in the coupling conditions or transducers have become disconnected.

Numerous methods are available for compensating unwanted effects on the residual signals resulting from the baseline subtraction method: for temperatures compensation, the most common methods are (a) the optimal baseline subtraction ^[120-121, 126], which consists in recording as many baseline signals as possible which in turn, will be compared to subsequent signals, in order to identify signals which match the most; (b) the baseline signal stretch ^[120-121, 126] which aims to match the signals to the baseline by either extending or shortening the signals. Researchers also use the Damage Index Method (DIM) to counteract the effects of temperature. Other workers have used less common methods or techniques born from their research work: a

temperature-velocity model ^[123] was developed to predict velocities changes and to take these into account during subtraction process; a technique ^[127] called sparse estimation of guided wave signals, which consists in determining a factor called the estimation error. This factor is obtained from a set signals recorded during the same environmental and operational conditions. It was reported that a high estimation error will indicate the presence of a damage; other researchers ^[128] applied the baseline subtraction to the frequency-wavenumber domain, in order to spot signals resulting from mode conversion caused by the presence of a damage.

3.4 Composite defect detection based solely on the transmitted S_0 mode

3.4.1 Detection via the amplitude and velocity of the transmitted S_0 mode

Detection methods solely based on the transmission of the S_0 mode are popular in the literature ^[129-146]. One of the main reasons for this choice is that the S_0 mode is generally non-dispersive at lower frequencies. It is also reportedly the most suitable wave mode for detection of delaminations as its velocity highly depends on in-plane stiffness which is disrupted by delamination flaws ^[129].

One of the detection methods observed from the literature consists in transmitting only the S_0 mode so its interaction with defects can be isolated. Researchers, such as Tan et al. ^[130], based their detection technique on a pitch-catch test configuration which involved a fixed transmitter and mobile receiver. Tan ^[130] called their technique the *Lamb Wave Point* which aimed to detect delaminations by executing the pitch-catch technique followed by conventional Pulse-Echo Ultrasonic Testing method. They mainly tested unidirectional (UD) carbon fibre reinforced polymer (CFRP) laminates in which they introduced circular-shaped Teflon peel-ply (60mm diameter) to simulate the delamination. The Teflon peel-ply was inserted in several UD laminates to test different delamination depths. The waveform generator Krautkramer USD 10 was used to drive a 0.5MHz rectangle probe (the transmitter) which was set at a specific angle

(20°) to enable pure transmission of the S_0 mode. The receiver on the other hand, was a normal incidence 5MHz probe, 6.25mm diameter probe. The Pitch-Catch was conducted by first placing the pair of transducers (transmitter and receiver) in line with the defect but above a healthy area. The transmitter was fixed for the entire duration of the scan but the receiver was mobile, until it hovered and passed the defect. The specimen was made of 30 plies and the dimension were 300*220*4.59mm. Various interfaces (2nd and 3rd, 4th and 5th, 8th and 9th, 10th and 11th, and 20th and 21st layer) were investigated as flaw sites and Tan ^[129-130] reported that, apart for the defect located between the 20th and 21st layer, test results showed that the Pitch-Catch technique alone was sufficient for detecting each of the 60 mm diameter Teflon inserts. The simulated-delamination was detected by monitoring the amplitude of the S_0 mode throughout the tests. The detection was characterised by observing a drop in the amplitude of the received S_0 mode when the receiver was over the Teflon. The defect length was determined by estimating the distance over which the amplitude drop occurred. The size of the delamination was further confirmed with the Pulse-Echo technique, using a normal incidence 15MHz/5mm probe. The period over which an echo is reflected by the Teflon corresponded to the size of the defect (60mm). In this particular case ^[129-130], the pitch-catch and pulse-echo results returned the correct delamination size (60mm). For the pitch-catch configuration, it was noted that the intensity of amplitude drop was affected by the delamination depth, meaning the furthest the delamination was from the surface of inspection, the smallest the amplitude drop. The pitch-catch technique lost sensitivity over increasing delamination depth. Tan ^[129-130] reported that the technique was 98% accurate up to the fourth layer and 95% up to the tenth layer (third of the laminate thickness). Although the *Lamb Wave Point* technique sounded very promising, Tan's technique has pros and cons: it shows that the delamination can only be detected if it is

directly under the transducer, making this technique more suitable for follow-up inspections but, the advantage is that the technique could detect delamination at various interfaces.

This pitch-catch test configuration (fixed transmitter – mobile receiver) was further tested on delaminations induced by impact damage. Toyama et al. ^[131] looked at such defects within CFRP cross-ply laminates (300x 300 x1 mm). In this specific case, the impact-induced delamination was created by dropping a weight of 1.5 kg at a height of 0.5 m. The tests were carried out using the Agilent (3350 A) function generator to excite an angle-probe transmitter (0.5 MHz) with a Hamming window containing a five-cycle tone burst signal, with a centre frequency of 0.3 MHz). The receiver was an AE sensor (4 mm diameter). Like Tan, Toyama used the “fixed transmitter - mobile receiver” technique to estimate the size (here the length) of the impact-induced delamination. The receiver captured the transmitted S_0 mode before (i) it reached the damaged area, (ii) above the delamination and (ii) passed the delaminated zone while returning to the healthy area. Here again, a drop of the maximum peak amplitude of the transmitted S_0 was observed when the receiver was above the delamination. Toyama also presented an alternative way to detect and size the delamination. He used the GWT pitch-catch technique to monitor the arrival times of the S_0 mode. He used a pair of transducers but this time, they were both mobile by maintaining a set distance (210 mm) between the transducers. They were simultaneously moved with an increment of 5 mm and perpendicular to the direction used in the “fixed transmitter - mobile receiver” technique. When the delamination is present between the transducers, the time of arrival of the S_0 mode is delayed (in comparison to the healthy region) until the pair of transducers moved away from the damaged area. The distance over which the delay occurred, corresponded to the delamination width. The test results indicated that the induced-delaminations were 42 mm long/25 mm wide and 61 mm long/10mm

wide in the $[0/90_3]_S$ and $[0/90]_{2S}$ respectively. Conventional C-scan was further used and validated the test results.

Toyama^[131] further complement the *Lamb Wave Point* technique (Tan's technique) by showing that the delamination can be detected without prior knowledge of its location but, the defect will need to be between the transducers in order to be detected. Also, the "mobile transmitter/receiver" technique was not tested for different delamination depths. The detection of delaminations was characterised by a change in the amplitude and velocity of the S_0 wave mode. Although Tan and Toyama both focussed on delaminations, other types of defects (such as fatigue damage) can have the same effect^[132] of the S_0 mode. Various theories were discussed to figure out the reasons behind the amplitude drop of the S_0 mode: Some researchers said that the delamination splits the material into two regions and the receiver only records the amplitude of the S_0 mode travelling in the media located between the transducer and the delamination. Other workers added that the amplitude drop could be due to mode conversion caused by the delamination, which would reflect and partially convert the S_0 mode into the A_0 mode. This mode conversion phenomenon is further explained in the next section.

3.4.2 Detection via the conversion of the S_0 mode

Guo et al.^[133] also concentrated their study on the first order symmetrical mode (S_0) and the outcome of its interaction with a delamination. This interaction was first numerically simulated by using finite element analysis. The model represented a 2D cross-ply laminate, containing 8 layers $[(0/90)_2]_S$, 300mm long and 1mm thick. Stress-free boundaries and plane strain conditions were applied. A 10 mm long delamination, inserted between the first and second layer, was placed between the transmitting and receiving points. The laminate was excited with a 5 cycle wave signal, 0.5 MHz sinusoidal tone burst modulated with a Gaussian window. The model outcome showed that other modes were present in the material as well as the S_0 mode.

By applying the two-dimensional Fast Fourier Transform (2DFFT) method (used with 32 data points collected with an increment of 1mm) they demonstrated that the S_0 mode was partially converted into the first order anti-symmetrical wave mode (A_0). It was concluded that delaminations has induced mode conversion. Their investigation was further validated experimentally by scanning two specimens similar to the one used in the numerical model: 8-layer cross-ply laminate, also 1 mm thick but 290 mm long, 90 mm wide. One specimen was defect free and the second contained a delamination which was added across the width during its manufacture (by autoclave). The delamination was created by adding a release agent between the first and second layer of the laminate, but was twice as long (20 mm long) as the defect simulated in the numerical model. A 4 MHz/10 mm diameter probe was used and only the S_0 wave mode was generated at an incident angle of 27° . A 0° probe was used as a receiver in order to broaden the number and type of detectable wave modes. The excitation signal was also different from the one used in the model: here the signal was a 10-wave cycle (instead of 5) but still 0.5 MHz sinusoidal tone burst in a Gaussian window. The transmitter and receiver were facing each other and the delamination was between the two, with the receiver placed 10 mm away from the delamination. The 2DFFT method was used on 64 data points collected with an increment of 0.5mm. Test results from the healthy and delaminated specimens were compared and they agreed with the numerical model: the delamination partially converted the S_0 mode into the A_0 mode.

Staszewski ^[134] et al. also looked at the conversion of the S_0 mode caused by an impact-induced delamination. He used different transducers than Guo ^[133]. He used piezoceramic transducers for transmission and a PSV-400-3D laser vibrometer for measuring the waves at the sample surface. The excitation frequency was lower than in the previous case, as the laminate was thicker (7 mm). Staszewski tested a UD CFRP laminate with lay-up different again from the

previous laminate studied by Guo (which was cross-ply). Despite these differences, Staszewski reported that an impact-induced delamination would also cause a conversion of the S_0 mode. The literature indicates that using the 2DFFT method is currently the most reliable experimental method to confirm mode conversion and to measure the proportions of wave modes in a structure. The advantage in using the mode conversion method for defect detection is that it will not require mobile transducer/receiver or for the location of the delamination to be known. This detection method still requires further investigation. For example, it is not known how the through-thickness location of the delamination affects the proportion of the mode conversion to the A_0 mode. It is also not known if the nature of the A_0 mode transmitted by the delamination could be measured to provide information about the defect size. This method will indicate the present of the flaw but will not help an operator deciding whether it is safe or not to continue operating the structure. It has at least got potential as a screening technique.

Against some of the findings from the literature ^[135-139], i.e. delaminations will convert an S_0 mode into an A_0 mode, Su ^[140] reported that the S_0 mode could be converted into modes other than A_0 . He used three 8-ply CF/EP orthotropic woven beams in which he separately introduced a 50 μ m thick polyimide film (effectively a delamination): (a) 21 mm long, 190 mm from the beam left edge and 0.1 mm deep; (b) 19 mm long, 250 mm from the beam left edge and 0.1 mm deep and (c) 17 mm long, 210 mm from the beam left edge and 0.3 mm deep. He tested the material with two PZT elements bonded to the laminate 350 mm apart and 60 mm away from the edges. He used an Agilent E1441 system with an PiezoSys EPA-104 amplifier to respectively drive the transmitter and amplify the signal output. The acquired data were conditioned and digitized using an Agilent E3242A and an Agilent E1437A. The data were processed with artificial neural network-ANN method. Su ^[140] reported (against results reported by many authors) that when the S_0 mode encounters delaminations, mode conversion still

occurs, but in this case the SH_0 was generated by the delamination instead of the A_0 mode. Unfortunately, like many other authors, he didn't use any known techniques to validate his findings. Well known signal processing methods such as 2DFFT would have verified his results. It was also further reported ^[141] that an S_0 mode encountering a delamination can also be converted into higher order modes such as the A_1 mode. It is not very clear what delamination parameters can affect the type of wave modes the S_0 mode will be converted into.

Returning to Guo's case ^[133], although the delamination was always between the transmitter and receiver, with the right transmitter-receiver array, it is likely delaminations could be detectable even if they are not between the transmitter and receiver. This was further reported by researchers such as Hu et al. ^[142-143].

3.4.3 Detection via the reflection of the S_0 mode

Other researchers ^[142-146] looked at detecting defects by simply monitoring the S_0 mode reflected by flaws. For example, Hu et al. ^[142-143] studied how to detect delaminations of various lengths (90, 70, 50, 30, 20 and 10mm) – all 10 mm wide - using only the S_0 mode and without referring/depending on any healthy baseline signals. The study was conducted numerically and experimentally. Hu tested a $[0_{10}/90_{12}/0_{10}]$ CFRP beam, 1005mm long, 10mm wide and 4.8 mm thick. The delamination under investigation was a Teflon film of 25 μ m thickness inserted between the 10th and 11th plies. He used a pair of circular PZT actuators (10mm diameter/0.5mm thick) as transmitter and receiver. The transmitter and receiver were 455 mm apart. In this study, not only was the delamination not between the transducers but was located 320 mm from the receiver (i.e. 775 mm from transmitter). The material was excited at 100 kHz with a pulse signal of 5 cycles with output peak to peak voltage of 10 V peak to peak. Hu reported that apart from the 10x10mm delamination, all delaminations were detected, although he only published experimental results from the 30x10 mm delamination. He explained that not only was the

transmitted S_0 reflected by the delamination but it was also converted into the A_0 mode. He stated that only one end of the delamination would be detected. He stated that when ultrasonic waves propagate from a healthy or high bending stiffness region to a delaminated/lower bending stiffness area, the reflection will be weak. He added that the opposite induces a high reflection i.e. from low bending stiffness to higher bending stiffness region. This statement was not demonstrated mathematically. Although his test set-up was only tested for one delamination depth, he demonstrated that the transducer is not required to be above or near the delamination in order to detect it and also the defect doesn't need to be between the transmitter and receiver. However, like all testing methods reported so far, Hu's detection capability has limits: all techniques based solely on a pure S_0 mode transmission have reportedly not been suitable for the detection of mid-plane delamination. The mid-plane is known as a "zero-shear stress" interface and a delamination at this location will not disrupt the S_0 mode. The A_0 mode does not suffer the same blind spot and has the potential for mid-plane sensitivity. It might not be ideal since it tends to experience higher attenuation than S_0 (reportedly up to three times the S_0 mode's attenuation in some cases), but its use would compensate for the limitation of the S_0 mode. At low frequencies where only a few modes exist, the A_0 mode also is preferable due to it having a shorter wavelength than S_0 (for the same frequency). For an ultrasonic wave mode to detect a defect, its wavelength needs to be at least half of the defect size. Therefore, the A_0 mode should be sensitive to smaller defects than the S_0 mode. Section 3.3 describes the methods based on the pure transmission of the A_0 mode for the detection of composite defects.

3.5 Composite defect detection based solely on the transmitted A_0 mode

Many researchers ^[147-155] have investigated the interaction of the A_0 mode with composite defects. Workers such as Ramadas ^[147], Moreno ^[148], Chiu ^[149], and Wang ^[150] are among the group of researchers who investigated the interaction of the A_0 mode with delaminations. In all

cases, the delamination was always located mid-plane but was manufactured by using either Teflon film ^[147, 149], cardboard ^[148] or non-adhesive polyimide film ^[150]. The studies were focused on quasi-isotropic and unidirectional laminates and the equipment used for the transmission and reception of waves varied across air-coupled probes, PZT transducers and 3D laser vibrometers. Ramadas et al. ^[147] conducted two types of tests: For the three quasi-isotropic CFRP laminates, respectively containing a delamination of 40 mm * 95 mm, 20 mm * 95 mm and 10 mm * 95 mm. B-scans were collected from a pitch-catch test configuration. Both transmitter and receiver were simultaneously moving in parallel to the delamination width, with an increment of 1 mm and while maintaining a distance of 85 mm between the transducers. Tests started in a zone outside the delaminated area, until the receiver reached the damaged area and then the transmitter. The transmitter-receiver pair kept moving by an increment of 1 mm until the receiver first reached outside the damaged area, then the transmitter. For this configuration to work, i.e., defect to be detected, the transmitter and receiver would need to be above the delamination. This configuration was used to estimate the delamination width. A relationship between the size of the delamination, the transducers spacing and diameter of the probe was established in this case:

- When the transmitter-receiver pair of transducers is scanning the material, as long as they are above a healthy area at the same time, the wave velocity will remain the same. When the receiver is above the defect, it collects signals in a less thick area (due to the delamination) which causes the velocity to be reduced. From the B-scans Ramadas reported that the distance, over which the velocity was reduced, was equal to sum of the delamination size and the diameter of the probe.
- When the transmitter-receiver spacing is smaller than the defect, there will be a point when both transducers are above the defect for a certain period of time. Ramadas

reported the delamination size correspond to the sum of the transducers spacing, the probe diameter and the distance over which the wave velocity is constantly reduced

- When the transmitter-receiver spacing is equal to the delamination size, there will never be a point when they will be simultaneously above the defect. Therefore, the delamination size will always be the deduction of the diameter probe from the distance over which the velocity was reduced.

In summary, Ramadas' ^[147] work showed that the change in the A_0 mode velocity indicated the presence of the delamination and when this velocity change was closely monitored, it provided further information on delamination size. It was concluded that the delamination size was a function of the transmitter-receiver spacing. As for most of the techniques discussed so far, this technique will be more suitable for follow up inspection as the probes will need to come across the delamination in order to detect and size it. Moreno ^[148] (despite providing very little information on his work) also described that a delamination (created this time with cardboard) was detected by observing a decrease in the A_0 mode speed. Rheinfurth ^[156] further explained the change in the A_0 wave velocity and reported that it could also indicate presence of cracks. He carried out tension-tension, tension-compression and compression-compression tests on 8-ply quasi orthotropic glass fibre coupons (250 mm * 25 mm * 2 mm) using servo-hydraulic machine at a frequency of 6 Hz. The signal excitation and data acquisition were carried with incident and air-coupled transducers coupled with the ultrasonic system RAM-5000 SNAP from RITEC. The transmitter was driven with a 10-cycle toneburst signal with a centre frequency of 207 kHz. Rheinfurth ^[156] reported that the largest decrease in the A_0 wave velocity occurred during the tension-compression test. The decrease reportedly coincided with the degradation of the Young's and shear moduli (E_{11} and G_{12}) in the $\pm 45^\circ$ & 90° plies. When cracks reached the centre of the coupons, the decrease of the A_0 wave velocity was reportedly

further caused by the decline of G_{23} in the $\pm 45^\circ$ & 90° plies. Rheinfurth^[156] finally suggested that by monitoring the moduli E_{22} , G_{12} and G_{23} (via the velocity of the A_0 mode), cracks could be detected as these moduli are functions of the crack density, δ , times ply thickness. The issue with Rheinfurth^[156] report is that he didn't validate his work with conventional methods. He didn't check whether there was more than one defect type in the laminate. Other defects (such as delamination) could have existed and mainly caused the decrease of the A_0 speed. As a consequence, his results could be considered inconclusive.

Unlike the methods presented above and based on the monitoring of the A_0 wave velocity, Chiua^[149] looked at the A_0 mode amplitude and its scattering behaviour. He also showed that the mid-plane delamination does not require to be between the transmitter and receiver in order to be detected by the transmit A_0 mode. He tested a CFRP quasi-isotropic laminate for the detection of a semi-circle delamination (Teflon) inserted at the edge of the laminate. Chiua inspected five different size from 1.5 mm to 6 mm with 0.75 mm increment. He used a PZT 26 disc (5 mm diameter/2mm thick) as transmitter and the 3D laser vibrometer as a receiver. The A_0 mode was transmitted along the 45° direction, far from the centre of the delamination, at a distance 10 times the A_0 wavelength. Data were collected at a distance 4 times the A_0 wavelength, following a semi-circular path with 10° increments. Therefore, the delamination was never between the transmitter and receiver. Nineteen measurements in total were taken. He reported that with larger delamination size, the scatter was increased and focused toward the fibres perpendicular to the direction of the transmitted A_0 mode. Through his technique, Chiua showed that a mid-plane delamination is not required to be located between the transmitter and the receiver in order to be detected. The downside with his technique is the use of the 3D laser vibrometer which is not suitable for practical inspection scenarios since it is a fragile and expensive laboratory tool. Sohn^[157] also monitored the amplitude of the transmitted A_0 mode

but this time against impact damage. He reported that the A_0 mode amplitude was increased by a 30 mm long, impact-induced delamination. At first, this was an interesting result as it was for an impact-induced delamination which could occur at any interface. His findings would have demonstrated that delaminations could also be detected at any other interface with the A_0 mode but with lack of evidence of the through thickness position of the defect, it is not possible to conclude that the impact-induced delamination caused an increase. It could be that the matrix/fibre cracks caused the increase or the A_0 mode was partially converted into another mode.

Wang et al. ^[150] looked at detecting the onset of a delamination during interlaminar fracture tests also using the propagation of the A_0 mode. His idea was based on newly developed formulas which required three wave parameters to be plotted against the laminate displacement. They also required to be compared with peak values from conventional methods used for assessing interlaminar fracture toughness, namely NL (deviation from linearity), VIS (visual observation) and MAX (maximum load). The three defined (delamination-sensitive) wave parameters were the velocity change (VC), the magnitude change (MC) and the correlation coefficient (CC). Wang ^[150] tested unidirectional CF/EP beams (245*25*3.6 mm) in which Mode I & II edged delamination (100 mm long and 50 μm thick non-adhesive polyimide film) were inserted. Mode I strain energy release (G_{IC}) was created following the standard ASTM D5528-01, using the Double Cantilever Beam (DCB). Mode II strain energy release (G_{IIc}) was created through the ESIS protocol for interlaminar fracture testing of composites via the End Notch Flexure (also known as three-point loading). He used rectangular PZT Piezoelectric elements which were driven with the Agilent E1441A Waveform generator. A 5-cycle signal in a Hanning window was generated at 30 kHz and data was collected at a sampling rate of 5.12MHz. The Interlaminar Fracture Tests for Mode I & II delaminations were carried out at a

cross-head rate of 1 mm/min using the Instron 5567n. The transducers were set in a pitch-catch configuration and mounted on opposite surfaces at the right and left edges of the CF/EP beam. For the DCB (Mode I delamination) tests, Wang reported that the peak of VC, MC, CC matched major changes from the load-displacement curve (NL, VIS, MAX). Only one peak value for each VC, MC and CC was observed per load-displacement curve. For the VC and CC curves, values were stable until a sudden and continuous drop which corresponded to the onset of the delamination and its growth. For the MC curves, the value dropped steadily during the tests until the onset of the delamination which would cause the amplitudes to stabilise. For the ENF (Mode II delamination) tests, two key points were observed for VC, MC and CC per load-displacement curve. These key points corresponded either to the peak or the trough of the VC/MC/CC values. The first key point (for each VC, MC and CC) marked the onset of the delamination and coincided with the NL/VIS/Max parameters, while the 2nd point showed the displacement at which the delamination propagated up the area with the highest stresses. Wang's technique provided good coverage and there was no need to move the transducers, which were actually permanently attached. The technique was validated by conventional methods used for assessing interlaminar fracture toughness and it had potential suitability for practical industrial situations, but the downside is that the technique will not provide details on defect location and or size. It would only inform the operator of the onset of the delamination.

All tests methods summarised so far, are in favour of the fundamental Lamb wave modes, generated separately. As previously reported, the S_0 and A_0 modes could be used in a complimentary fashion for detecting defects. Therefore, it is not surprising that other researchers used both Lamb wave modes at once and in the same test configuration for defect detection.

3.6 Composite defect detection based on the S_0 and A_0 wave modes transmitted at once

3.6.1 Monitoring of elastic moduli reconstructed from the S_0 and A_0 modes velocities

Material moduli are good indicators of the health of a structure and it is already known that that compliance coefficients are proportional to wave displacement and velocity. Therefore, it is not surprising that researchers tried to assess a material's health via elastic moduli in relation to their influence on wave parameters. Damage such as thermo-oxidative ageing was investigated. Gelebart ^[158] manufactured this damage by inserting an 8-ply carbon epoxy and orthotropic laminate ($[0^\circ/45^\circ/-45^\circ/90^\circ]_s$) in an oven for 3500hrs and at two separate temperatures: 160°C and 180°C . The ageing was reportedly materialised by cracks initiating at the surface and propagating perpendicularly to the laminate surface. He used a chirp signal (1 MHz central frequency) to drive air coupled/angled transducers (Ultran NCT1010 transducers) which were mounted to the laminate 30 mm apart but on opposite surfaces of the plate. Gelebart ^[158] reported that numerical results showed that a decrease (up to 20%) of the elastic moduli C_{55} value measurably affects the velocity of the S_0 and A_0 modes. FFT was used to estimate the velocity of the fundamental Lamb wave modes in healthy and damaged plates. It was experimentally demonstrated that ageing affect C_{55} and that through the measured velocity values of the S_0 and A_0 modes, C_{55} can be monitored and estimated. Vishnuvardhan ^[159] further demonstrated to what degree all nine coefficients of the compliance matrix of an orthotropic material are linked to the velocities of the S_0 and A_0 modes. He made this conclusion following the testing of a 21-layer unidirectional graphite epoxy, quasi-isotropic laminate which was impacted with two distinctive loads (16 J and 13 J) that created two delaminations (reportedly $40*40$ mm and $30*40$ mm respectively). He conducted the research work by first calculating the material elastic moduli from the S_0 wave velocity using a *Genetic Algorithm*-based inversion method. Piezo wafer-active sensors (APC 850) were used as transmitters and

receivers. The sensors were driven using the MATEC PR5000 and the excitation signal was a 2 cycle tone burst (unlike a 5 to 10 cycles typically used by others) centered at 200 kHz. The measurements were taken by monitoring a quadrant of the material; a single transmitter was placed at the centre of the quadrant within a two-ring sensor array. These two rings were respectively at 80 mm and 120 mm from the transmitter. This pitch-catch configuration was carried out only to determine the material elastic moduli. To add to Gelebart's ^[158] research work, he stated that C_{44} and C_{55} are more sensitive to the A_0 mode propagation compared to the S_0 mode and for the remaining seven coefficients (C_{11} , C_{12} , C_{13} , C_{22} , C_{23} , C_{33} and C_{66}), the opposite was observed. He then attempted to detect numerically and experimentally the two delaminations. He developed an algorithm he called "*Phased Addition*", which was used with the S_0 mode velocity obtained numerically (using the Disperse software ^[53]). He reported that a specimen can be reconstructed numerically, defects included. He carried on validating his model by using an omni-directional piezoelectric wafer active sensor (PWAS) as a transmitter at the centre of a 60 mm diameter circle fully populated with a single ring of 30 PWAS. The two impact-induced delaminations were in the area between the transmitter and the receivers. The 16 J impact damage (40 mm*40 mm) was induced 23 mm from the transmitter at an angle of 180° and the 13 J damage was induced 43 mm from the transmitter at an angle between 180° and 270° . Vishnuvardhan ^[159] reported that the A_0 mode could not be monitored for defect detection because it overlapped with edge reflections but he reported that the Phased Addition Algorithm (PAA) was only successful in detecting the 16 J impact damage. The methods based on the calculation of elastic moduli from the measured wave velocities are appealing as they are based on determining coefficients directly related to the mechanical properties of the laminates. However, both Gelebart ^[158] and Vishnuvardhan's ^[159] work lacked the use of conventional methods to confirm the type of the existing composite defects (especially required

for the impact-damage) and these techniques would not be ideal for defect location and sizing. Furthermore, although reduced elastic moduli would indicate a decrease in the health of the structure, this could also be caused by any type of flaws; therefore, this technique would not be suitable also for defect classification.

Additional research work was carried out to correlate changes in the amplitudes and velocities of the S_0 and A_0 modes with presence of disbonds. Qing-tian ^[160] attempted to numerically assess the quality of a bond between two composites. He modelled a disbond between an 8-layer laminate ($[0/45/-45/0]_s$) and a multilayer structure $[0/-45/90-45]_s$. He modelled disbonds of various thicknesses, lengths, shapes and qualities (poorly bonded or disbonded) and studied their interaction with guided waves using the Hamilton's principle and the semi-analytical finite element method. Although he reported that wave velocities and dispersion would be affected by large disbonds, he did not disclose any further details such as signal excitation characteristics or the type of wave modes he used. The results were not validated. Mustapha ^[161] was also among the workers who investigated the effects of disbond flaws on guided waves. He looked at a disbond (blade insertion) between the skin (a quasi-isotropic $[\pm 45, 0/90]_s$ CF/EP laminate) and the core material (honeycomb and foam) of a sandwich beam. Two distinct defect sizes were studied: 30*20mm and 30*35 mm respectively. He tested the specimen with PZT transducers whose transmitter was driven with a 5-cycle sinusoidal toneburst signal in a Hanning window that was generated by an Agilent E1441 waveform generator. Signals were amplified with a PiezoSys EPA-104 system, received signals were conditioned with an Agilent E3242A system and digitised with an Agilent E1437A unit. The excitation frequency was between 10 and 400 kHz and the acquisition sampling rate set at 20.48MHz. He selected pitch-catch for his research work and the receivers were mounted on opposite surfaces 200 mm apart from the transmitter. Three defect-free sandwich beams were originally tested to study the

conversion of plate guided waves to Rayleigh waves. The excitation frequencies varied from 25 to 400 kHz. Mustapha ^[161] reported that depending on the excitation frequency, 20% to 50% of the transmitted energy will reach the opposite side of the core material. For the defect-free sandwich beams, the results for the honeycomb sandwich showed that both the A_0 and S_0 modes leaked in the structure but only the A_0 was measurable on the opposite skin. For the foam, both A_0 and S_0 modes leaked in the sandwich beam but only the S_0 mode was measurable on the opposite side of the core material. For the defective sandwich beams, the 20 mm thick honeycomb sandwich beam was tested with an excitation frequency of 200 kHz. Results showed when a disbond is present, the amplitude of the S_0 mode increased because the disbond stopped it from leaking into the material. This S_0 mode behaviour was exhibited for the 10 mm thick honeycomb and 20 mm thick foam sandwich structures. The A_0 mode has a slightly different behaviour: its amplitude increased for the 20 mm thick honeycomb but scattering was observed for the 10 mm thick honeycomb and 20 mm thick foam sandwich structures. Mustapha ^[161] further reported that the scattering of the A_0 mode was also noted for the 20 mm thick foam for excitation frequencies above 40 kHz. Experimental results agreed with the numerical simulation which was previously modelled with Abaqus (Dynamic Finite Element).

These results highlight further the difference between disbond and delamination: Disbonds represent the detachment of one structure from another, like the detachment which can occur in wind turbine blades, between the spar cap and the shell of the blade. Delaminations is particular type of disbond, unique to laminates within composite structures. While delaminations have been detected by monitoring the amplitude/velocity/conversion of the S_0 mode, Mustapha reported disbond detection is achieved by monitoring the leaky nature of wave modes. A disbond will stop the signals from propagating from one structure to another i.e. from leaking from one to another components.

Habib ^[162] investigated a more realistic disbond scenario: the quality of a repair patch. The previous disbond was not realistic as it was simulated by the insertion of a blade. In real life, disbonds are more likely to grow from fatigue during service life, poor bond quality and from repair patches. A boron doubler ([0, 0, 45, -45]_s) was placed on both surfaces of carbon substrate (381 mm*50.8 mm*1.016 mm) assembled with a [45, -45, 45, -45]_s ply layup. The repair patch was subjected to a fatigue loading with a maximum amplitude of 1500lbf (6,672 N), a stress ratio of 0.1 and a test frequency of 5 Hz. The aim of his research was to compare guided wave testing with the output of Surface Mountable Crack Sensors (SMCS) during fatigue loading. The guided wave testing was executed using an Acellent ScanGenie, and an Acoustic-Ultrasound system. The excitation signal was a 5 cycle toneburst sinusoid which centre frequency swept from 100 to 350 kHz by steps of 50 kHz. During the fatigue loading, guided wave data were collected every 5000 cycles between 0 and 50000, every 10000 cycles between 50000 and 100000 cycles and every 50000 cycles afterwards. Received signals were analysed using Habib's newly developed method for defect detection and quantification, which he called the Direct Path Image Utility (DPIU) method. For the SMCS, SHM data were collected every 5000 cycles between 0 and 50000, every 10000 cycles between 50000 and 100000 cycles and every 25000 cycles afterwards. The SMCS method, originally intended for metallic crack growth monitoring, can only provide a binary response indicating whether or not a disbond has occurred at the edge of the patch. For the technique to work, sensors need to be mounted on or near the patch for accurate results. SMCS are triggered when their circuit is broken. No further details were provided on the types of sensors, array configuration, or what wave modes and parameters (amplitudes/velocities) were monitored, but he reported that the sensitivity of the Lamb Waves Acoustic-Ultrasound method was 0.15 inch² (96.774 mm²). The

existence of the disbond was further confirmed through visual inspection for defect detection and through A/B/C-scan ultrasound for defect quantification.

3.6.2 Through-thickness displacement caused by the S_0 and A_0 modes

The shapes of displacement through a plate's thickness caused by Lamb waves have not only been numerically modelled [42, 163-164] for healthy isotropic plates but also for healthy composite laminates. The results demonstrate that not only does the frequency-thickness product have an impact on the displacement pattern but the fibre directionality relative to the direction of propagation does too. This is complicated because the fibre directionality can vary with depth. Lee [57] proposed an analytical model to plot the displacements of the S_0 and A_0 modes in an orthotropic unidirectional laminate. Although Lee's model worked for plotting displacement at 0° (along the fibres), he did not demonstrate his analytical model for multi-directional laminates. However, other workers [62, 140, 165] provided modelling results for the displacement of Lamb waves in healthy cross-ply, quasi-isotropic and bidirectional laminates. It was also reported [166] that wave shapes can vary with the angle of incidence at which the ultrasonic waves enter the material.

The displacement of particles can also be calculated in composite materials containing defects. The delamination can be modelled as a media with free boundaries [167-168] (open delamination) or with boundary conditions (closed delaminations [168]). Barouni [168] presented modelling results for a healthy unidirectional GFRP strip and two GFRP strips containing respectively a 10mm and 100mm delamination at mid-span. The results showed that the in-plane displacement of the S_0 wave changed around the delamination; for a 100mm delamination, the in-plane displacement moved from below 5.0×10^{-9} to above 7.0×10^{-8} . In this work, the displacement does not have a unit per say and can be viewed as arbitrary (only the proportionality is of interest). Researchers [42, 51, 57] considered the displacement to be a position relative to a chosen

origin. For a 10 mm delamination, the displacement component shifted further to the right of the displacement scale, suggesting that the delamination could have increased the in-plane displacement. It could be concluded that the smaller the delamination, the bigger the shift of particle movement in the displacement scale. Unfortunately, these results were never validated through experiments, making these finding inconclusive.

3.7 Summary

As previously explained and reported, composites are very difficult to inspect, mainly due to their anisotropic nature which makes wave propagation difficult to manipulate and interpret. Research studies have showed that interrogating these materials at frequencies where only a few wave modes exist significantly reduces the complexity of data interpretation for inspection purposes. The S_0 and A_0 wave modes showed promising results in terms of the detection of defects such as delaminations, impact damage, cracks and disbond according to the literature. The defect detection not only relies on the types of ultrasonic wave modes selected for transmission but also on the data collection technique. For some techniques, the defect would be detected and the size estimated as long as the receiver reached above it or if the defect was located between the transmitter and receiver. For the cases where these requirements didn't apply, defects (mainly delamination) would still be detected but no information on size would be obtained. Defect sizing will only become important if the operator (carrying out the inspection) has been made aware of the greatest defect size acceptable for the structure in service. The presence of defects was indicated by (i) change in the amplitude/velocity/displacements of the S_0 and A_0 modes, (ii) mode conversion, (ii) wave reflection and (iii) reconstruction of the material elastic moduli through the velocity of the fundamental Lamb waves.

SHM has been an important research topic for decades now, as structures continuously require checking in order to detect defects before they cause permanent/irreversible damage. SHM relies on a robust inspection technique capable on operating daily and automatically, not only detecting flaws but also sizing them so the overall health of the structure can be kept in check.

**Chapter 4: TRANSDUCER
DIRECTIONALITY STUDY IN WOVEN
GFRP COMPONENTS**

4.1 Introduction

The study reported in this chapter compares the performance of transducers which are reported to facilitate control over ultrasonic guided waves.

Three transducer types were selected:

1. Thickness-shear PZT elements (d_{51} -type) ^[169]. These are polarised and plated individual pieces as supplied by PI Ceramics GmbH with alumina face plates bonded to them.
2. Thickness-shear PZT elements commercially manufactured within an assembly also comprising an alumina face plate, a stainless-steel backing mass/housing and an electrical socket. These are also d_{51} -type ^[169]. These are known as Teletest Transducers and are supplied by Eddyfi UK Ltd.
3. Macro Fibre Composite (MFCs) transducers which are manufactured and supplied by Smart Material GmbH. MFCs are made of lead-zirconate-titanate (PZT) fibres bonded to each other with epoxy and enclosed by electrodes and polyimide film. The polyimide includes interdigitated electrodes that can apply a field along or across the axis of the PZT fibres, depending on the MFC group type.

Unlike MFC transducers, various forms of thickness-shear elements are more common in commercial applications of GWT. However, MFC transducers have been successfully applied to composites in the literature and have the advantage of being compliant and low-profile.

There are three main types of MFCs made available to the scientific community:

1. The type which expands with applied voltage along the fibres' main axis is the P1-type (also known as d_{33} -type ^[170]).
2. The type which contracts due to electrodes placed either side of the group of PZT fibres is called the P2-type (also known as d_{31} -type ^[171]).

3. MFCs are also available in a version that can have a diagonal flexural motion, which is known as the P3-type (also known as d_{31} -type^[171]).

The type of MFC used in this chapter is the M2814-P1 (d_{33}) type, which has an active area of 28mm (in the fibres' main axis) by 14 mm.

Each of these transducers has a main in-plane axis of vibration. The thickness-shear transducers are uniformly sensitive to in-plane displacement along their axis of vibration (the direction of shear), whereas the MFC transducers are sensitive to strain along their axis of vibration (along the fibre length).

The main goal of this chapter is to study the performance of each of the transducers mentioned above and to observe which ones will be more suitable for practical applications. To compare the suitability of these transducers for composite testing, their GWT directionality was examined within a GFRP woven material typical of the kind commonly used to make the shell part of wind turbine blades.

This characterisation can be achieved by measuring and plotting the group velocity of each possible wave mode as generated from a transducer against direction for a given frequency (these are the so-called directionality plots). In order to successfully establish the directionality plots, it was necessary to design an experiment that allowed measurements of the wave velocity i.e. plotting dispersion curve for each fibre orientation. This needed to be done with the main axis of vibration of the transducers aligned in both the on- and off-fibre directions of the material. Dispersion curves were required because without knowing the velocity of each ultrasonic wave modes, it will be impossible to design the experiment for the directionality plots. Knowing wave velocities allow distancing the transmitter from the receiver to successfully avoid overlapping of the ultrasonic wave modes at the receiving point. Hernandez^[172] developed a numerical protocol for plotting the dispersion curve for composite

materials. Hernandez ^[172] reported that the propagation profile of the SH₀ mode in composite is highly dependent on the lay-up of the material and the orientation of the sensors (Thickness Shear PZT element) with regards to the fibres. Hernandez produced Finite Element models (via Abaqus) of the propagation of the SH₀ mode in a unidirectional, bi- and tri-axial laminates, with cases where the sensor was oriented in directions parallel to the fibres and oriented at an angle to the fibres. Hernandez' results showed that for each case, up to three wavefronts can be observed in the propagation of the SH₀ mode in composites, each with their own velocity. While Hernandez ^[172] conducted experiments to validate a model, this set of experiments described here (different from Hernandez' experiment) was carried out in parallel to verify the dispersion curves obtained numerically. For these experiments, a scanning laser vibrometer was used to collect data while a waveform generator and amplifier was used to drive each transducer. The vibrometer used was a Polytec PSV-400-3D-M and the waveform generator and amplifier was an Eddyfi Teletest Focus+. This setup was used in turn to characterise each of the three transducer types. Knowing the dispersion curves at this stage also allowed focussing on the wave mode separately, to determine their specific and respective transmission directionality. This was done by defining each wave mode time window i.e. by calculating the time of arrival of the leading and trailing edges.

4.2 Experimental protocol

4.2.1 Specimen manufacture

The component (ID Chapter 4_Specimen 001) used for testing was a 3000 mm long, 2000 mm wide and 4.5 mm thick GFRP plate. It was made of six layers, each containing fibres orientated at $\pm 45^\circ$ and arranged in a twill weave pattern. The material properties of the GFRP plate are listed in Table 1:

Table 1: Mechanical properties of Chapter 4_Specimen 001

Density kg/m ³	E ₁ GPa	E ₂ GPa	E ₃ GPa	v ₁₂	v ₁₃	v ₂₃	G ₁₂ GPa	G ₁₃ GPa	G ₂₃ GPa
1800	12.46	12.46	11.47	0.5	0.29	0.29	9.5	4.237	4.327

4.2.2 Scanning Laser Vibrometry for plotting wavenumbers and dispersion curves of a Woven GFRP plate: “ON” and “OFF” fibre signal generation

Laser vibrometry is a non-contact technique where a laser is directed at a point on a sample's surface chosen for measurement. Vibration at the surface causes a doppler shift in the scattered laser light. The doppler shift provides a measurable modulation that corresponds to the surface's velocity (due to vibration) at the point the laser targets. Interferometry is used to extract the surface velocity signal from the measured scattered light. The measurement is simultaneously taken with multiple vibrometry units, which allows a three-dimensional measurement of the vibration at the surface. Since with this measurement technique the surface is not loaded and the signal corresponds directly to the surface velocity, this gives a true measurement of the vibration. Since the behaviour of the transmitted waves is repeatable, multiple vibrometry measurements can be taken over the surface of a sample and used to characterise the waves. The procedure for using the PSV-400-3D-M Vibrometer is reported in Appendix A – Polytec Scanning Vibrometer Instruction.

When the waveguide material of interest is anisotropic, such as GFRP, numerical modelling is often used for generating dispersion curve plots and these are often validated with experimental measurements. The dispersion curve plots for the GFRP plate under study here have already been numerically predicted and results are published in Hernandez' thesis ^[172]. Hernandez^[172] numerical model revealed that at least four wavefronts exist in the excitation frequency range 60-140 kHz: the S₀ mode (3000-3400m/s), the A₀ mode (1000-1200m/s), and two other

wavefronts representing a decomposition of the SH_0 mode: the SH_0 slower wavefront (SH_{01}) and the SH_0 faster wavefront (SH_{02}). The velocities of the slower and faster wavefronts of the SH_0 mode are 1500-2000m/s and 2250-2500m/s respectively. This numerical work provided approximate values which were able to inform the initial position of the transmitter and receiver points chosen for the experiment described here. As is intended for the experimental work, the dispersion curves were numerically predicted for two types of ultrasonic wave generation: excitation in line with the fibres (45°) and at off-fibre direction, as shown in **Figure 4**. For the velocity measurement, only the Thickness-shear PZT element (with a ceramic faceplate but no backing mass) was considered. Its function was transmission only. Preliminary calculations show that as long as the distance between the transmitter and receiver (here the laser vibrometer) was maintained between 240 and 440mm, the fundamental Lamb waves (and reflection from edges) would not overlap. Calculations do not include velocities of the shear waves but calculations predicted that the plate needed to be at least $3000*3000 \text{ mm}^2$ and the distance between transmitter and receiver to be set at a minimum of 690mm, in order to prevent the S_0 mode to overlap with the SH_0 mode.

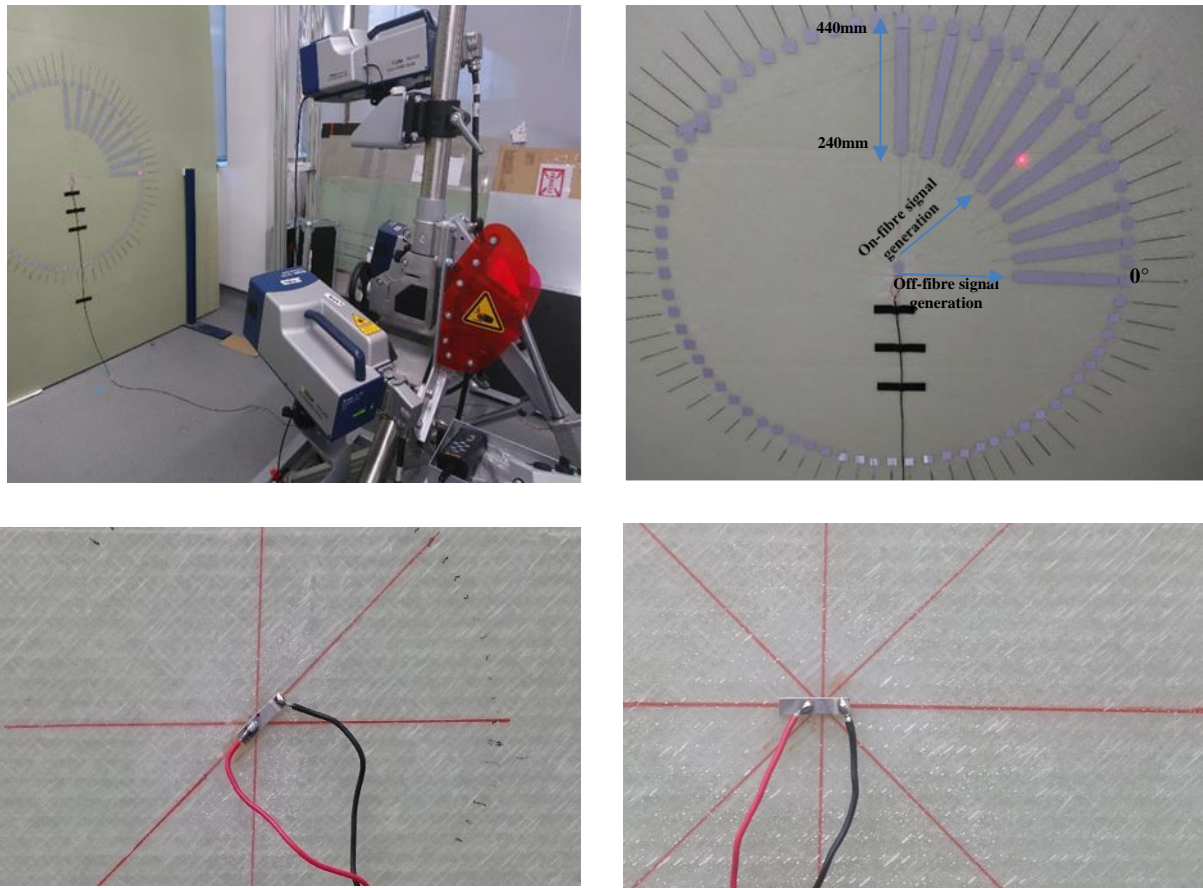


Figure 4 Experimental protocol for dispersion curves with thickness-shear PZT element

4.2.3 Scanner Laser Vibrometry for sensor assessment

The approach to comparing the transmission capability of the various transducers was based on the approach used above to measure the wave mode velocities. Transmission was carried out by a Teletest Focus system for signal generation for exciting the transducers and the PSV-3D-400-M was used for measuring the waves in the sample panel. The location of the transmission point was the same as previous tests (velocity measurements) but the reception increment point was different. Each transducer was used in turn to transmit in the centre of the same 880 mm diameter circle. Transducers were mainly studied with a signal generated along the 45° fibre orientation. Data were collected at a set radial distance of 440 mm from the transmitter with an increment angle of 5° over the range of 0° to 90°.

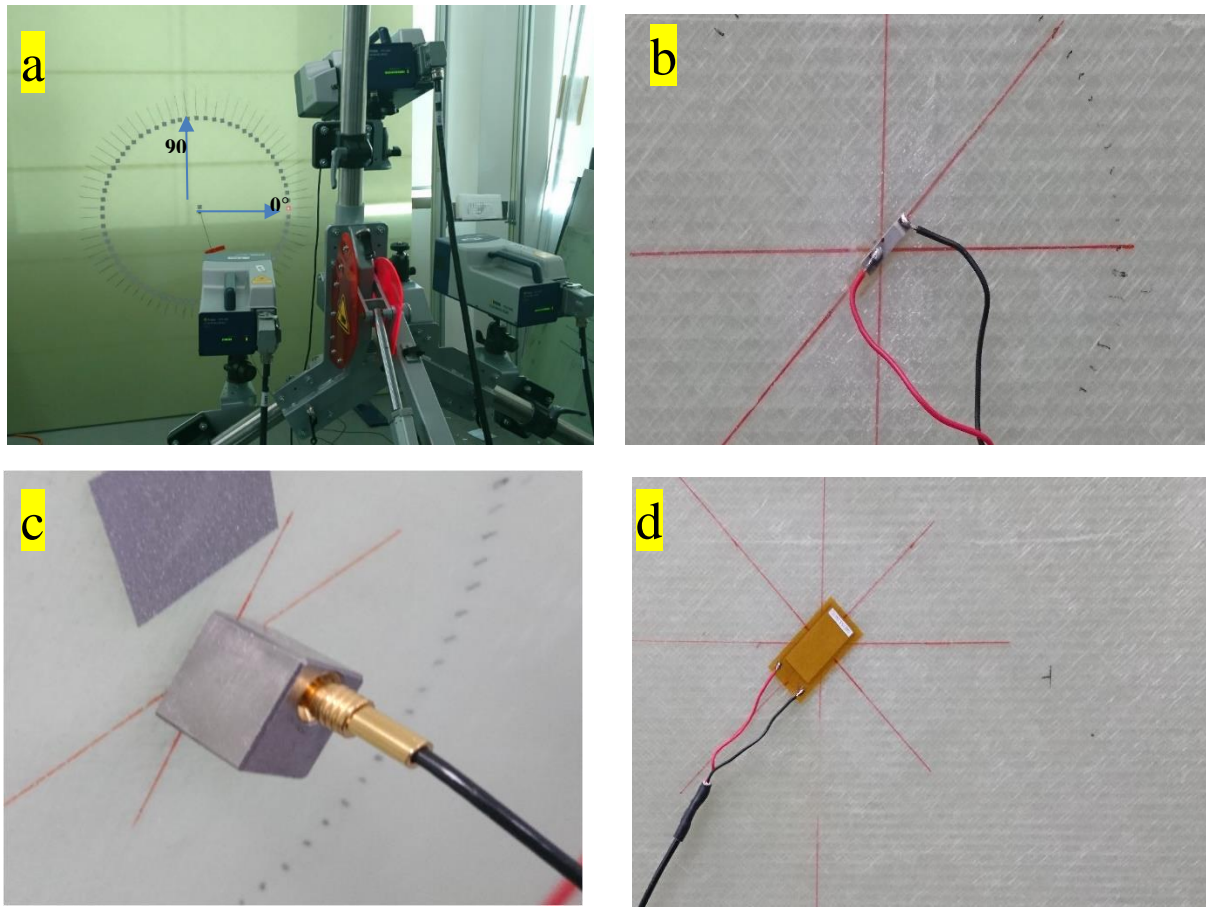


Figure 5 (a) Experimental set up for transducer directionality plots; (Thickness-Shear PZT element); (c) Thickness-Shear PZT element with backing mass; (d) M2814-P1 MFC

The transducers subjected to comparison were the Thickness-Shear PZT element, Thickness-Shear PZT element with backing mass (commercially manufactured and known as Teletest transducer) and M2814-P1 MFC as shown in Figure 5.

In order to remove the transmitter and swap them from another one, transducers were soaked in a localised bath of acetone for approximately 1-3 hours (depending on the transducer) to dissolve the bonding adhesive, shown in **Figure 6**.

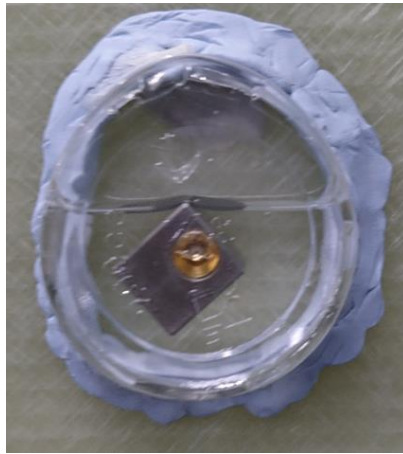


Figure 6: Localised bath acetone

4.3 Data collection and plotting protocols

4.3.1 Wavenumber plots and dispersion curves

Data collection protocol

The Thickness-shear PZT elements was driven by a Teletest Focus waveform transmitter and amplifier. The signal used for transmission was a linear rising chirp with a frequency range from 56 to 140 kHz and a duration of 500 μ s. For reception, 512 repeat signals were averaged on each point of measurement to increase the signal to noise ratio. A high band pass filter was selected and the signals were collected for a duration of 800 μ s. The transmitting PZT element was mounted to the plate using cyanoacrylate adhesive (“super glue”) after the surface was cleaned using sand paper and acetone. The transmitter was placed at the centre of the 880mm circle diameter. Vibrometry data were collected from one quadrant of the plate with an increment of 10° between measurements from 0° to 90°. For each angle, an average of 155 points (for the on-fibre data) and 157 points (for the off-fibre data) were collected radially (the axis of wave propagation) from a distance of 240 mm from the transmitter up to approximately 440mm, as shown in Figure 4.

Data plotting protocol

The dispersion curves were calculated by applying the two-dimensional Fast Fourier Transform (2DFFT) method to 155 (on-fibre data) and 157 (off-fibre data) points collected at each angle. Therefore, 10 sets of dispersion curves were calculated for various fibre orientation around the transmitter. The 2DFFT method yields plots where colour is used to represent magnitude plotted over a Cartesian space where the two axes are frequency and wavenumber. As explained Chapter 2 of this thesis, wavenumbers represent the number of wavelengths per meter or per second^[42]. Since a broadband transmission was used, each wave mode is expected to exist as a curve over the frequency/wavenumber space and the curve is expected to appear as a ridge of colour. How distinctly clear each ridge appears depends on the number of samples taken, the range over which the samples were taken and the signal to noise ratio of the measurements. Dispersion curves can be extracted by fitting curves to the observed ridges. For the experiments, the number of samples taken was 155 on-fibre and 157 off-fibre; the range over which the samples were taken was 200 mm. The signal to noise were not calculated but was visually assessed.

The three-dimensional vibration signals collected by the PSV-3D-400-M are associated with the Cartesian axes (in the plane of the plate's surface). However, since the waves propagate radially from the transmission point, the main axes of interest are the radial axis (the main axis for Lamb vibration) and the circumferential axis (the main axis of vibration for shear horizontal modes). In order for Lamb and shear horizontal modes to be distinctly measured, it was necessary to convert the Cartesian based results to the equivalent using polar coordinates.

Figure 7 shows an example of A-scans in the Cartesian coordinate form and their results in the polar coordinate form.

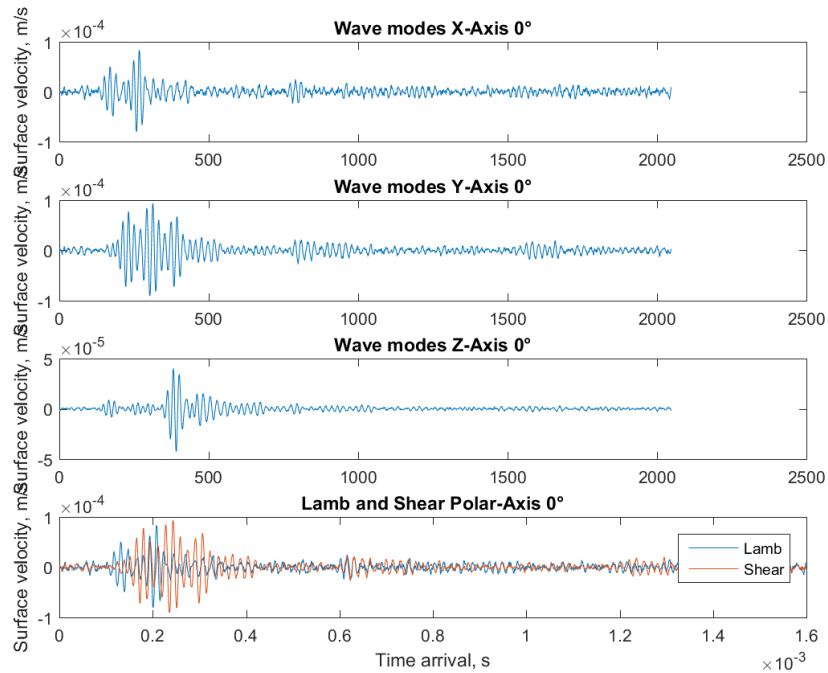


Figure 7 A-scans in the Cartesian and Polar coordinates, for signal transmission parallel to the fibres and collected off-fibre direction - 66kHz excitation frequency

Wavenumbers for the “ON-FIBRE” signal generation were calculated from data collected between 0° and 90° (with an increment of 10°). The fibres were orientated at 45° from the X-axis of the GFRP plate as shown in **Figure 8**.

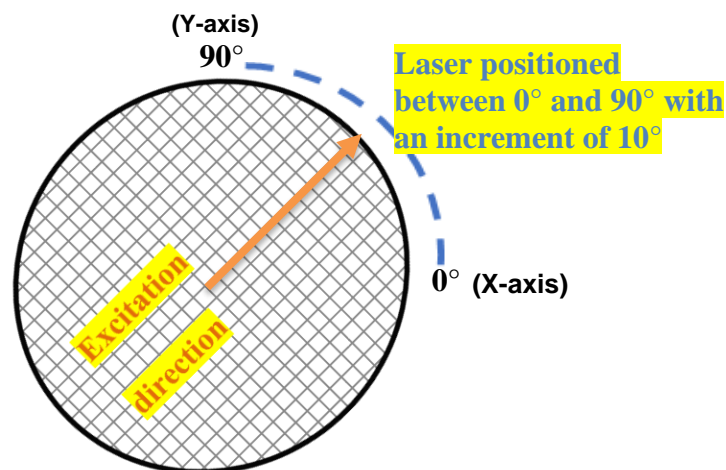


Figure 8 Data collection diagram for on-fibre (45°) signal excitation

Wavenumbers for the “OFF-FIBRE” signal transmission were also calculated from data collected between 0° and 90° (with an increment of 10°) but for signals generated in line with the X-axis of the plate, as shown in **Figure 9**.

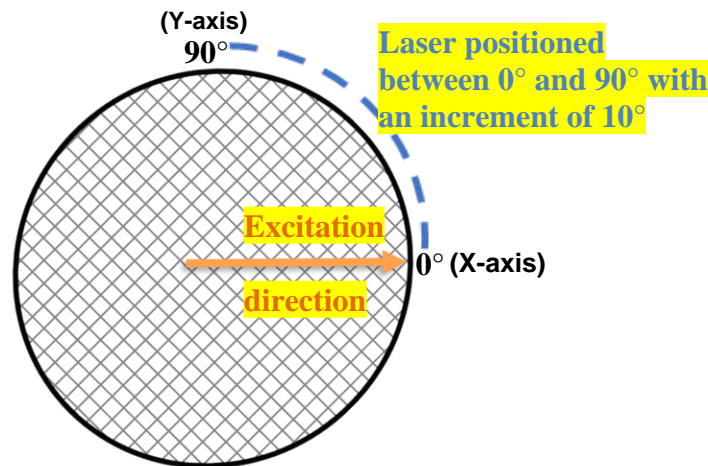


Figure 9 Data collection diagram for off-fibre (0°) signal transmission

4.3.2 Sensor assessment

Data collection protocol

The transducers were driven with a 5-wave cycle signal enclosed in a Hanning window. A sweep frequency was carried to data collection for excitation frequencies varying from 66 kHz to 130 kHz with an increment of 4 kHz. As previously stated, these signal excitation parameters will ensure separation of the fundamental Lamb waves, as long as the laser vibrometer is set at a distance range 240-440 mm from the excitation point. The data acquisition was similar to the process for the wavenumber plot/dispersion curve, with the duration of the data collection (sampling time) changed from $800 \mu\text{s}$ to $1600 \mu\text{s}$ instead.

Data plotting protocol

The protocol is the same as the one used for the wavenumber plots.

4.4 Results and discussion

4.4.1 Wavenumbers and dispersion curves of a Woven GFRP plate: “ON” and “OFF” fibre signal generation

Wavenumber plots for the “ON-FIBRE” signal generation

Test results showed that up to four wavefronts modes can be observed for excitation frequencies between 66 and 130 kHz. They are easily detected where the laser vibrometer is positioned at 0° , 80° and 90° . At 20° , 30° and 70° , three wavefronts are observables. For the rest of the laser vibrometer positions, two wavefronts are detected. These results are shown in Figure 10 - **Figure 19**. These measurements agree with the numerical predictions reported by Hernandez [172].

Figure 10 - **Figure 19** have been labelled based on the knowledge acquired from the literature review and previous experiments, where the phase velocity of the S_0 and A_0 mode are well known. But the SH_{01} and SH_{02} (slower and faster wavefronts of SH_0) have been predicted based on the numerical modelling work carried out by Hernandez.

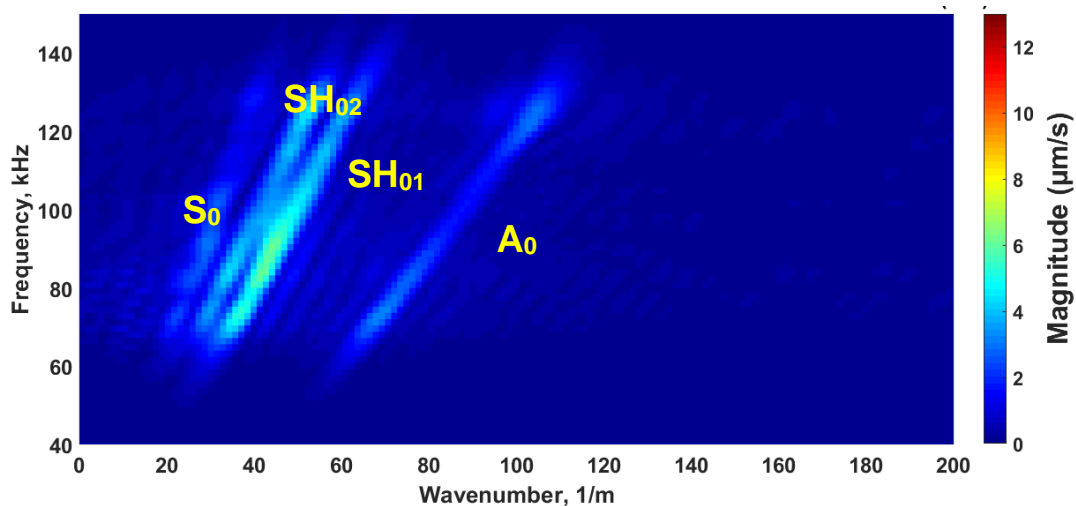


Figure 10 Wavenumber plot at 0° for signal transmission parallel to the fibres (45°)

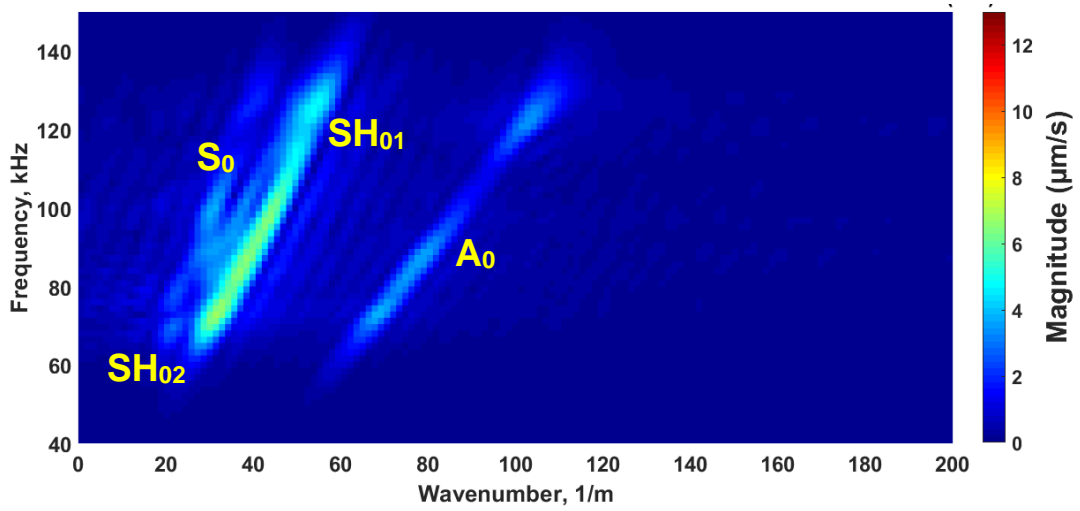


Figure 11 Wavenumber plot at 10° for signal transmission parallel to the fibres (45°)

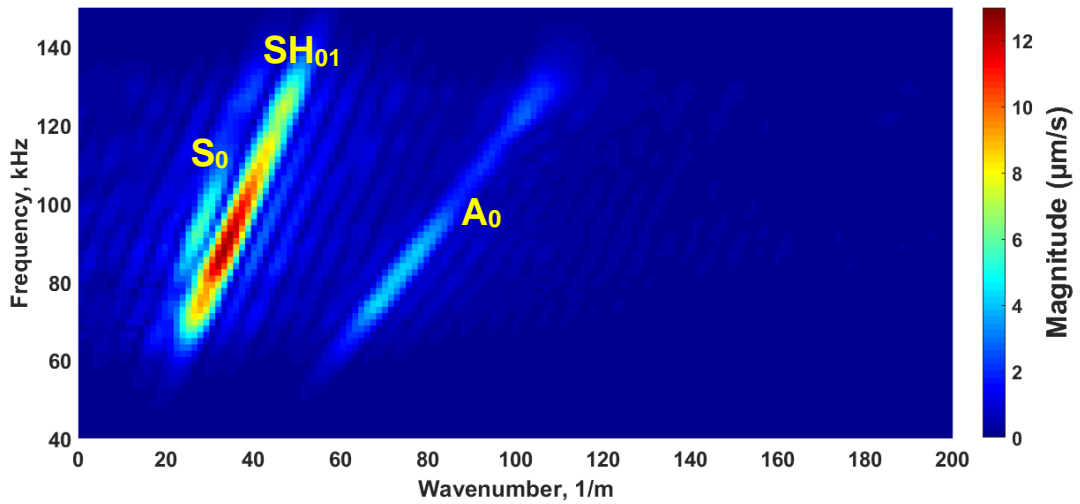


Figure 12 Wavenumber plot at 20° for signal transmission parallel to the fibres (45°)

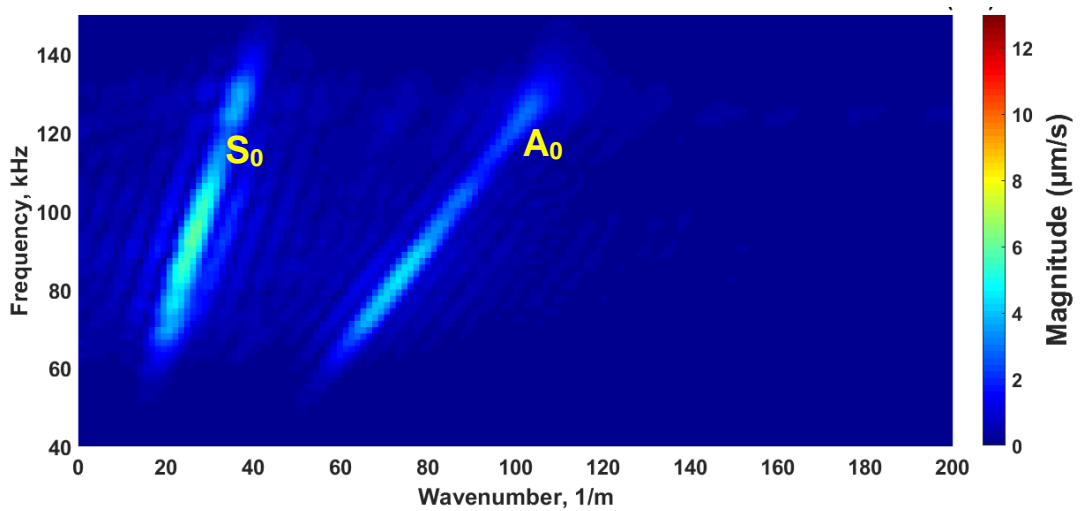


Figure 13 Wavenumber plot at 30° for signal transmission parallel to the fibres (45°)

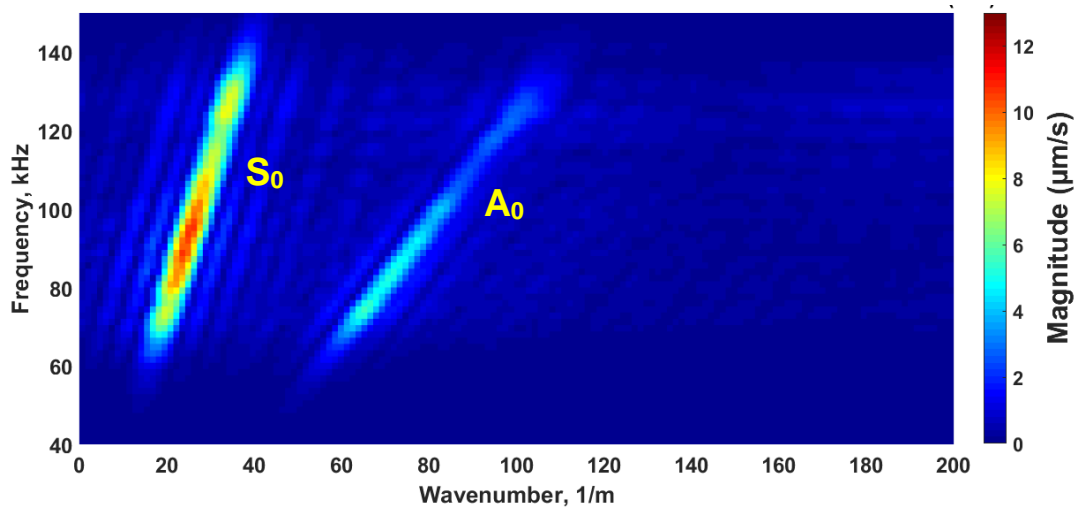


Figure 14 Wavenumber plot at 40° for signal transmission parallel to the fibres (45°)

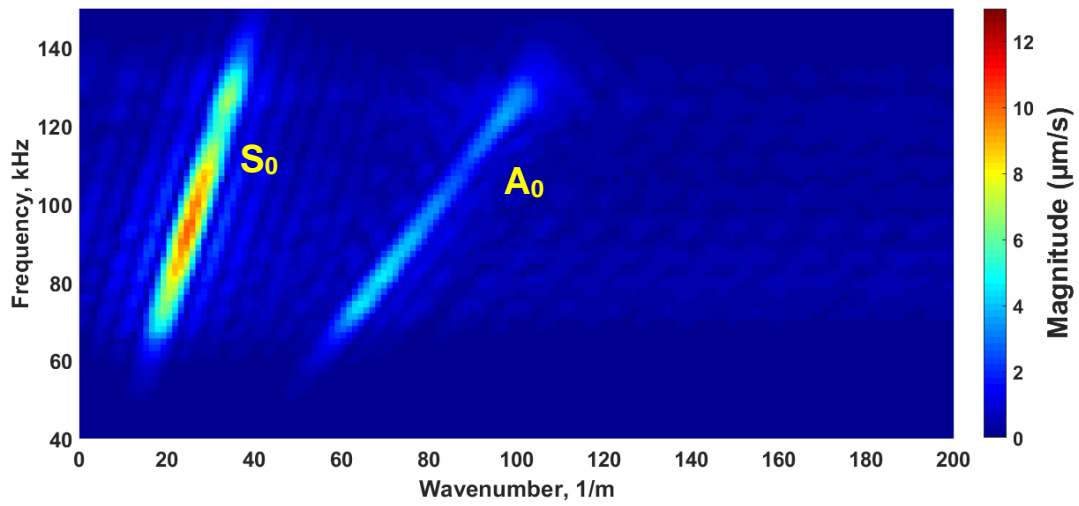


Figure 15 Wavenumber plot at 50° for signal transmission parallel to the fibres (45°)

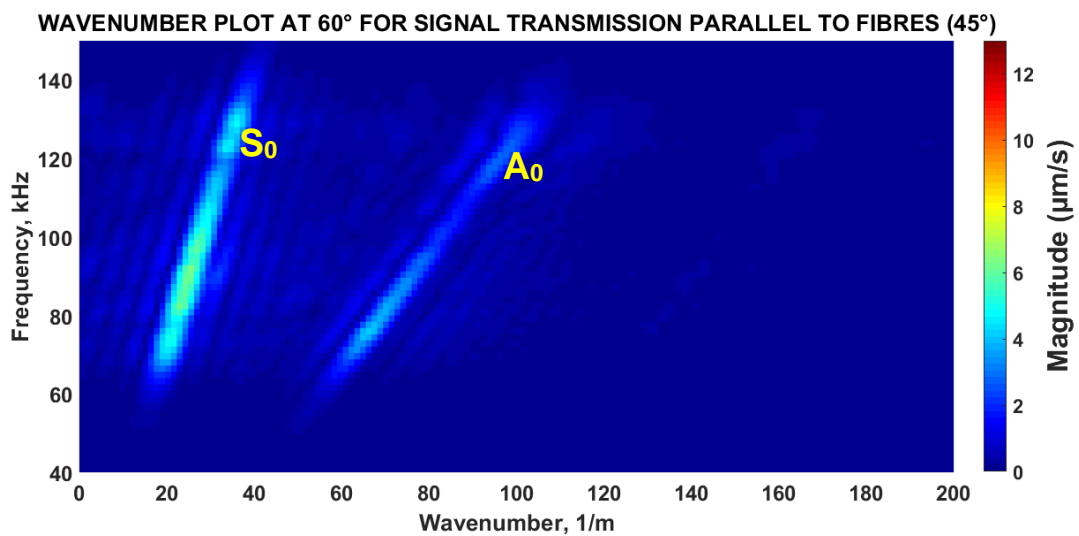


Figure 16 Wavenumber plot at 60° for signal transmission parallel to the fibres (45°)

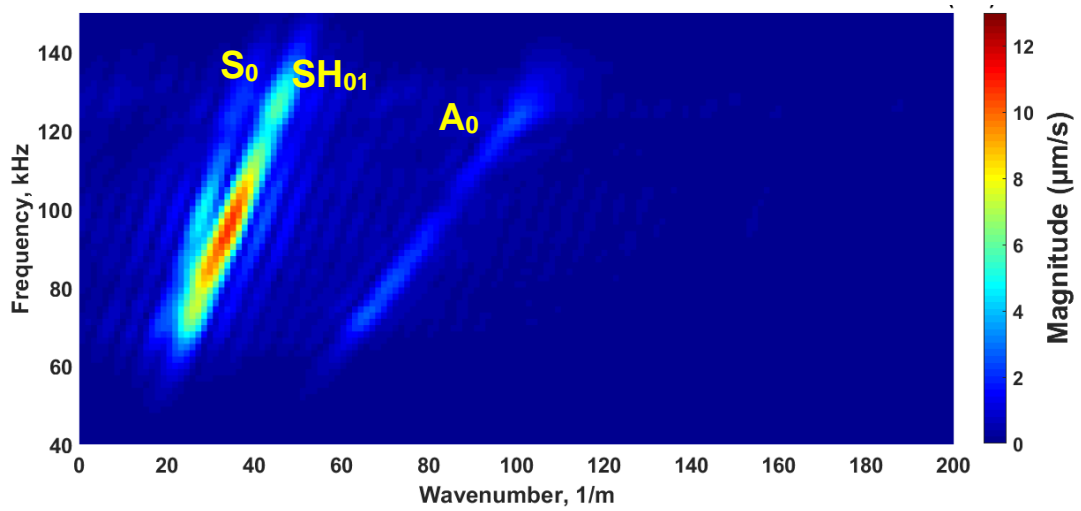


Figure 17 Wavenumber plot at 70° for signal transmission parallel to the fibres (45°)

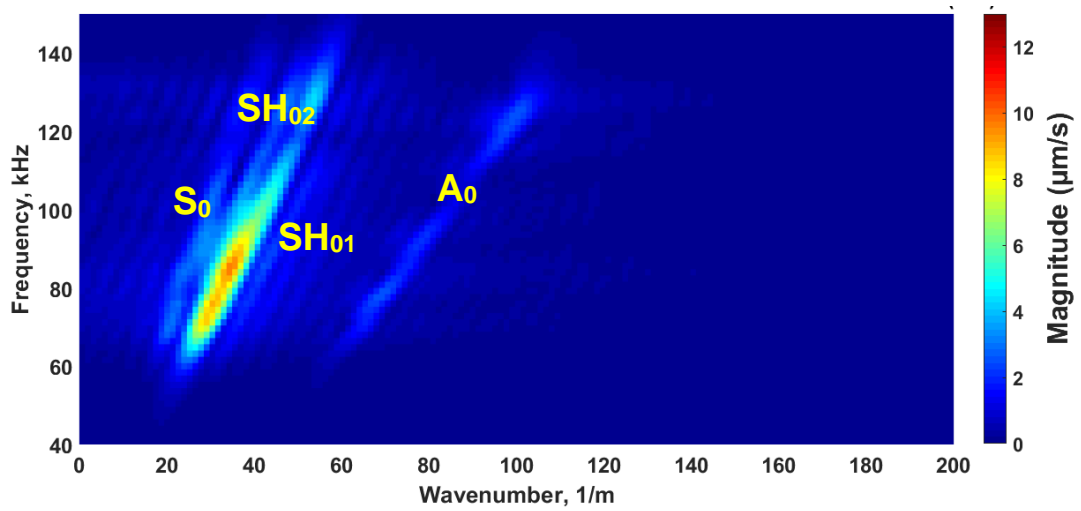


Figure 18 Wavenumber plot at 80° for signal transmission parallel to the fibres (45°)

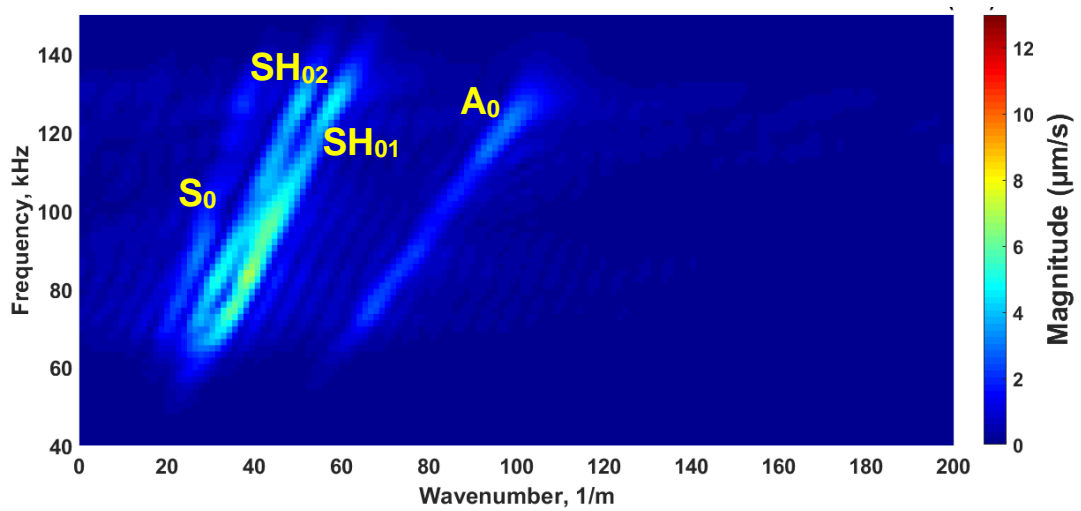


Figure 19 Wavenumber plot at 90° for signal transmission parallel to the fibres (45°)

Dispersion curves for the “ON-FIBRE” signal generation

The phase velocity profiles shown in Figure 20 are for signals transmitted parallel to 45° direction and for the excitation frequency ranging from 66kHz to 130kHz (with increment of 4 kHz).

These velocity profiles are the S_0 , A_0 and SH_0 (SH_{01} and SH_{02}) wave modes. They result from the wavenumber plots from Figure 10 - **Figure 19**.

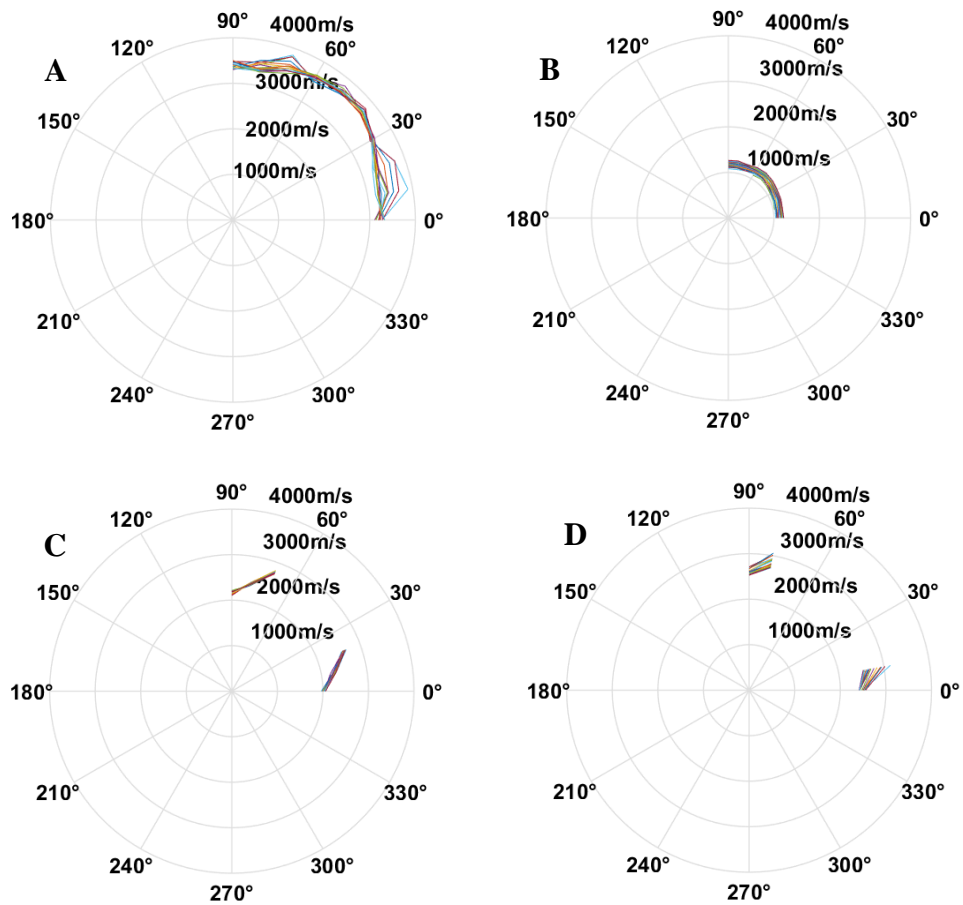


Figure 20 S_0 (A), A_0 (B), SH_{01} (C), SH_{02} (D) phase velocities from signal transmission parallel to fibres (45°)

Wavenumber plots for the “OFF-FIBRE” signal generation

Wavenumbers for the “OFF-FIBRE” signal transmission were also calculated from data collected between 0° and 90° (with an increment of 10°) but for signals generated in line with the X-axis of the plate, as shown in Figure 9.

Data collected between from 0° to 20° show that four wave modes are propagating in this area. From 30° to 90° , three wave modes were recorded. These results are shown in Figure 21 -Figure 30.

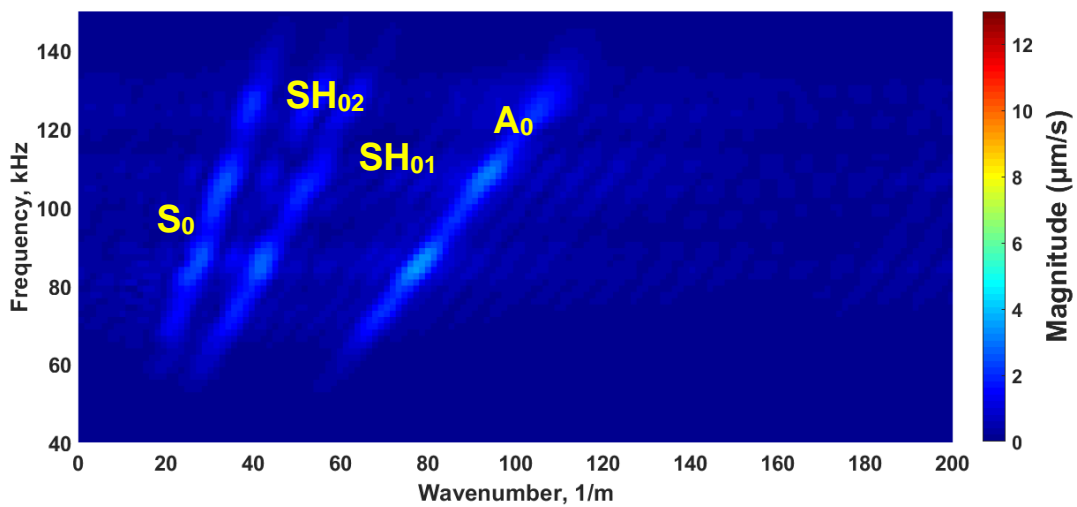


Figure 21 Wavenumber plot at 0° for signal transmission off-fibre (Plate X-axis)

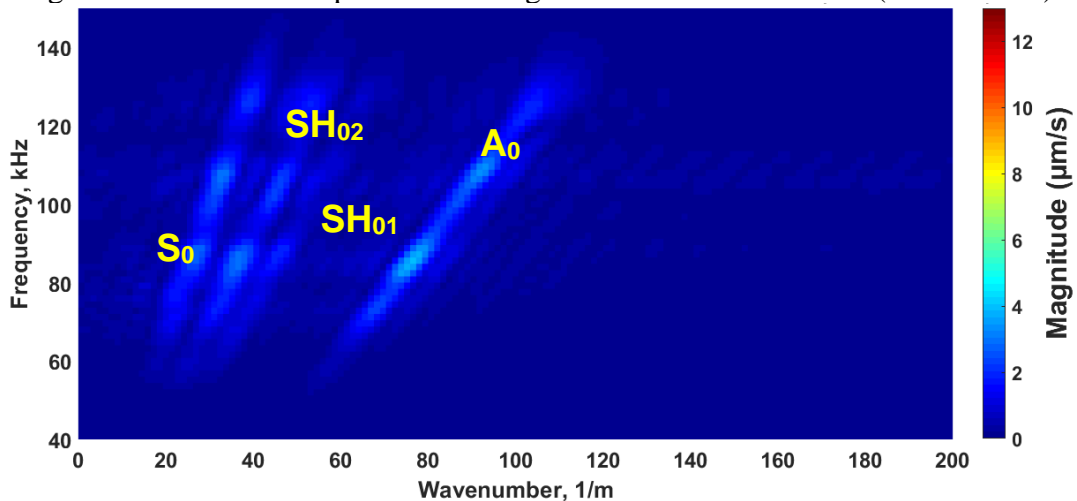


Figure 22 Wavenumber plot at 10° for signal transmission off-fibre (Plate X-axis)

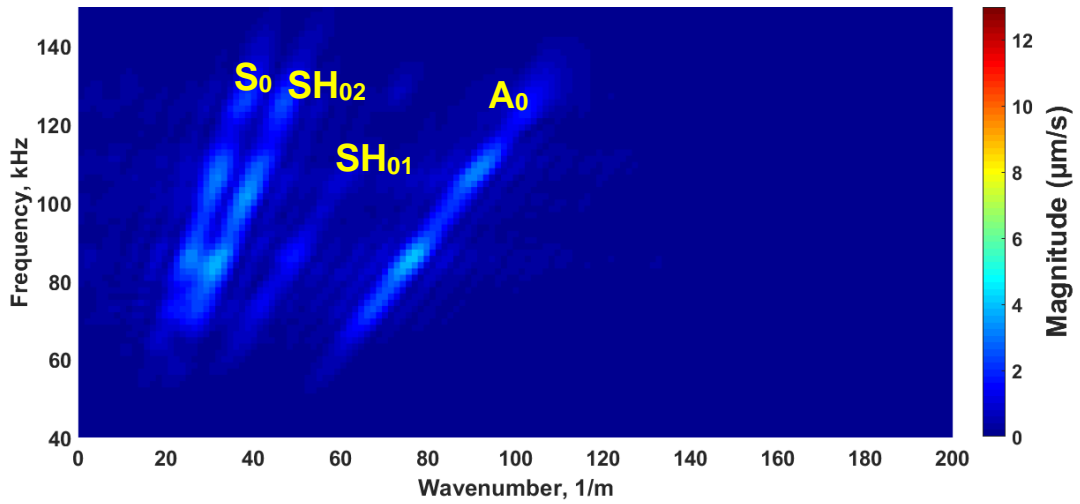


Figure 23 Wavenumber plot at 20° for signal transmission off-fibre (Plate X-axis)

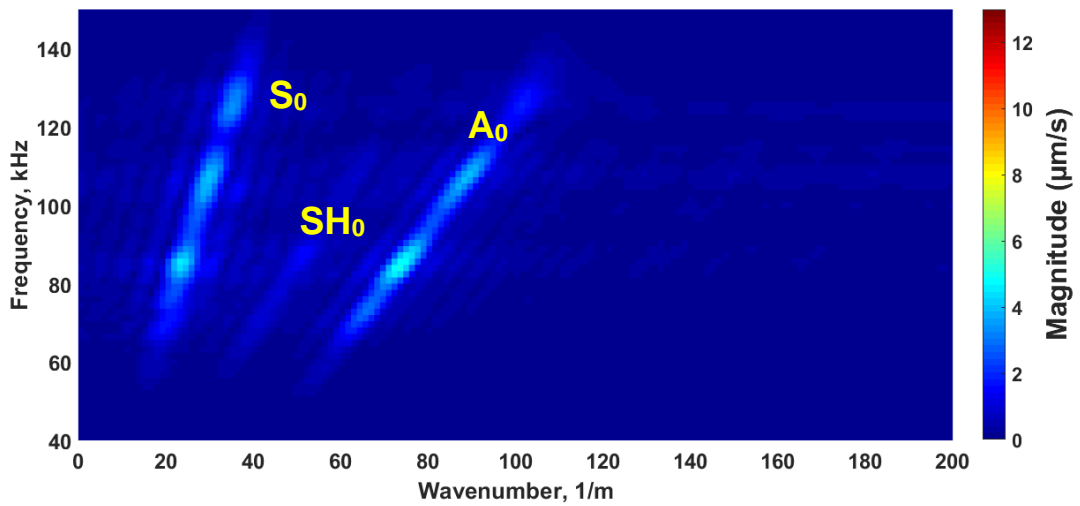


Figure 24 Wavenumber plot at 30° for signal transmission off-fibre (Plate X-axis)

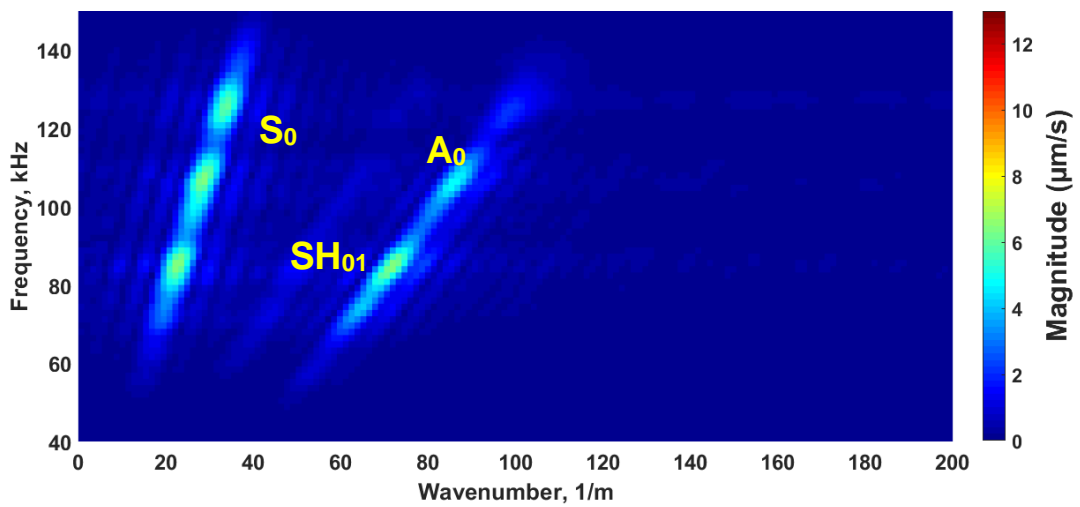


Figure 25 Wavenumber plot at 40° for signal transmission off-fibre (Plate X-axis)

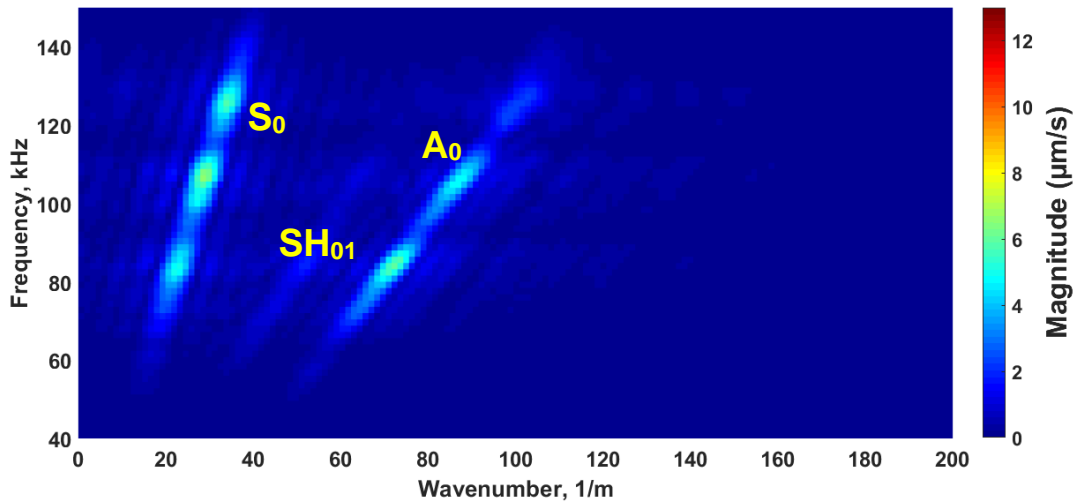


Figure 26 Wavenumber plot at 50° for signal transmission off-fibre (Plate X-axis)

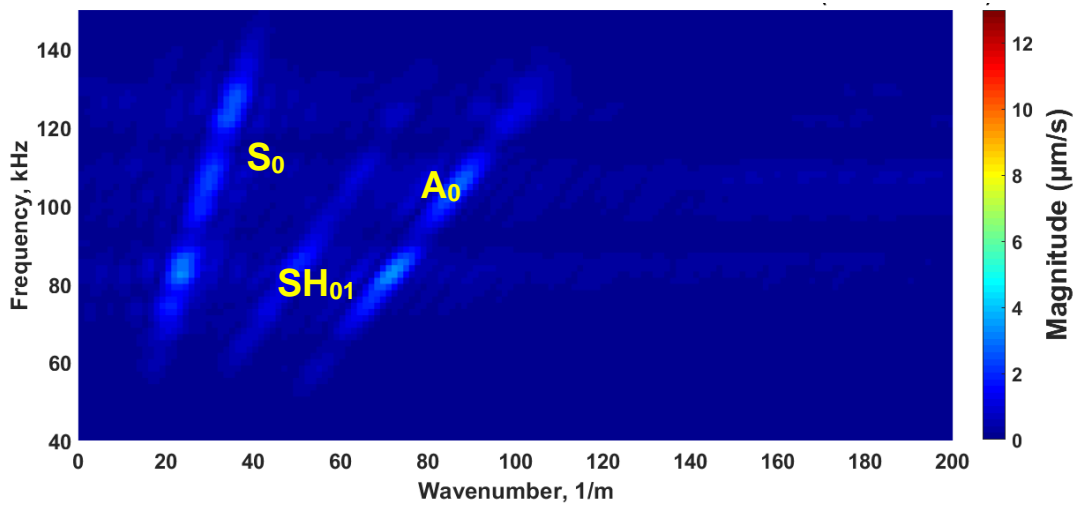


Figure 27 Wavenumber plot at 60° for signal transmission off-fibre (Plate X-axis)

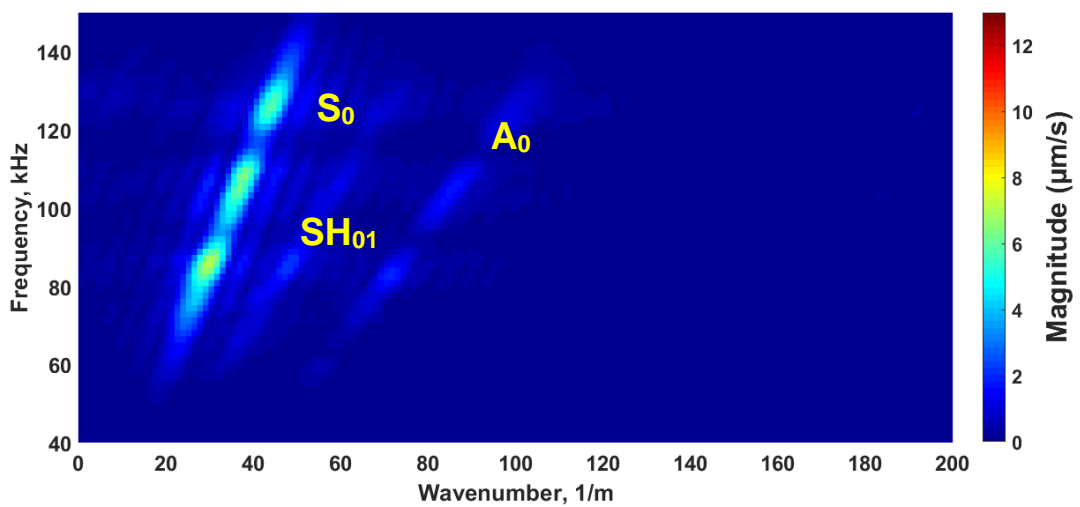


Figure 28 Wavenumber plot at 70° for signal transmission off-fibre (Plate X-axis)

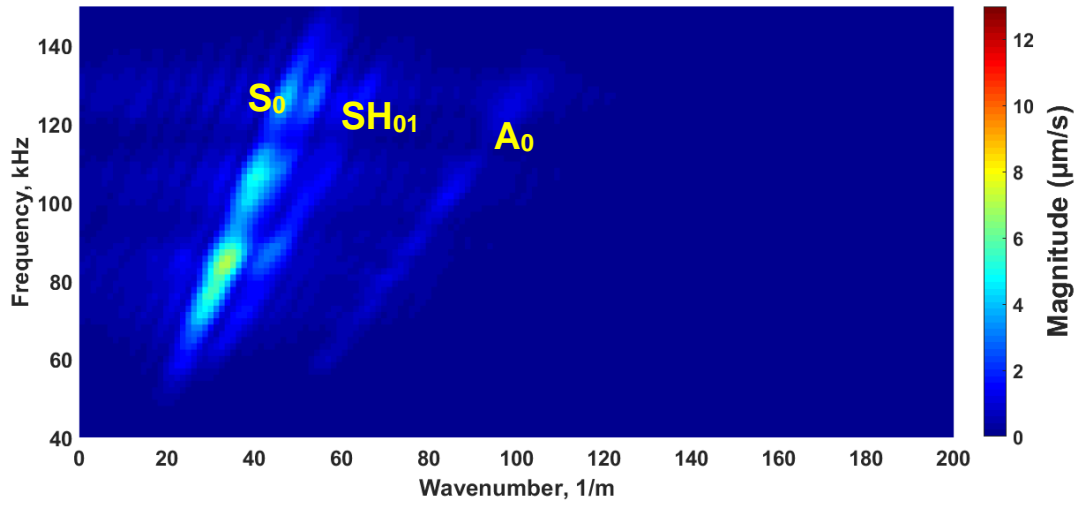


Figure 29 Wavenumber plot at 80° for signal transmission off-fibre (Plate X-axis)

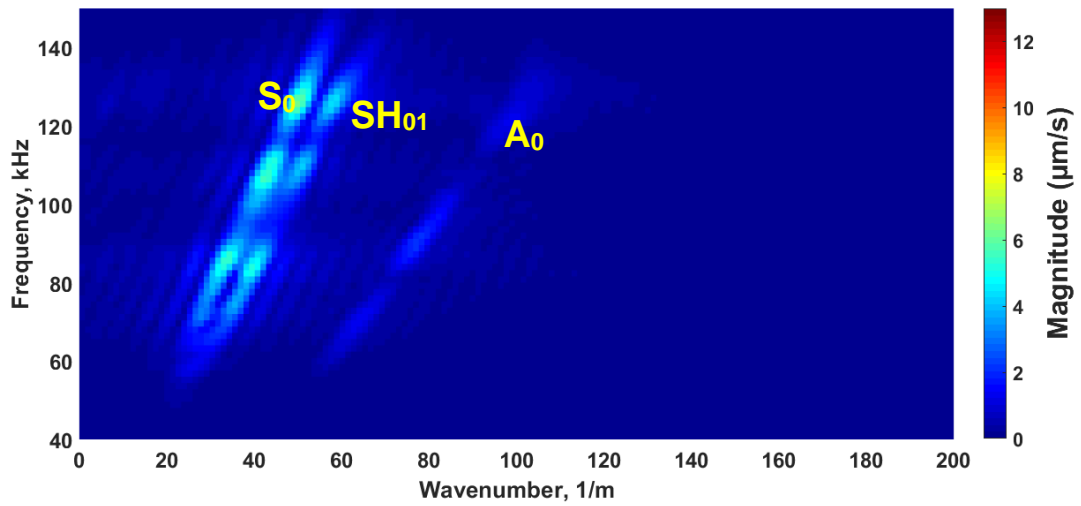


Figure 30 Wavenumber plot at 90° for signal transmission off-fibre (Plate X-axis)

Dispersion curves for the “OFF-FIBRE” signal generation

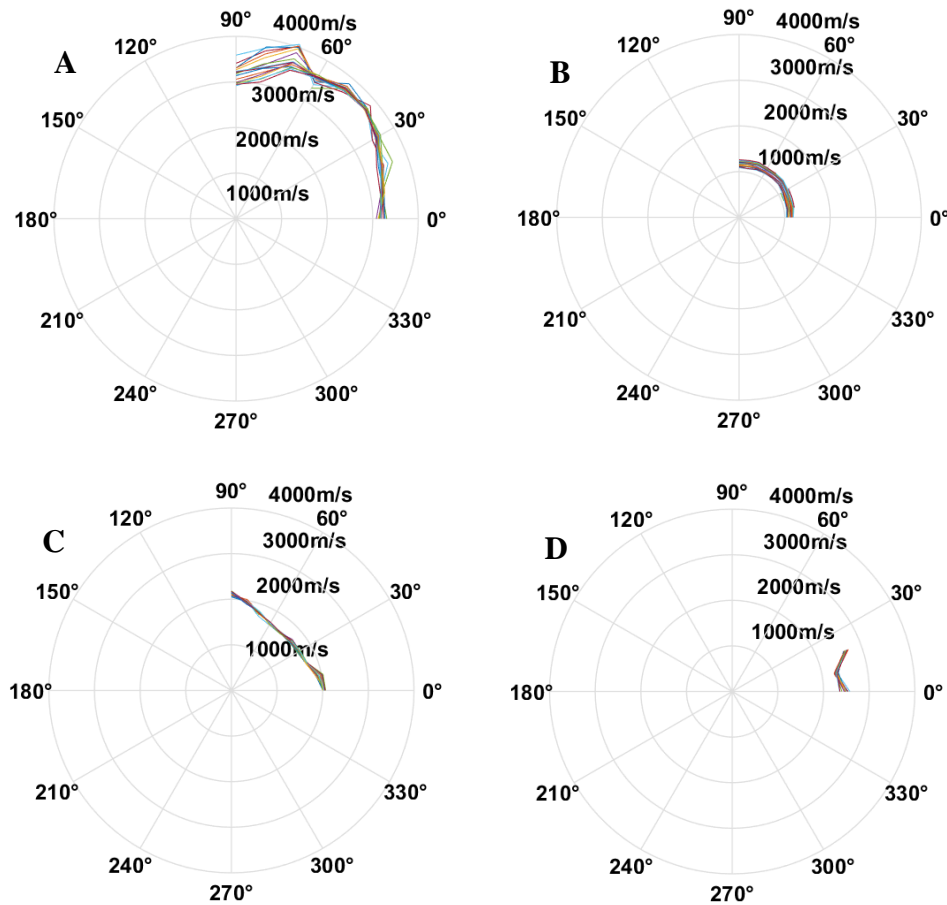


Figure 31 S_0 (A), A_0 (B), SH_{01} (C), SH_{02} (D) phase velocities from signal transmission off fibres (X-Axis)

The phase velocity profiles shown in Figure 31 are for signals transmitted parallel to the plate X-axis (0° direction) and for the excitation frequency also ranging from 66kHz to 130kHz. These velocity profiles are the S_0 , A_0 and SH_0 (SH_{01} and SH_{02}) wave modes resulting from the wavenumber plots from Figure 21 - Figure 30. **Figure 31(A-C)** agree with Hernandez work^[172] while **Figure 31D** only agrees partially, i.e. the SH_{02} mode is only detected between 0° and 30° where it should also be detected between 60° and 90° .

4.4.2 Sensor assessment

Results for the “ON-FIBRE” signal generation

On the top of test results from the wavenumber plots (Figure 10 - **Figure 19**) and velocity profiles (**Figure 20**), Test results showed that the shear horizontal wave modes are not always present at every angle. This would suggest that the shear waves would be limited in terms of area of inspection/structural health monitoring. Therefore, the remainder of this chapter focusses only the behaviour of the fundamental Lamb wave modes.

For all the following figures reported, the blue trace represents the surface vibrating in parallel to the direction at which the ultrasonic waves propagate (Lamb waves); the red represents the surface vibrating tangentially to the direction of propagation (shear horizontal waves) and the green shows the out-of-plane vibration (also Lamb waves).

Thickness-shear PZT elements

Figure 32 shows the surface velocity of the S_0 mode against each angle and in polar axes for the low end of the frequency range (66 kHz) and the top end (130 kHz).

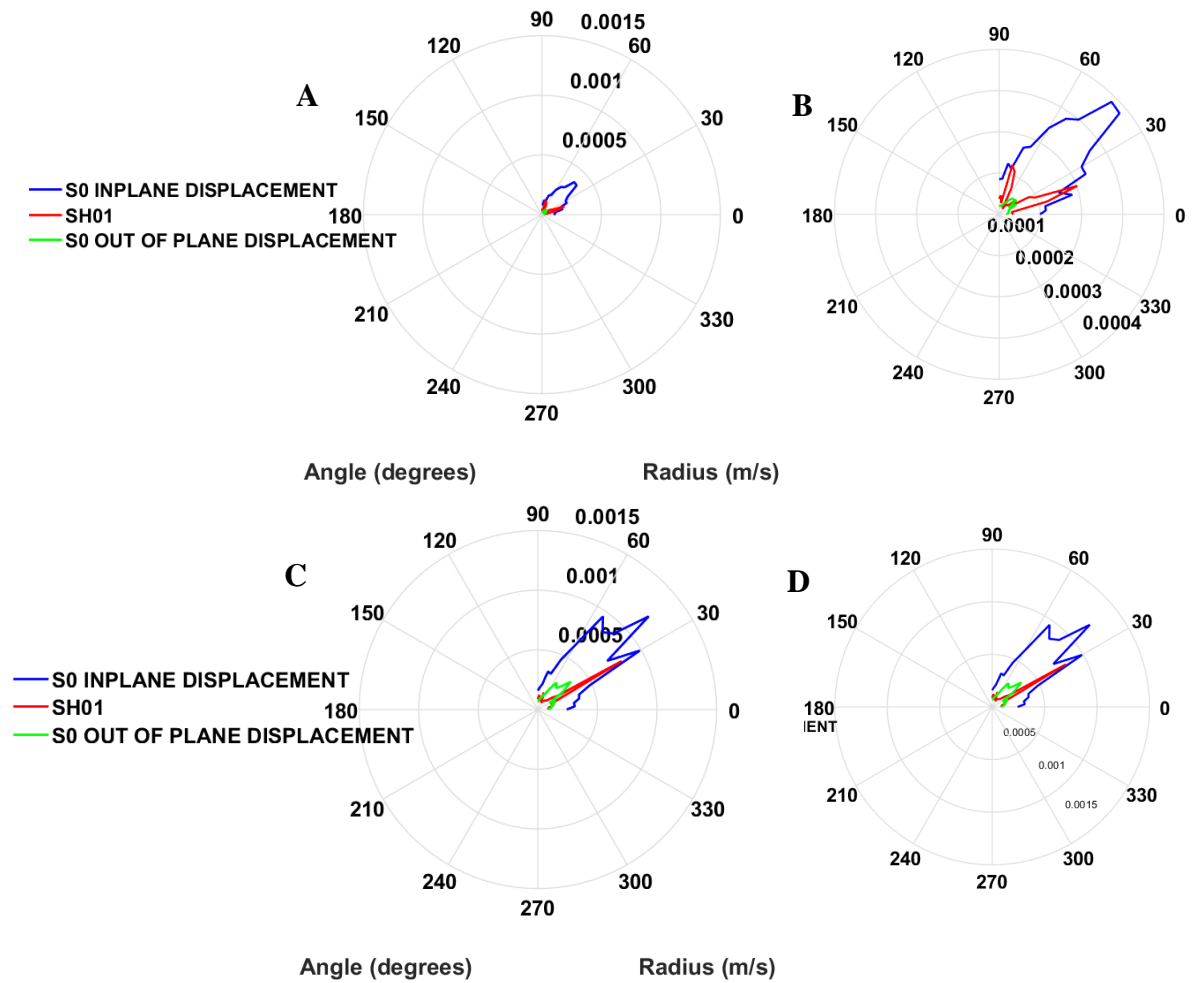


Figure 32 S₀ mode directionality from signal transmission parallel to fibres at 66 kHz (A&B) and 130 kHz (C&D) – PZT element

Figure 32B and D are the enlarged views of Figure 32A and C respectively. Figure 33 shows the surface velocity of the A₀ mode against each angle and in polar axes also for the low end of the frequency range (66 kHz) and the top end (130 kHz).

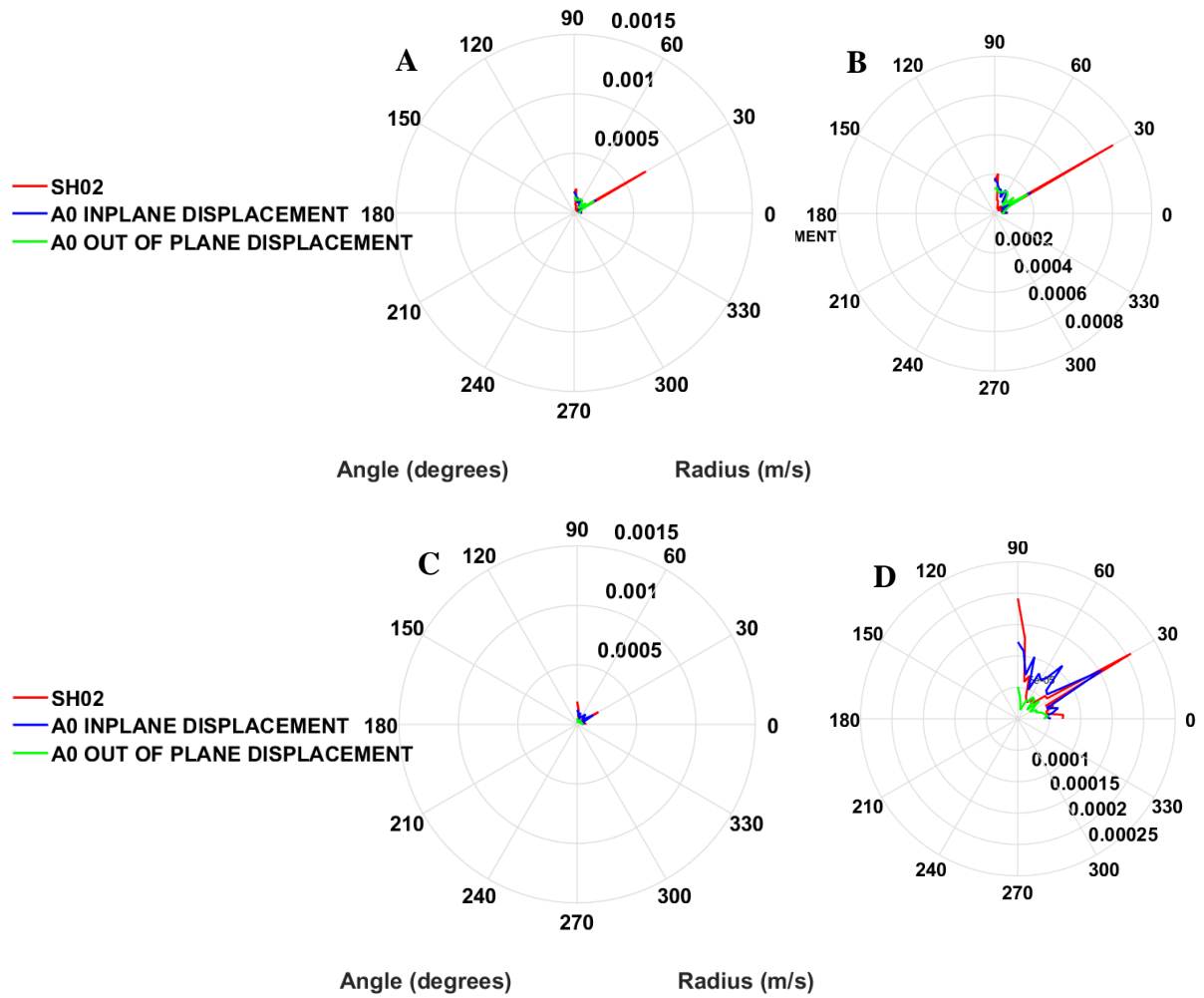


Figure 33 A₀ mode directionality from signal transmission parallel to fibres at 66 kHz (A&B) and 130 kHz (C&D) – PZT element

Figure 33B and D are the enlarged views of Figure 33A and C respectively. The polar plot results for the Teletest transducers (Figure 34 - Figure 35) and the MFCs (Figure 36 - Figure 37) show the same information details.

Thickness-shear PZT elements with backing mass

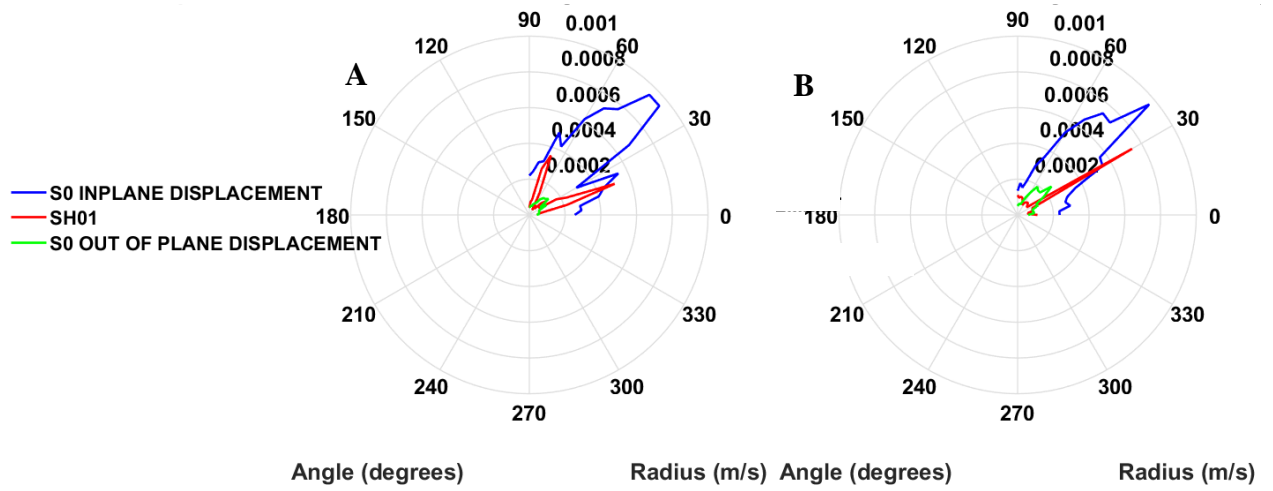


Figure 34 S₀ mode directionality from signal transmission parallel to fibres at 66 kHz (A) and 130 kHz (B) – Teletest Transducer

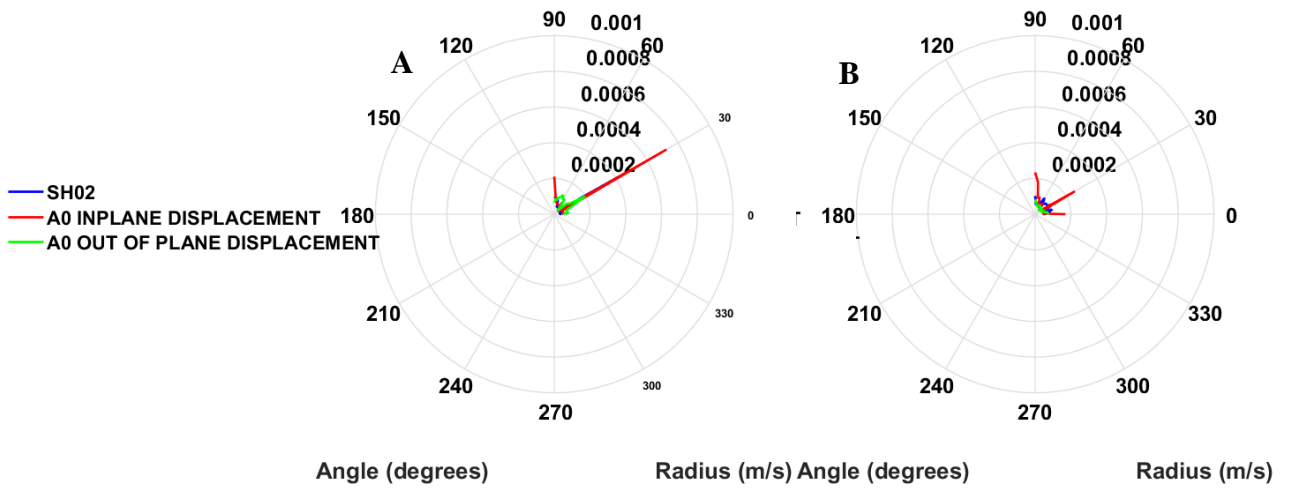


Figure 35 A₀ mode directionality from signal transmission parallel to fibres at 66 kHz (A) and 130 kHz (B) - Teletest Transducer

M2814-P1 MFC sensor

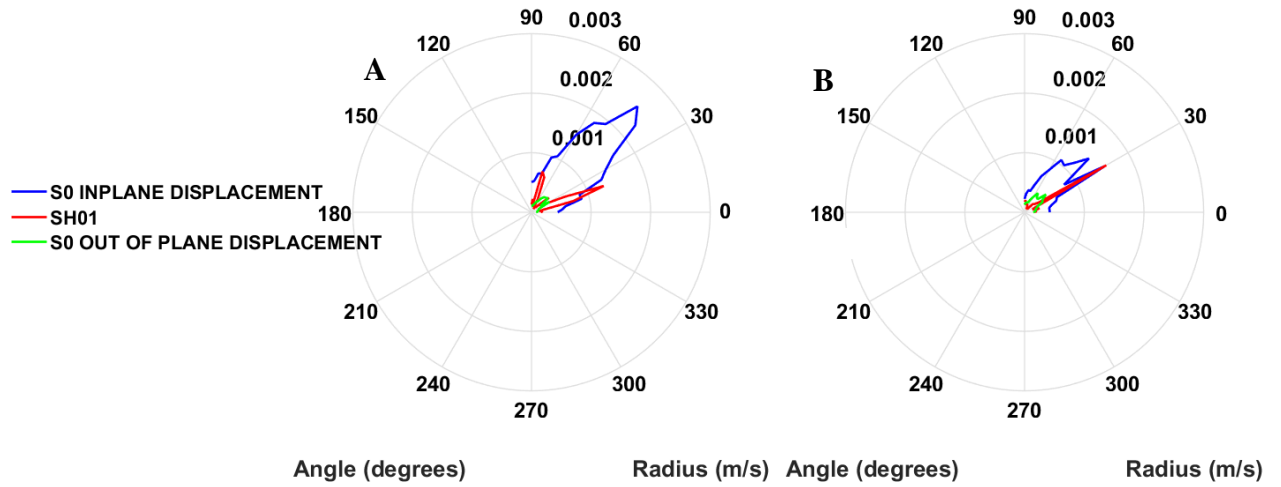


Figure 36 S₀ mode directionality from signal transmission parallel to fibres at 66 kHz (A) and 130 kHz (B) - MFC

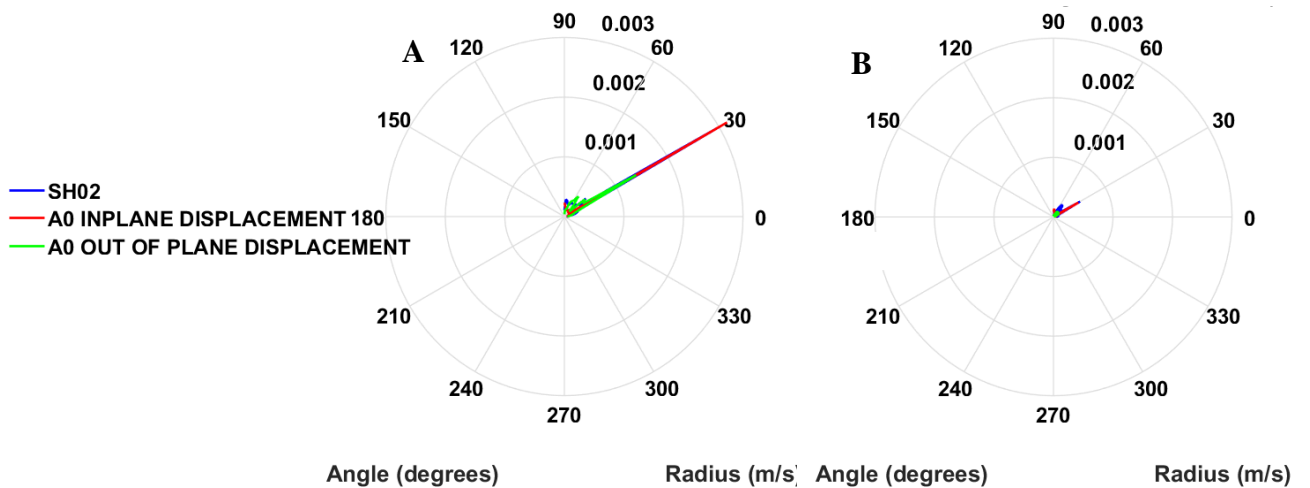


Figure 37 A₀ mode directionality from signal transmission parallel to fibres at 66 kHz (A) and 130 kHz (B) - MFC

Figure 32 - Figure 37 show the directionality of the ultrasonic wave modes in the bi-axial GFRP plate. These plots were obtained by generated signals using sensors aligned in parallel to the direction of the fibres (45°/on-fibre signal generation). From **Figure 32** - Figure 37, it can be observed that the A₀, the faster (SH₀₂) and slower component (SH₀₁) of the SH₀ modes are highly attenuated in comparison with the S₀ mode. Therefore, the A₀ and SH₀ modes will no

longer be investigated and the focus will be on the S_0 mode, which is more likely to detect changes in the material.

4.4.3 Performance comparison between the Thickness-shear PZT element, Thickness-shear PZT element with backing mass and MFCs

As previously reported, the S_0 mode offers a greater amplitude than the A_0 and SH_0 modes, therefore the focus now is on the S_0 mode only. Results below show that the MFC sensors transmit with greater amplitudes than the Thickness-shear PZT element and Thickness-shear PZT element with backing mass.

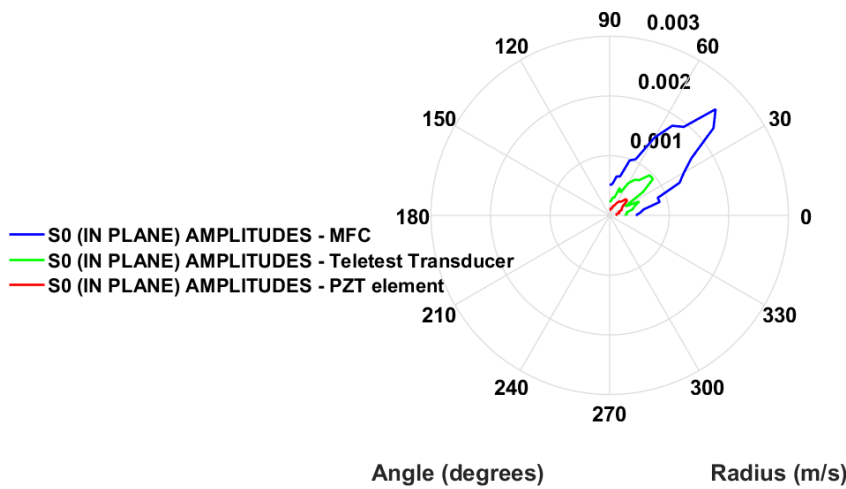


Figure 38 Comparison of the S_0 mode in- plane displacements between transducers – transmission parallel to fibres (66kHz)

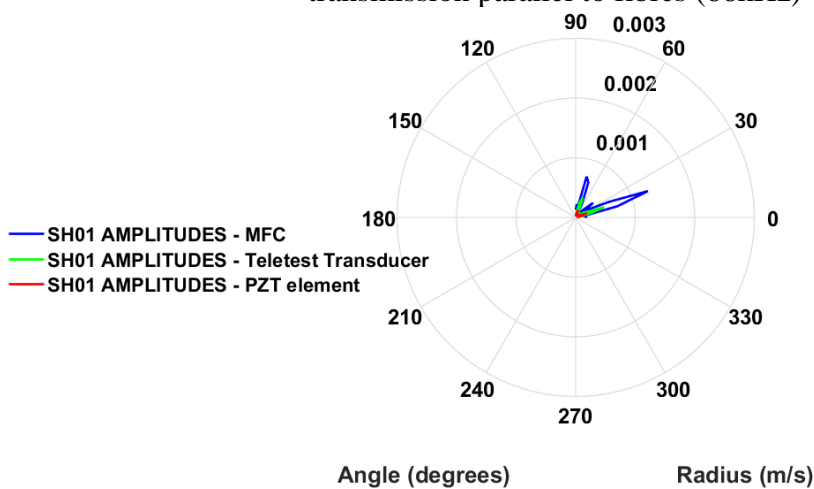


Figure 39 Comparison of the SH_{01} modes between transducers – transmission parallel to fibres (66kHz)

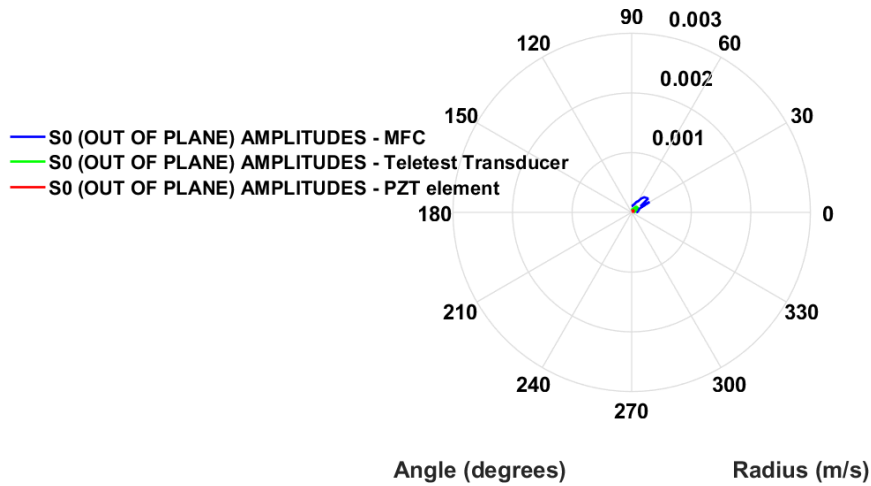


Figure 40 Comparison of the S_0 mode out-plane displacement between transducers– transmission parallel to fibres (66kHz)

Figure 38-Figure 40 show the directionality of the S_0 mode only in the bi-axial GFRP plate. These plots were obtained by generated signals using sensors aligned in parallel to the 45° plate-axis (on fibre signal generation). It can be observed that the shape of the plots is the same regardless of the sensor (Thickness shear PZT element, its commercialised version or an MFC). Therefore, only one transducer type was required in order to compare the directionality of the ultrasonic wave modes between the on-fibre and off-fibre signal generation.

Results for the “OFF-FIBRE” signal generation (Thickness shear PZT element only)

Figure 41 show the performance resulting from the signal excitation at 0° with the PZT element only. The area coverage is not as good as when signals are excited at 45° (on-fibre) but is still overall better than the coverage provided by the A_0 mode.

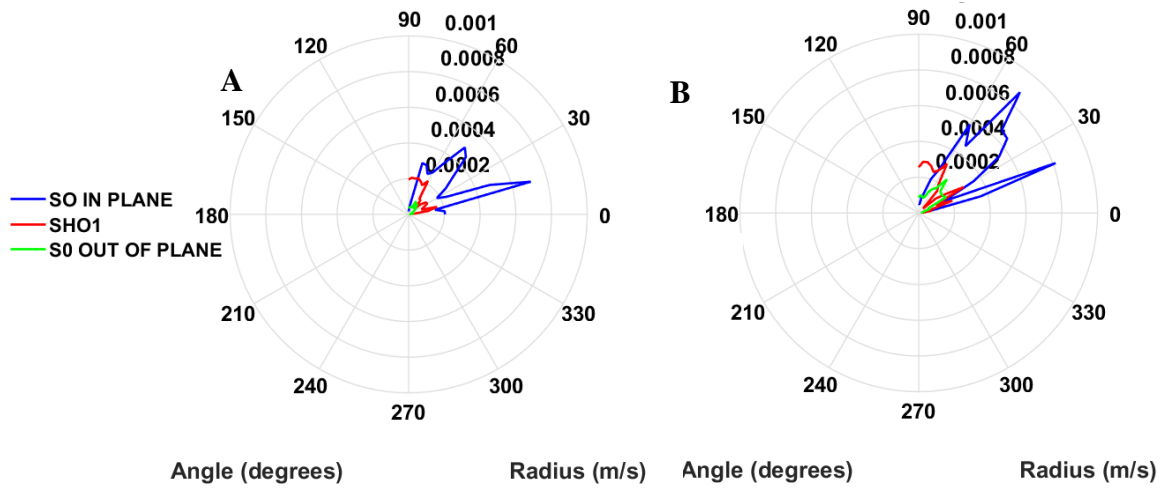


Figure 41 S₀ mode directionality from signal transmission off-fibre at 66 kHz (A) and 130 kHz (B) – PZT element

Comparison between “ON-FIBRE” and “OFF-FIBRE” results for PZT elements

Figure 42 - Figure 44 show differences for the S₀ and Shear wave modes between transmitter aligned parallel to the fibres (45°) and the transmitter orientated toward the off-fibre direction (0° – X-axis).

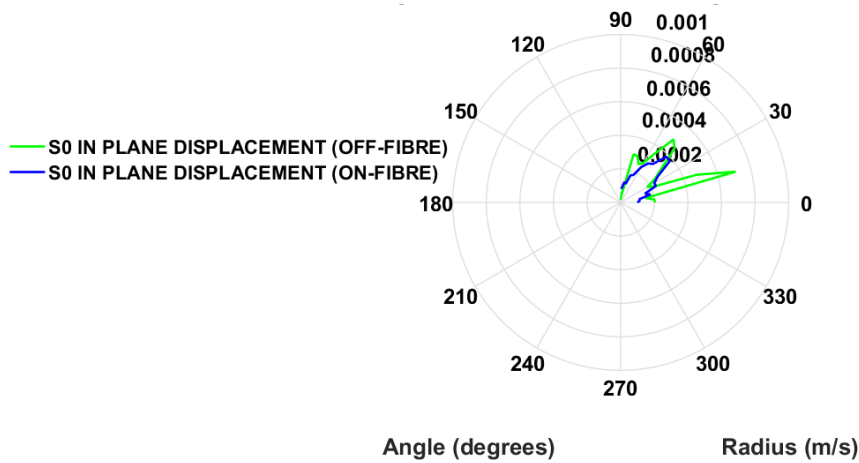


Figure 42 S₀ mode (in-plane)

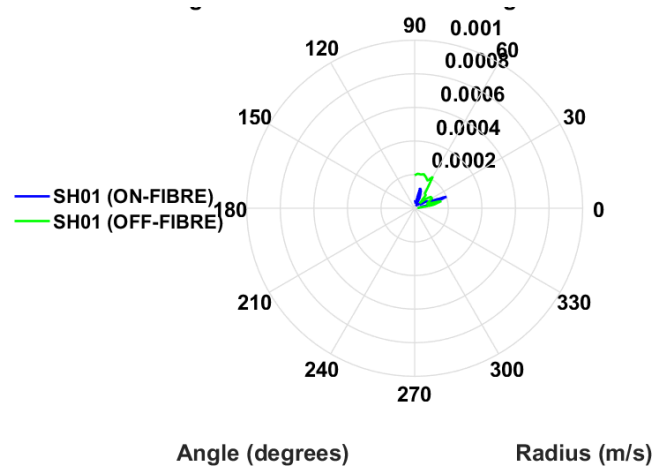


Figure 43 Shear wave SH₀₁

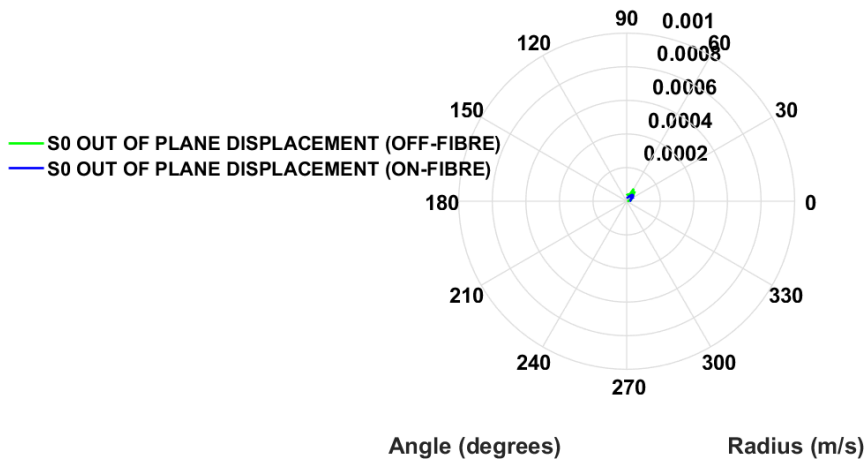


Figure 44 S₀ mode (out of plane)

4.5 General discussion

In order to obtain the directionality plot of ultrasonic wave modes for signal generation in the axis parallel to fibres (45° from plate X-axis) and parallel to the plate X-axis, it was necessary to plot the dispersion curves first. As mentioned in Chapter two, dispersion curves are velocity plots against frequency-thickness product ($f*t$). By determining the wave velocity at a specific excitation frequency, it is possible to design an experiment that will prevent the received ultrasonic waves to overlap. By preventing the overlap, it will be possible to study each wave mode separately and accurately. The dispersion curves of the GFRP plate for signal generation in the axis parallel to fibres (45° from plate X-axis) and parallel to plate X-axis are provided in

Figure 20 and **Figure 31** respectively. The wave velocities in **Figure 20** were obtained from the wavenumber plots in Figure 10-Figure 19; **Figure 31** was obtained from Figure 21-Figure 30.

The wave velocities in **Figure 20** and **Figure 31** were used to design the experiment for the directionality plot, within the frequency range of interest (66 -130 kHz).

Figure 32-Figure 33 illustrated the wave directionality for signal generated, in direction parallel to the fibre alignment, with the thickness shear PZT element; **Figure 34-Figure 35** are results for the same signal generation axis but from signal generated with the Teletest transducer; and Figure 36-Figure 37 are for signal generated with the M2814 MFC sensor. After deducting from Figure 32-Figure 37 that the S_0 mode would be the most suitable ultrasonic wave for the remaining work, Figure 38-Figure 40 were plotted to compare the performance of the sensors, using the S_0 mode as reference. At last, the effect of the axis direction of signal generation on wave directionality were illustrated Figure 42-Figure 44. The work carried out here allowed extraction of important details such as:

Wave mode sensitivity

As previously mentioned, it is preferable to carried out GWT of composites in a frequency range where only the S_0 , A_0 and SH_0 exist. This is to enable the easiest data interpretation possible. The dispersion curves presented here were in agreement with Hernandez work^[172]; As predicted by Hernandez^[172], the experimental results showed that the S_0 , A_0 and SH_0 existed in the excitation frequency range 66-130 kHz for the bi-axial GFRP plate. Researchers such as Ramadas^[147], Moreno^[148], Chiu^[149], and Wang^[150] and Rheinfurth^[156] have claimed that the A_0 mode could be used to detect flaws such as delamination and cracks but this cannot be achieved with the guided wave sensors used here. From Figure 32 - Figure 37, it was observed that the S_0 mode was less attenuated than the A_0 , the faster (SH_{02}) and slower (SH_{01}) component

of the SH_0 modes; therefore the S_0 mode will offer a better signal to noise ratio in measurements. But there is a downside in using the S_0 mode over the other wave modes. As a rule of thumb, the resolution limit in UT is half wavelength. Both A_0 and SH_0 are slower than the S_0 mode. For a given frequency, the A_0 and SH_0 modes will have a wavelength smaller than the S_0 mode, meaning there are more likely to detect small defects.

Wave mode directionality and area coverage

The dispersion curve results enabled the design of the experiments leading to plotting directionality of the ultrasonic wave modes in the bi-axial GFRP. Figure 42 demonstrated that as long as the axis of vibration of the sensors is parallel to the orientation of the fibres, less scatter of the S_0 mode would be observed. But the area of coverage for S_0 is still quite limited. Figure 42 showed that when the axis of vibration of the sensors is parallel to 45° , the peak signal amplitude is also at 45° . This is because the mechanical properties of a material will be stronger in directions parallel to fibres than in off-fibre directions. The wave amplitude/velocity/acceleration depends on the mechanical properties of the material. The higher the mechanical properties, the higher the wave amplitude/velocity/acceleration. But Figure 42 further shows that when received signals are recorded away from the fibres (especially at 0° and 90° of the plate axis), the signal amplitudes drop down to 25% of the signal amplitude recorded at 45° . Another interesting factor to take into account is the poling of the sensors. From a physical point of view, three different sensors were tested here. But from the sensor poling angle, two types were tested: the d_{51} (thickness shear PZT element and Thickness shear PZT element commercially manufactured) and the d_{33} (M2814 MFC). Figure 38 - Figure 40 show that the difference in sensor poling has had no effect in the wave directionality profile.

Transducer performance

Figure 38 - Figure 40 show that the M2814 MFC transducer demonstrated better performance on the GFRP woven plate than the Thickness shear PZT element and the Teletest transducers. The same experimental set-up, signal excitation characteristics, equipment and coupling method were used to test these three transducers. Therefore, the results in Figure 38 - Figure 40 demonstrate that the MFC vibrate more easily than the Thickness shear PZT element and the Teletest transducers, when coupled to the GFRP laminate and excited within the frequency range used here (66-130 kHz).

4.6 Conclusion

The literature on GWT of polymer matrix composites has evidence that the fundamental Lamb modes would be suitable for detecting composite defects such as delamination. The work discussed in the literature have mostly been carried out in a laboratory, using equipment more suitable for laboratory environment than industrial purposes. The sensors used here are designed for industrial use and test results show that the ultrasonic mode worth investigating was the S_0 mode, which in term of sensitivity has outweighed the A_0 mode. Also, defects located away from the orientation of the fibres might become difficult to detect, as they will be in an area where the S_0 wave amplitude will experience a decreasing signal to noise ratio. In terms of choosing the adequate transducer for inspection or structural health monitoring, the MFC sensors were more effective, than the thickness shear PZT element and the Teletest, transducer at transmitting Lamb modes at the frequency range of interest. Its good performance was attributed to its ability to vibrate more freely than the other two transducers. MFCs are more likely to be used as part of a monitoring or inspection solution for GFRP woven materials than thickness shear PZT element and transducers.

**Chapter 5: GUIDED WAVE TESTING OF A
GFRP CROSS-PLY LAMINATE
CONTAINING A DELAMINATION**

5.1 Introduction

The main objective of this chapter is to study the performance of MFC sensor during the inspection of a biaxial GFRP plate with a delamination inserted at manufacturing stage. The MFC sensors are usually permanently mounted to testing material but in this particular case, they were coupled to the material by using pressure. This was achieved by applying a set of weight (4kg) on top of the MFC sensor. This was needed in order to move the MFC sensors freely on the material surface. As mentioned in the literature review, it was reported that when the S_0 mode encounter a delamination, mode conversion would result and the A_0 mode would be generated. While materials like Teflon, PTFE, peel-ply or release agents have been reportedly used to mimic a delamination, the effect of a 25 mm x 15 mm piece of paper on the fundamental Lamb waves is experimentally investigated in this chapter.

5.2 Experimental protocol

5.2.1 Specimen manufacture

Two identical GFRP plates (1300x1000x7.4mm) were manufactured with the autoclave method and contained 32 plies ($[0/90]_{16}$) each. The first sample (with no known defects) was used for calculating the dispersion curve on the on- and off-fibre directions. This sample ID was Chapter5_Specimen 001. The second sample (Chapter5_Specimen 002) was used to study the interaction of Lamb waves with the piece of paper (25 x 15 mm) that had been inserted during lay-up of the GFRP plate.

5.2.2 UltraLAB system for plotting dispersion curves of a Cross-Ply GFRP plate

Although there are software and analytical models available for calculating dispersion curves, here the dispersion curves were calculated using data directly retrieved from the type of laminate under investigation. The dispersion curves were calculated based on data collected

with a low frequency ultrasonic measurement system called ULTRALAB (owned by Kaunas University). The Ultralab system was made of adjustable transducer holders attached to an automatic stepper mounted to a single axis scanner, as shown in **Figure 45** .

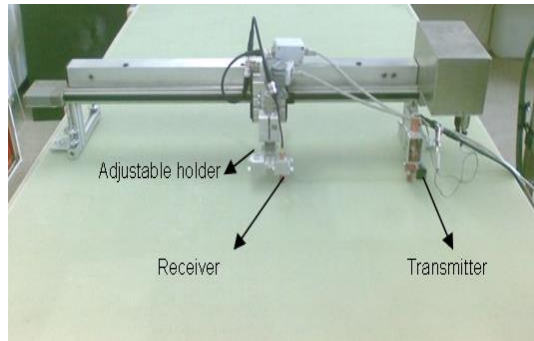


Figure 45 ULTRALAB equipment

The PZT transducers were coupled to the structure with glycerol. Several test trials were conducted to identify the resonance frequency (f_r) of the PZT when coupled to the GFRP plate, prior to the start of the experiments. The resonance frequency of the PZT transducers was found to be 100 kHz. The different tests conducted to identify f_r were not recorded for this particular experiment but Figure 46 - Figure 48 illustrated how to find f_r for a specific material:

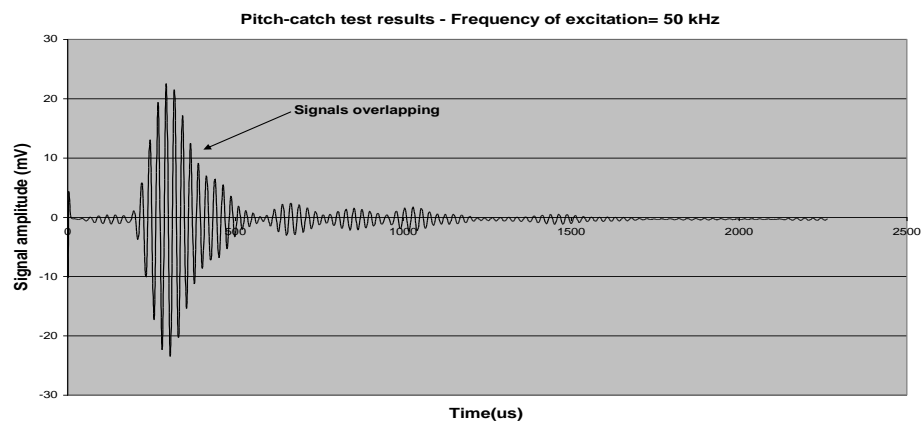


Figure 46 A-scan with centre frequency of 40 kHz

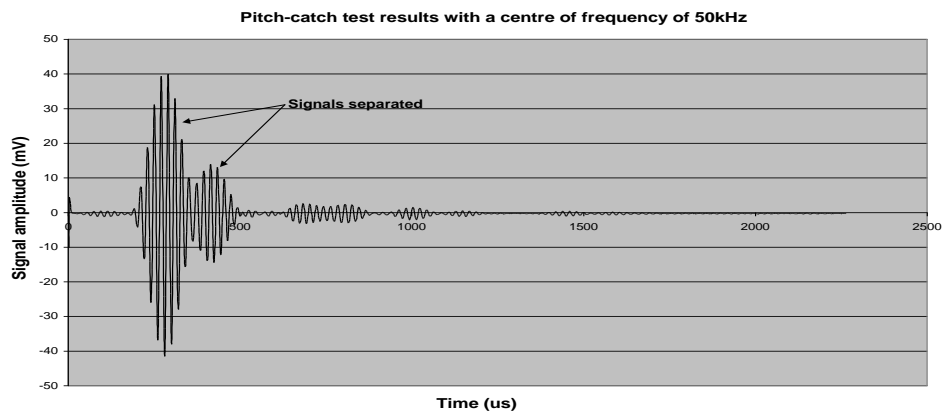


Figure 47 A-scan with centre frequency of 50 kHz

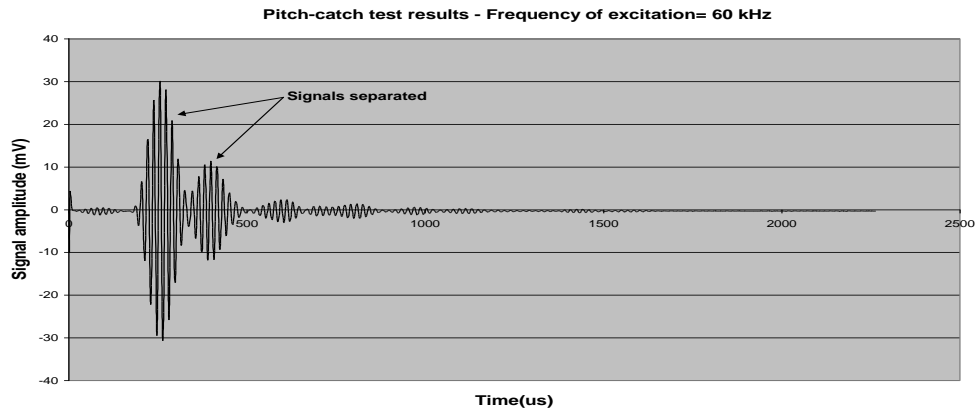


Figure 48 A-scan with centre frequency of 60 kHz

Figure 46 - Figure 48 were the outcomes of a pitch-catch test which was performed on a quasi-isotropic ($0^{\circ}/45^{\circ}/90^{\circ}$) GFRP plate using 6 MFC as transmitter and one as receiver. Figure 46 showed that the first two signals had overlapped and the peak-to-peak signal amplitude of the first echo was just above 40 mV; Figure 47 showed a better resolution of the signals and the peak-to-peak signal amplitude was approximately 80 mV; and finally Figure 48 showed that, although the echoes are still separated, the peak-to-peak amplitude of the first echo dropped down to 60 mV. The different results showed that the f_r was between 40 and 50 kHz. Further sweep frequency tests were carried out from 40 to 50 kHz with a step of 1 kHz. The final results

showed that the resonance frequency of the M2814-P1 type when coupled to the GFRP quasi-isotropic plate was 48 kHz.

Going back to the experimental design used to calculate dispersion curves, the test frequency selected for the Ultralab equipment was 100 kHz. In order to calculate the dispersion curves, the transmitter was placed at a fixed location on the surface of inspection. The first position of the receiver was 250 mm from the transmitter. The distance between the two sensors was decreased by step of 1 mm, covering a total distance of 200 mm; thus, the final position of the receiver was 50 mm from the transmitter. Data were collected at each position and were processed using a MATLAB script file, specifically prepared for processing data produced by the Ultralab system.

5.2.3 Velocity profile of fundamental Lamb waves in Chapter5_Specimen001

The rectangular GFRP plate initially used to calculate the dispersion curves was cut into a circular shape, to enable further experiments to be conducted, not only to determine the velocity of the S_0 mode, but also to observe the overall variation of the S_0 velocity in the GFRP plate. The MK2 unit and two MFCs were used to perform this experiment and the excitation frequency was 56 kHz for a five-cycle signal. The transmitter was mounted at the centre of plate (as shown in Figure 49) and the receiver was placed right at the edge. Both transmitter and receiver were rotated in step of 5° in order to perform 72 pitch-catch tests. A set of weights (4 kg in total) was placed above each MFC. The Teletest® software produces two types of files: The ASCII and TTD formats; MATLAB was used to processed data from the ASCII files. The script consisted of analysing only the S_0 and A_0 mode by recording their peak to peak amplitude around the plate. Due to a good signal to noise ratio, the extracted data did not require filtering.

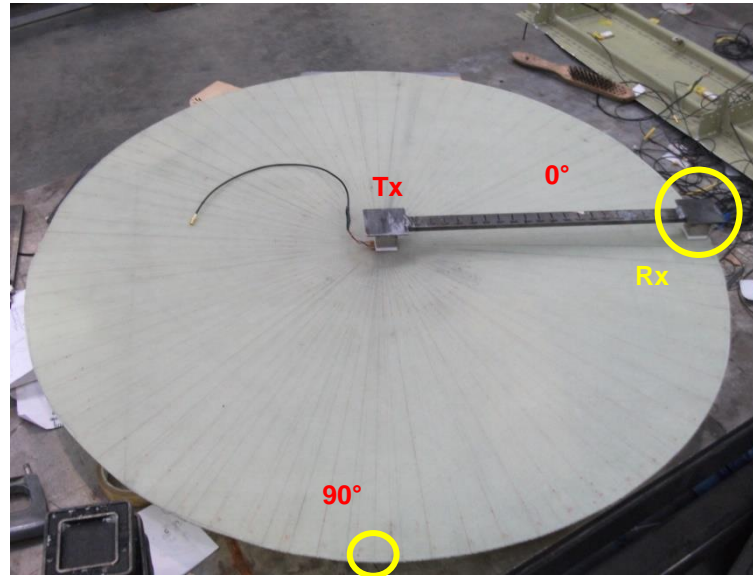


Figure 49 Experimental setup for directional MFC frequency response

5.2.4 MFC frequency response

Further tests were carried out to investigate the frequency response of the MFCs when coupled to Chapter5_Specimen001. The test configuration illustrated in Figure 49 was repeated and the pitch-catch tests were conducted with a sweep frequency from 20 to 200 kHz with an increment of 1 kHz. The limits set for the time arrival of both S_0 and A_0 modes in the previous MATLAB script needed adjustment to monitor a complete signal envelope throughout the sweep frequency.

5.2.5 Guided Wave Testing for delamination detection (single excitation frequency)

The coupling method for MFCs was assessed during preliminary inspection of the second GFRP plate (Chapter5_Specimen002) which contained a 25x15mm piece of paper. The MK2 Teletest Focus unit was used and the MFCs were coupled using set of weights (4 kg overall) using two separate supports unlike the “bridged” support shown in Figure 49. No couplant was required between the MFC and the surface of inspection. Five-cycle signal pulse, with an excitation frequency of 56 kHz, was used to scan the plate in directions parallel to the fibres,

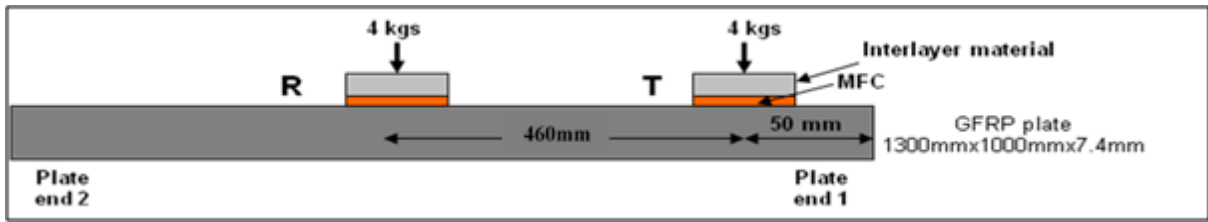


Figure 51 MFC coupling method

Further tests were carried out to verify these results. Chapter5_Specimen002 was tested using the pitch-catch technique by moving the sensors from West to the East side of the plate. Two MFCs were used, each coupled to the plate using the same weight previously mentioned. For this test, the receiver was kept at a set same distance (675mm) from the transmitter while the two-sensor array moved from West to East (Figure 52).

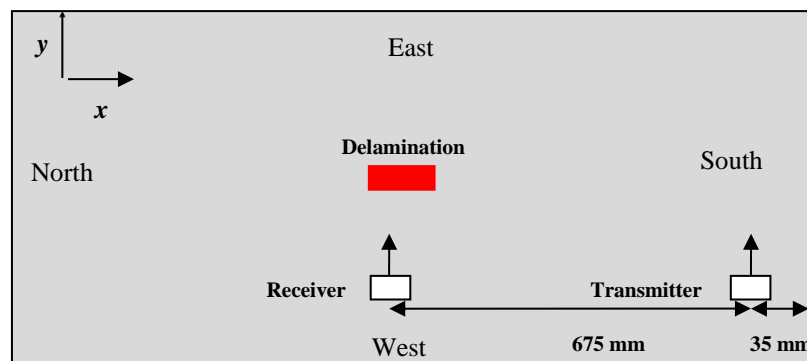


Figure 52 Experimental setup for the West-East scan

The measurements were taken at multiple positions. Data were collected at 40, 50, 60, 70, 80, 90, 100, 120, 150, 220, 250, 300 and 350 mm at either side of the paper insert, from the plate West to East direction.

5.2.6 Guided Wave Testing for delamination detection (sweep frequency)

The detection of the paper insert, by using the experimental setup described in **Figure 50**, was taken further by carrying out a sweep frequency test. Chapter5_Specimen002 was once again scanned using two new MFCs which were now controlled by a MK4 unit. Each point of the selected area around the paper insert was scanned using with a sweep frequency signal from 40

to 80 kHz with an increment of 1 kHz. Five-cycle signal pulse was used to inspect the plate in the directions where it is known that the phase velocity of the S_0 mode is approximately 3000 m.s^{-1} and the A_0 mode's is 1000 m.s^{-1} . At 80 kHz, the pulse length of S_0 and A_0 will be 187.5mm and 62.5mm respectively. At 40 kHz, the pulse length of S_0 and A_0 will be 375mm and 125mm respectively. In order to keep the S_0 mode, the A_0 mode and reflections from the edges separated during the entire sweep frequency experiment, the first receiving point was set at approximately 380mm from the transmitter which in turn, was located at approximately 190mm from the edge of the plate to the centre of the transmitter. Another 50 locations were examined with a constant increment of the receiving positions fixed at 5 mm. As previously mentioned, it was estimated that the piece of paper was located between the test locations P21 and P26. In this case, data was collected from both surfaces of the GFRP plate: From *Surface A* view, the piece of paper was located at one third of the laminate thickness (estimated between the 10th and 11th ply); from *Surface B* view, it was estimated between the 20th and 21st ply. The MFCs were coupled to the plate using again set of weights (4 kg). This experiment was only conducted once.

5.2.7 Validation technique: Scanning Laser Vibrometry for delamination detection

A closer look was taken at the propagation of Lamb waves in the known damaged area by replacing the receiver (here the MFC) with non-contact receiver, the PSV-400 Vibrometer. This system has been developed by Polytec ^[173] which has more than 15 years of expertise in vibration analysis using a laser. The technology has been developed around the Doppler Effect principle, meaning the system is meant to capture the change in frequency of the particle movements controlled by the MFC exciting the plate. Polytec reported ^[173] that the frequency and velocity of particle displacements can be monitored up to 24 MHz and 20 m.s^{-1} . The Laser Vibrometer PSV-400, equipped to measure the speed and displacement of a particle in three dimensions, was used as indicated in Figure 53.

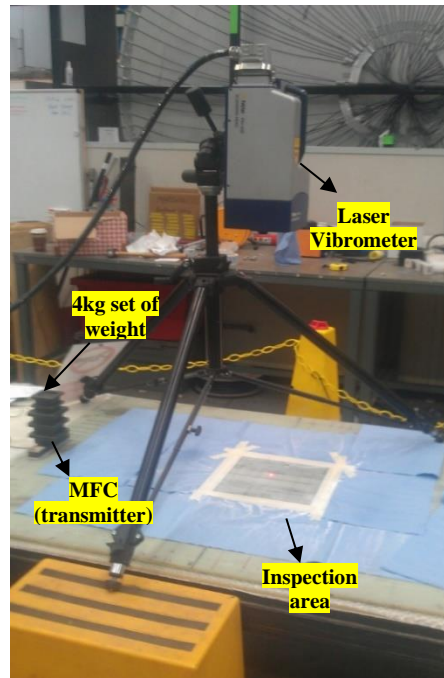


Figure 53: Experimental set-up with PSV-400 Laser Vibrometer

5.3 Results and discussion

5.3.1 UltraLAB system for plotting dispersion curves of a Cross-Ply GFRP plate

The dispersion curves were plotted based on contour plots (graphical representations of wavenumbers). An example of contour plots can be found in Figure 54. The tests were repeated three times by lifting the receiver off the surface between readings. The tests were conducted along the 0° (on fibre) and 45° (off fibre) directions, hence the three different colour traces in the dispersion curves. The colour blue represented the first test, the red the second test and green the third one. Figure 55 showed the dispersion curves matching the contour plot illustrated in Figure 54. Both Figure 56 and Figure 57 showed the comparison between the dispersion curves calculated for the on-fibre and off-fibre directions.

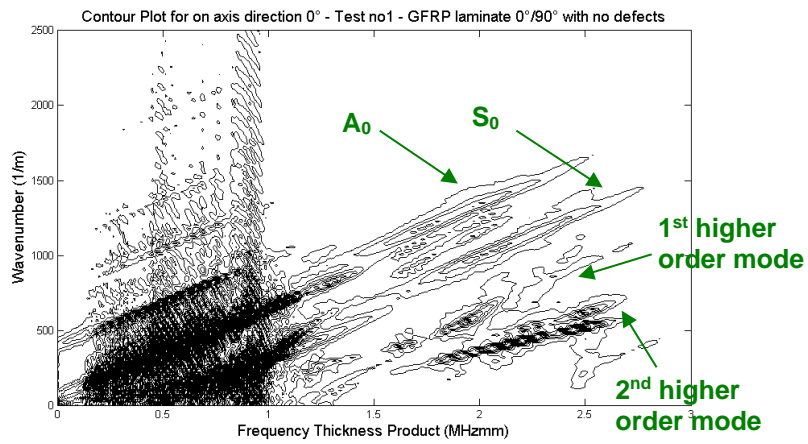


Figure 54 Contour plot for off axis direction 45° - GFRP laminate 0°/90° with no defects

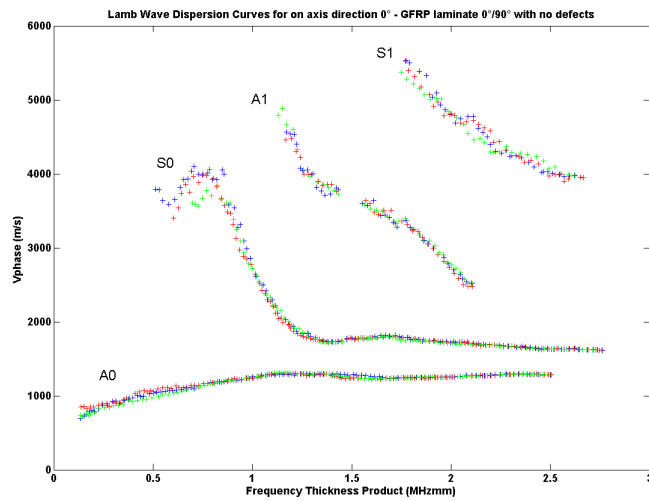


Figure 55 Dispersion curves for on axis direction 0° - GFRP laminate 0°/90° with no defects

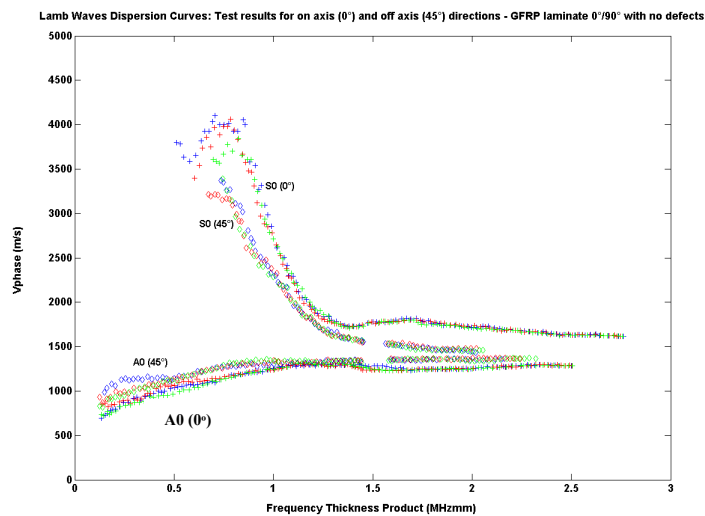


Figure 56 Comparison between on-fibre and off-fibre propagation of the S_0 and A_0 modes

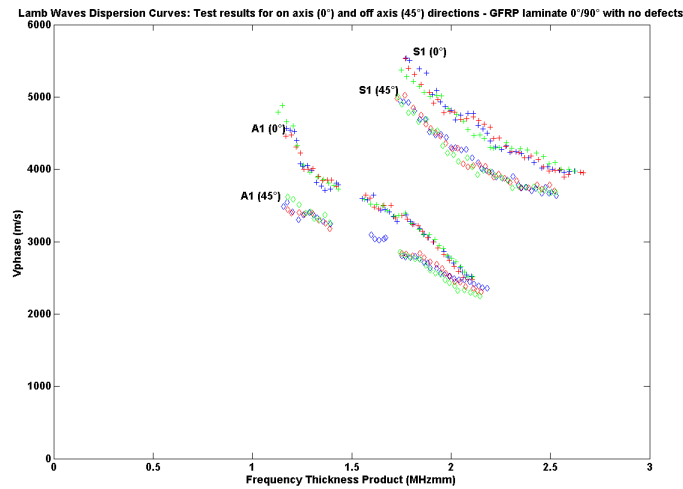


Figure 57 Comparison between on-fibre and off-fibre propagation of the A_1 and S_1 modes

Figure 56 showed that for the S_0 mode, the phase velocity was affected by fibre directionality while the propagation of the A_0 mode was clearly insensitive to the different fibre orientation (also as reported in the literature ^[51]). The reduction of speed of the S_0 mode, propagating at 45° (off fibre) from the fibre alignment, was estimated approximately at 20%. Also, it can be observed that some test data were missing for the dispersion curves at 45° and around 1.5MHz at which, the wavelengths of the ultrasonic waves tend to be closer to the thickness of the plate. Data were also missing for the S_0 mode below 0.5MHz, which is the operating frequency range of interest in which, the S_0 mode is usually non-dispersive. This key information was needed to prepare further test procedures; therefore, additional experiments were conducted to determine with as much precision as possible, the velocity of the S_0 mode in the cross-ply GFRP laminate under investigation. The following results enabled finding this missing piece of information.

5.3.2 Velocity profile of fundamental Lamb waves in Chapter5_Specimen001

Test results in Figure 58 demonstrated that the velocity of the S_0 mode was at his maximum – 3000m/s - at 0° , 90° , 180° and 270° (directions parallel to the fibres) but was reduced in between angles (also as reported in the literature ^[51]). The velocity of the S_0 mode was reduced down to

66% when it travels in the off-fibre directions of this GFRP laminate. It can further be observed that the A_0 mode remained approximately the same (1000m/s) around the plate (also as reported in the literature [51]).

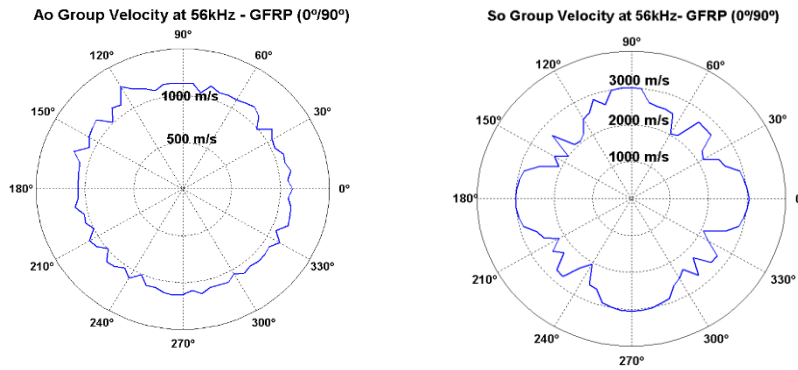


Figure 58 The S_0 and A_0 modes velocities in the defect free GFRP laminate

5.3.3 MFC frequency response

The results showed in Figure 59 demonstrated that, the operating frequency for future experiments on plates similar to Chapter5_Specimen001 should be between 40 and 80 kHz approximately, whether tests are carried out on- or off-fibre. These tests were carried out three times for repeatability purposes. The rest of the results are listed in Appendix B - **MFC frequency response for $[0/90]_{16}$ GFRP circular plates.**

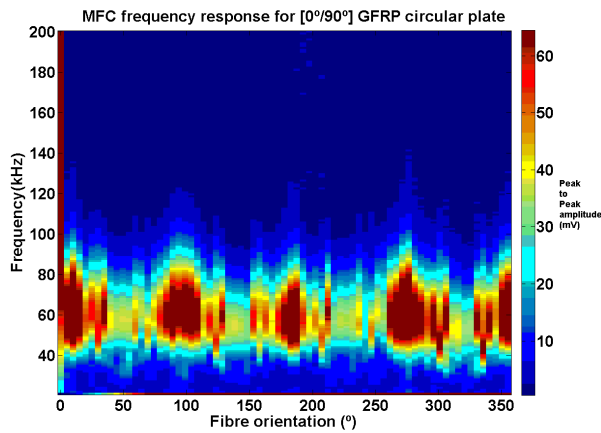


Figure 59 MFC frequency response for $[0/90]_{16}$ GFRP circular plates

5.3.4 Guided Wave Testing for delamination detection (single excitation frequency)

Each line of scanning was repeated three times hence the three different traces in the preliminary test results (Figure 60). It can be observed that overall, the test results are repeatable.

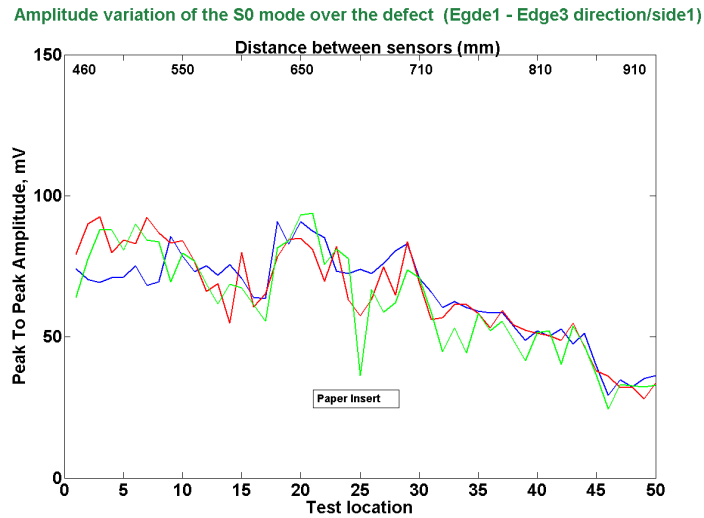


Figure 60 Peak to peak amplitude variation of the S_0 mode along 0 mm axis

The data collected at 40mm, 50mm and 60mm, either side of the paper insert are reported in Figure 61 - Figure 63.

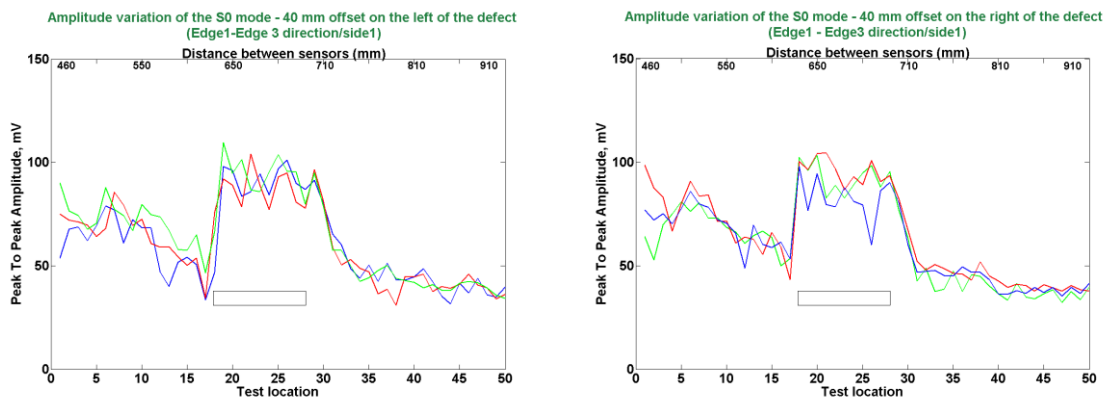


Figure 61 Peak to peak amplitude variation of the S_0 mode at 40mm offset on the left and right side of the paper insert

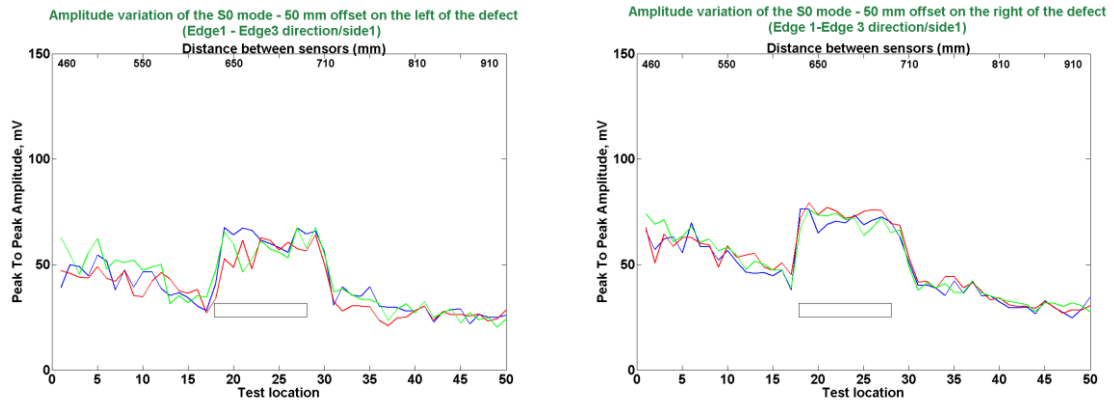


Figure 62 Peak to peak amplitude variation of the S_0 mode at 50mm offset on the left and right side of the paper insert

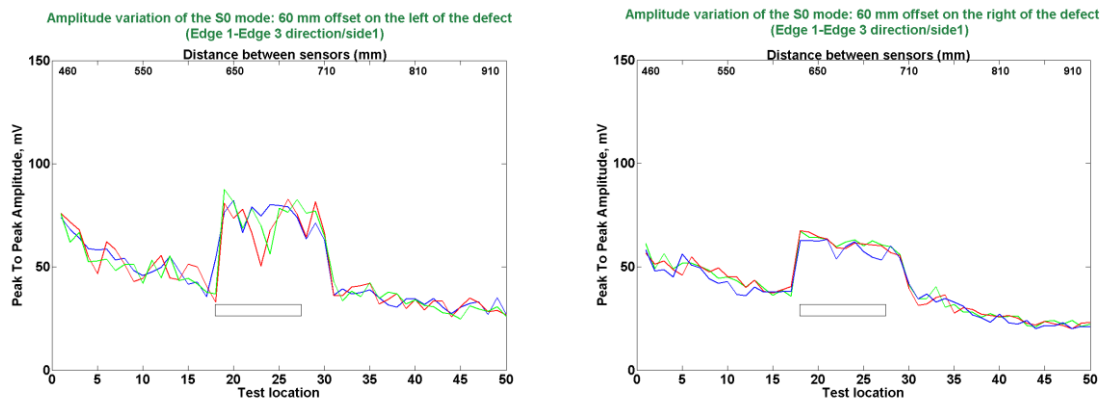


Figure 63 Peak to peak amplitude variation of the S_0 mode at 60mm offset on the left and right side of the paper insert

All data were processed using MATLAB. As data were collected over an increasing distance, the script was modified so only the highest peak to peak amplitudes were recorded among all signals which capture range was pre-set to 5 metres. The results from Figure 61 - Figure 63 show that the same MFC can repeatedly be lifted off the surface of inspection and still produce repeatable results. The test results also showed that the increase in amplitude was still being recorded up to 70 mm and 90 mm at the plate West and East sides respectively. The increased signal amplitudes in the South-North direction (from test location 17 to 28) were averaged and plotted from the West to East side view of the plate, as shown in Figure 64. To obtain another

profile of the propagation of the ultrasonic waves in this defective GFRP plate, test locations 17 - 28 from the 50 mm axis were added to Figure 64, to allow comparison between the signals far outside the damaged area and the signals near the paper insert.

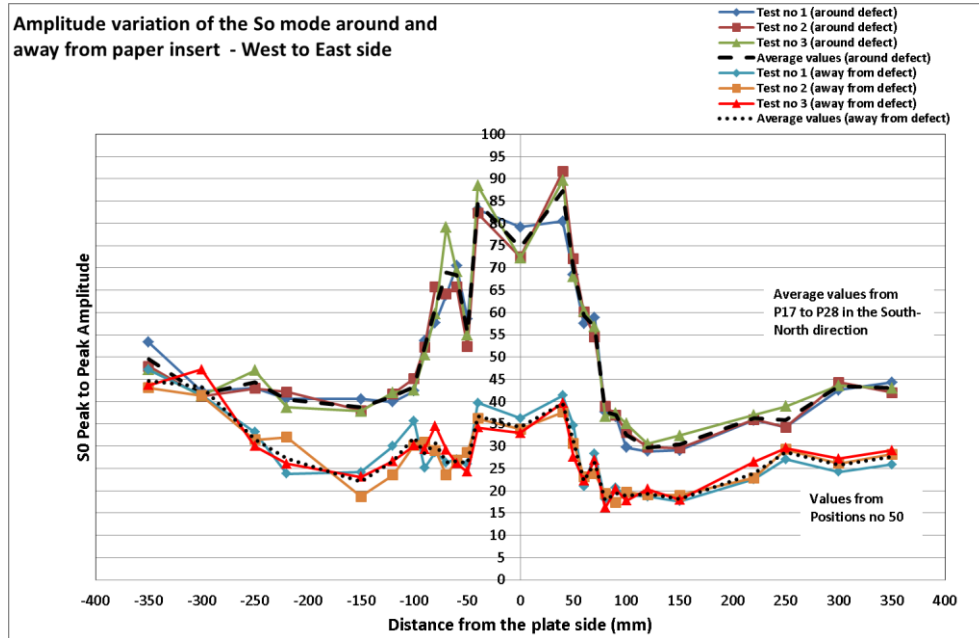


Figure 64 Variation of signal amplitude at multiple positions around the defect and at P50 from West to East

Figure 61-Figure 64 already showed that the paper insert was detected along its 25 mm length and now Figure 65 further demonstrates that the defect can also be detected across its width of 15 mm. In both directions, the MFC recorded the increase in signal amplitudes around the defective area. Data in Figure 64 display more resolution than in Figure 65, because much more data have been processed for Figure 64 than Figure 65. Figure 64 showed the accumulation of data collected between the positions 17 and 28 of the South-North direction while Figure 65 showed results for only a single receiving position.

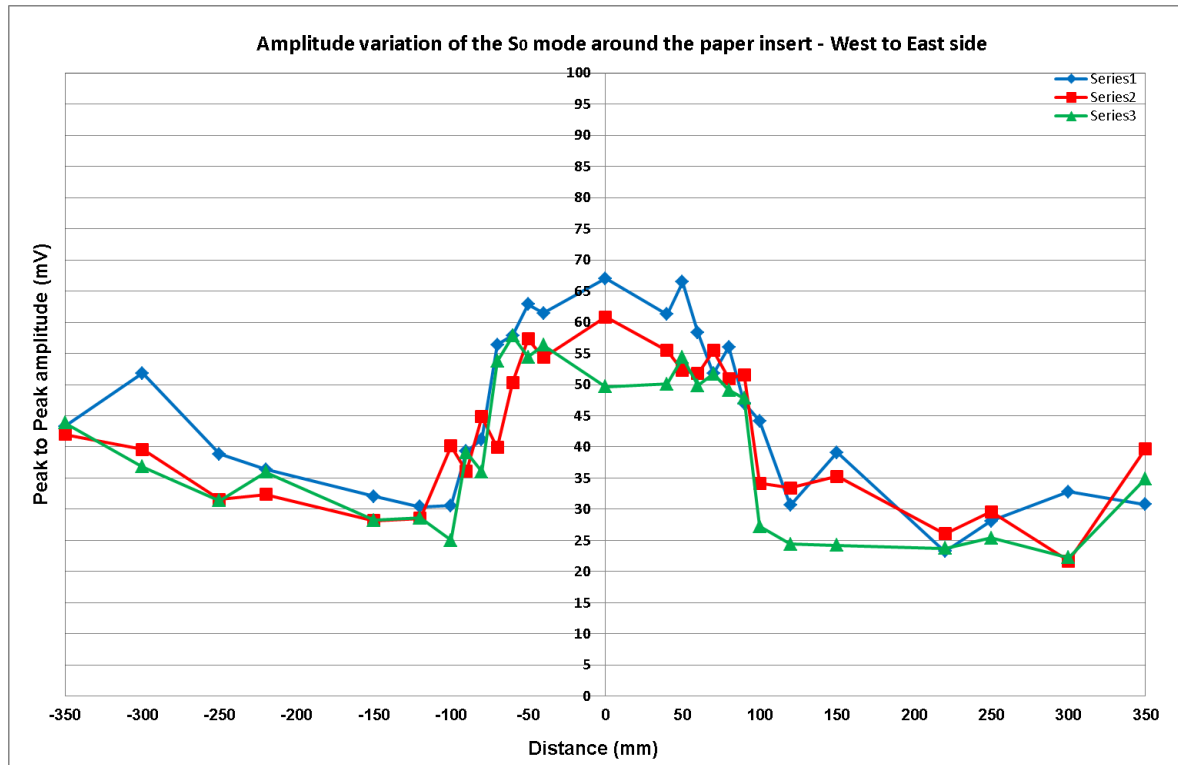


Figure 65 Variation of signal amplitudes at fixed receiving point between P23 and P24 and from West to East

5.3.5 Guided Wave Testing for delamination detection (sweep frequency)

A different script was used to process the data with MATLAB. It required (i) creating a matrix of data for each excitation frequency and (ii) producing individual image for the S_0 and A_0 modes, also applying the MATLAB Butterworth filter, to help visualise the propagation of the fundamental modes from both surfaces of the laminate. A total of 164 figures resulted from the sweep frequency experiment but in this section, only the first (40 kHz) and the last (80 kHz) results were shown. Images were produced not only to analyse the propagation of the S_0 mode but also to observe the propagation of the A_0 mode. The images represented the scanning area where the point of origin of the X-Y axis is the first position of the receiver at 350mm from the defect in the East side of the plate. *Surface A* results for the S_0 mode are shown in Figure 66.

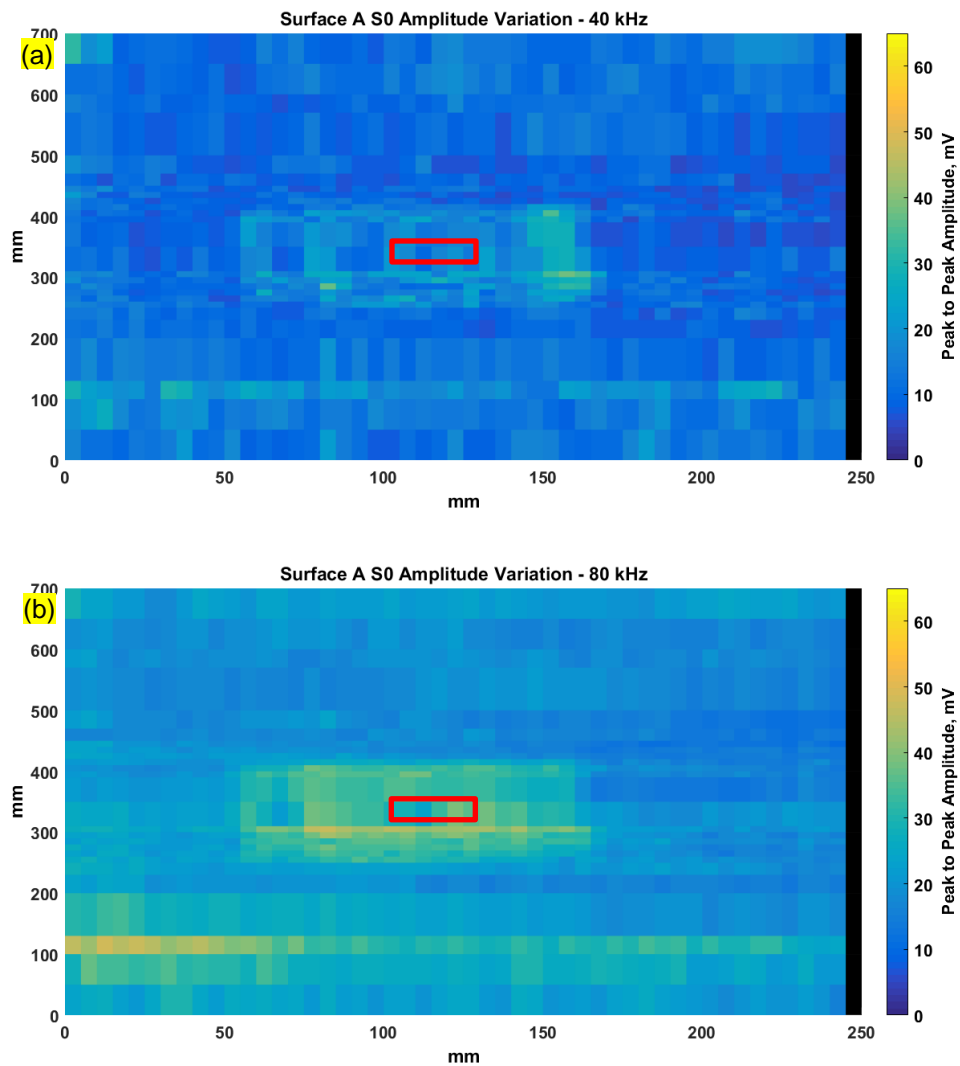


Figure 66 Amplitude variation of the S_0 mode around the paper insert for 40 kHz (a) and 80 kHz (b) excitation frequency— *Surface A*

The defect was located between 105 and 130mm approximately of the X-axis on the scaled image. For the S_0 mode, a small region depicting high amplitudes was identified after the defect (at around $X=150$ mm) for the 40 kHz excitation frequency but for 80 kHz, this region has enlarged and completely surrounded the defect. It can also be observed that for 80 kHz, high amplitudes emerged around the 100mm Y-position, between 0 and 75mm of the X-axis.

For the A_0 mode, higher amplitudes were more significant at 40 kHz than at 80 kHz (Figure 67).

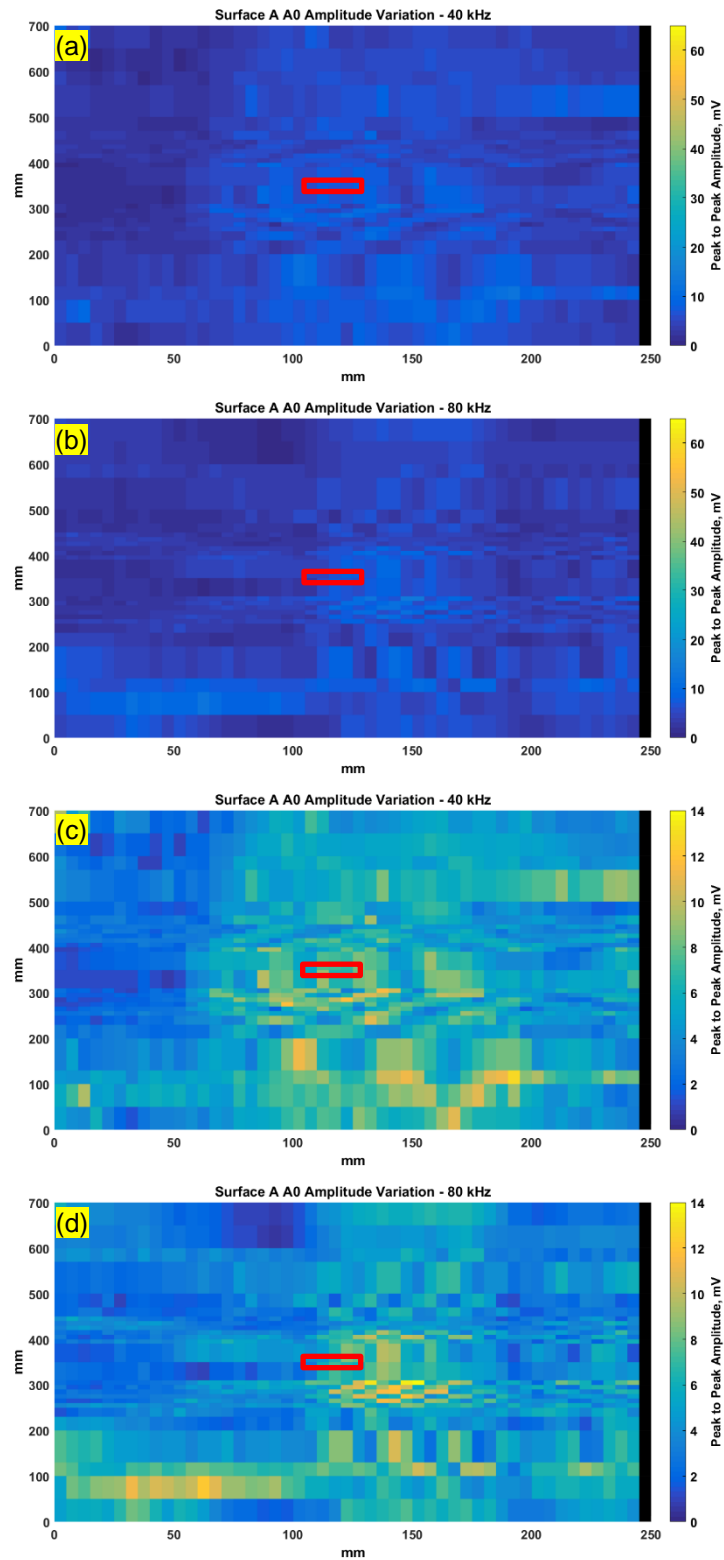


Figure 67 Amplitude variation of the A₀ mode around the paper insert for 40 and 80 kHz excitation frequency – *Surface A*; (a), (b) normalised amplitude scale; (c), (d) enlarged view of (a) and (b)

High amplitudes occurred near and around the defect but they were not as consistent as they appeared for the S_0 mode at 80 kHz. It can further be observed that for the A_0 mode in the 40 kHz test results, high amplitudes were recorded between the Y-positions 0-200mm and X-positions 100-200mm.

For the data collected from *Surface B*, the results for the S_0 mode were reported **Figure 68**.

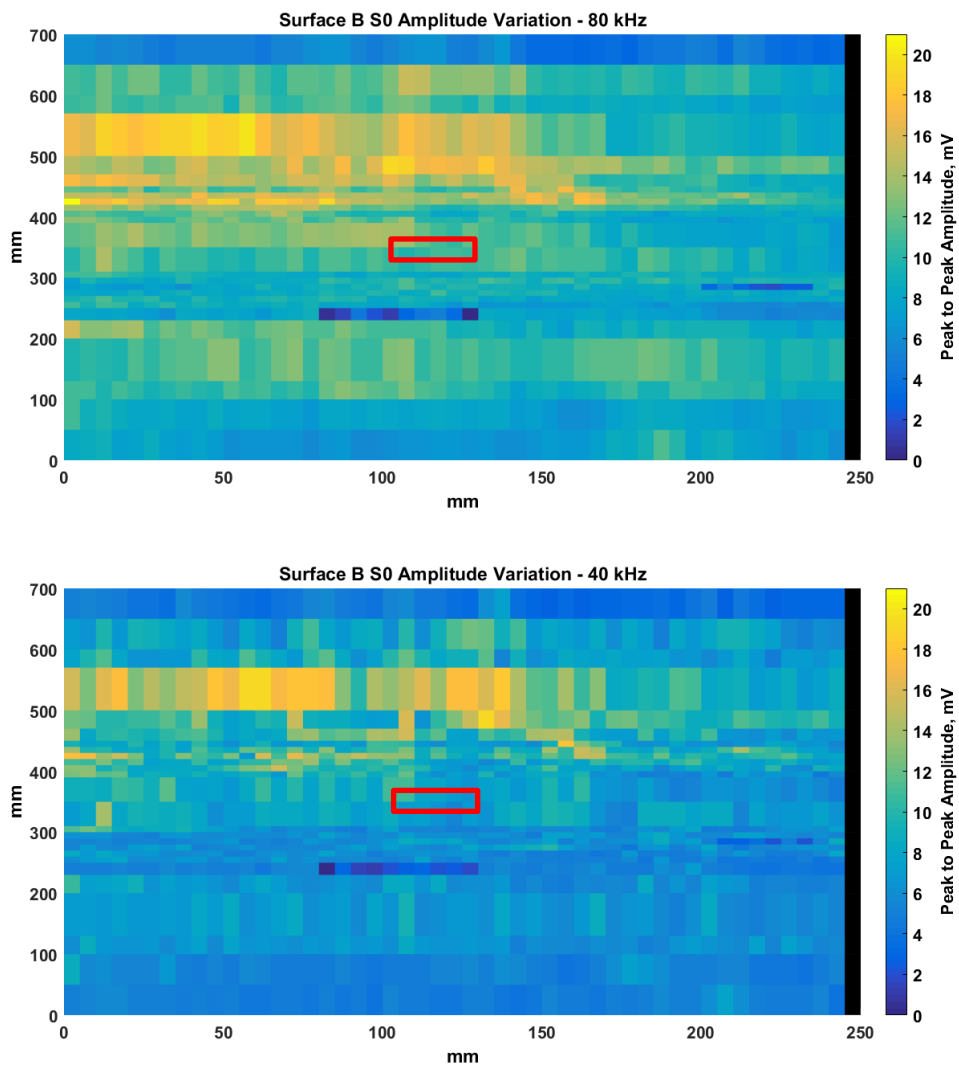


Figure 68 Amplitude variation of the S_0 mode around the paper insert for 40 and 80 kHz excitation frequency – *Surface B*

The high amplitudes which were captured from *Surface A* at the 80 kHz excitation frequency and at X-Y positions (0 to 75mm) - 100mm, were further highlighted in data collected from *Surface B* with the 40 kHz excitation signal. The 100mm Y-position from *Surface A* was approximately equivalent to the Y position 600mm from *Surface B*. It can be seen that between 600 and 500 mm, there were high amplitudes signals up to 150 mm on the X-axis, although these amplitudes were much higher on *Surface A* (up to 45mV). At the 80 kHz excitation frequency, the high amplitudes spreaded across the plate, possibly indicating that there might be much more than just a paper insert present in the GFRP laminate. The A_0 mode from *Surface B* has similar behaviour profile to the signals collected from *Surface A*.

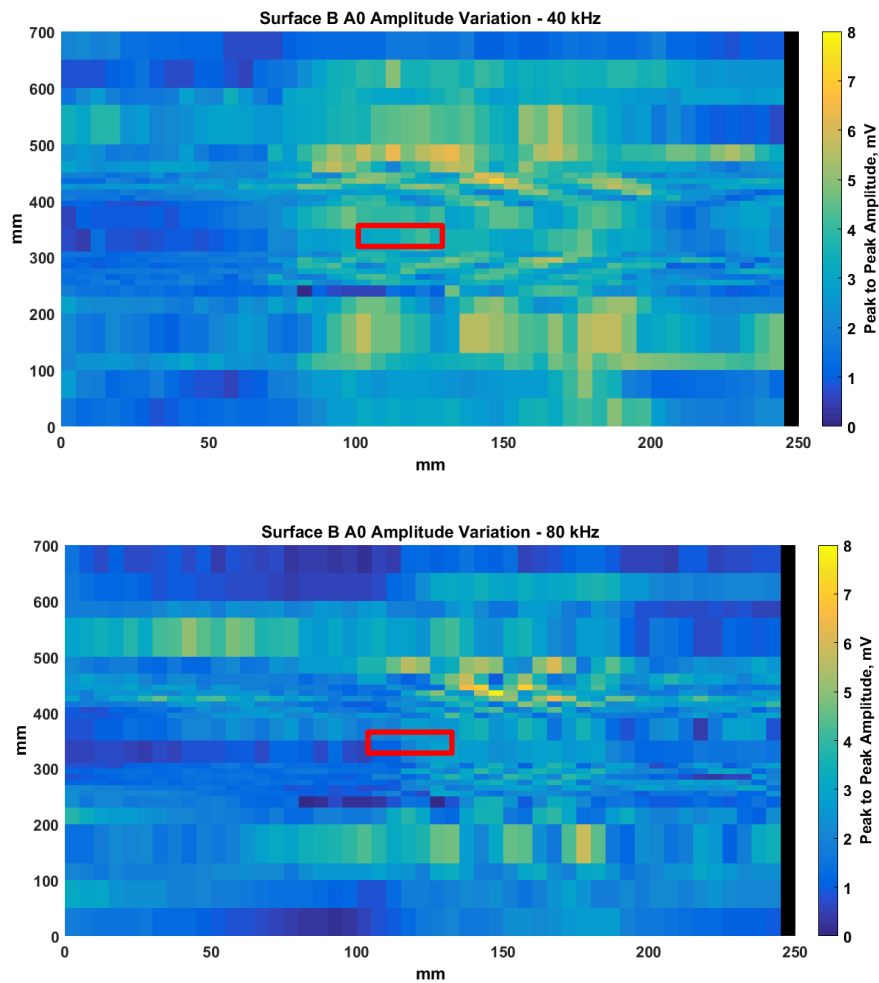


Figure 69 Amplitude variation of the A_0 mode around the paper insert for 40 and 80 kHz excitation frequency – *Surface B*

Higher amplitudes were also more significant at 40 kHz than at 80 kHz and although the high amplitudes occurred around the defect, there seemed to be no indication that the A_0 mode intercepted the piece of paper from both surfaces. Similarly, there are no indications that the S_0 mode detected the delamination from inspecting Surface B.

5.3.6 Validation technique: Scanning Laser Vibrometry for delamination detection

The results in Figure 70 showed that (i) the piece of paper has induced a higher signal amplitude when the S_0 mode reached the defect, (ii) the ripples present around the paper insert confirm the mode conversion into the A_0 mode by the paper insert and (iii) there seems to be no further indication of high amplitudes beyond the paper insert and no indication of additional defects within the area of inspection.

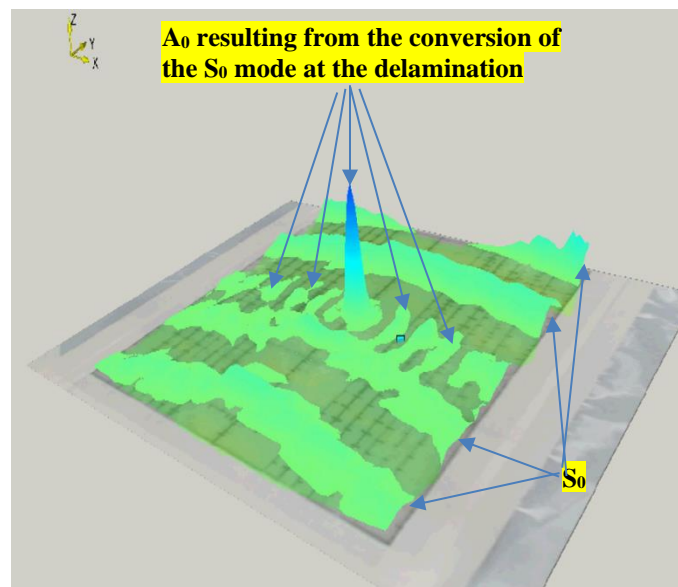


Figure 70 Test results from using Vibrometer

5.4 General discussion

As per the work carried out in Chapter 4, it was necessary to generate the dispersion curves (Figure 55-Figure 57) of the cross-ply laminate, in order to determine the distance limit

(between the transmitter and receiver), which will prevent overlap of the fundamental Lamb wave modes (S_0 and A_0). The detection of the 25*15mm piece of paper (delamination) was carried out in two stages:

The first stage consisted in determining whether the defect was detectable with the MFC sensor and technique used. Results were obtained for a receiver moving in the direction parallel to the plate X-axis (Figure 60-Figure 64) and moving in the direction parallel to the plate Y-axis (Figure 65). It was necessary to obtain the results in both axes to ensure that the results were repeatable, i.e., that the delamination has indeed been detected. These tests were executed at a single excitation frequency of 56kHz.

The second stage consisted in scanning the plate (from both surfaces) in the direction parallel to the plate X-axis and with a sweep frequency from 40 to 80 kHz (increment of 1 kHz). This frequency range was obtained from Figure 59, which showed the frequency response of the M2814 MFC coupled to the cross-ply GFRP plate. The focus here was on the lower and higher end of the frequency range (40 and 80 kHz), because of the high number (164) of images obtained. The results obtained from scanning the GFRP plate from the surface (A) closer to the defect are shown in **Figure 66-Figure 67**. For the opposite surface (B) of the plate, results are provided in Figure 68-Figure 69.

The presence of the delamination was further confirmed by using the Laser Vibrometer (Figure 70). This was achieved by carrying out pitch-catch tests using the Scanning Laser Vibrometer to collect data generated by MFC sensors, driven by an Eddyfi Teletest Focus+. Both tests indicated the presence of the paper insert, with the Laser Vibrometer easily confirming further that the A_0 mode was generated at the defect location.

Although the A_0 was easily detectable with the Vibrometer, its signal to noise ratio was extremely low in the two-staged experiments carried out with MFCs to transmit and receive

signals. **Figure 67** and **Figure 69** showed that the signals were too noisy for the detection of the paper insert; therefore, the A_0 results were deemed inconclusive. The S_0 mode showed more promising results. Figure 66 show the results from the interaction of the S_0 wave mode with the defect, when testing the laminate with an excitation frequency of 40 kHz and 80 kHz separately. Bearing in mind that the resolution limit in UT is half wavelength and the velocity of the S_0 mode was estimated at 3000 m/s within the 40-80 kHz, the test carried out at 40 kHz will be suitable for the detection of anomalies 37.5 mm apart. The test carried out at 80 kHz will be suitable for anomalies 18.75 mm apart. In the work discussed here, the anomalies refer to the edges of the paper insert. In Figure 66, data were collected in the plate X-axis where the distance between the edges of the paper insert was 25 mm. Therefore, the lowest frequency limit for distinguishing the edges will be 60 kHz. Figure 66 shows how increasing frequencies improves the resolution of the results. But, the high signal amplitudes area in Figure 66 does not depict the actual size of the damage. Instead, it pinpoints an area of interest, which will require further checks using follow-up NDT techniques such as conventional UT for example. In Figure 66, where data was collected from the surface close to the defect, it can be observed that the high amplitudes area is much bigger than the actual defect size. As reported in the literature, when the transmitted S_0 mode ($S_{0\text{transmit}}$) interacts with delaminations, it is partially reflected ($S_{0\text{reflect}}$), transmitted ($S_{0\text{transmit}}$) and converted into an A_0 mode ($A_{0\text{delamination}}$). Therefore, the high amplitudes area surrounding the defect can be attributed to these three wave modes which are overlapping close to the damage area. The disturbance caused by the paper insert starts even before the receiver reaches the defect, because it will start detecting $S_{0\text{reflect}}$ and $A_{0\text{delamination}}$ before it ends up above the defect. The literature showed evidence that the delamination will cause a loss in signal amplitudes. The literature further reported that it is possible to not only detect but also size the delamination with Lamb waves. These results were obtained in a

laboratory environment where the defect type, location and size are already known. Some of these results are also obtained by using transducers which are more receptive to certain wave modes than others. Results here showed that in an industrial environment and with guided wave sensors, it will be impossible to size the defect (if needed) as the guided wave sensor here (MFC) is sensitive to all type of wave modes (Lamb and shear). The work here showed that the guided wave sensor will detect a rise in signal amplitudes, because the sensor will not make a distinction between the various wave modes generated at the delamination site. Signal processing methods such the two-dimensional Fast Fourier transform (2DFFT) will allow separation of these wave modes in order to study them individually. But, for inspection purposes, where it is more important to know about the existence and location of a defect, increased signal amplitudes (instead of decreased amplitude as per the literature) will also indicate the existence of a defect, here the delamination.

Figure 68 showed that the S_0 mode could not detect the delamination when it is located further away from the surface of inspection, passed the mid-plane, unlike findings reported in the literature. This might be due to the excitation frequency used during the experiments. It is well known that the lowest the excitation frequency, the deepest the energy enters the material. Using an excitation frequency lower than 40 kHz could permit the S_0 mode to travel deeper in the material but test results will end up with poor resolution.

5.5 Conclusion

Unlike some of the findings reported in the literature, where decreased signal amplitudes suggested the presence of the delamination, a surge in signal amplitudes was detected here around the defective area. This surge was caused by the accumulation of ultrasonic wave modes surrounding the defect. Also, although the MFC was successful in detecting the defect, this could only be achieved from one surface, the one closest to the defect. This demonstrated that

the experimental set-up used here would be limited by the depth of delamination which is one-third of the material thickness here, unlike findings reported in the literature. The MFC sensors also proved their robustness: the receiver was lifted off the material surface up to 2700 times and not only the sensor was still functioning at the end of the experiments but test results remained repeatable. These results have showed that MFCs functioned well without permanent attachment to the material surface and therefore would be suitable for inspection of composites.

**Chapter 6: GUIDED WAVE MONITORING
OF WOVEN GFRPS UNDER THREE-POINTS
LOADING**

6.1 Introduction

The objective of the work carried out in Chapter 6 is to determine the sensitivity of guided waves to defects occurring during 3-point loading of bi-axial GFRP materials. The 3-point loading was carried out in order to recreate as much as possible a real-life scenario of damage growth in PMC. Other types of equipment were used to test the GFRP samples pre-three-point loading (PSV-3D only) and PSV-3D and X-Rays Microscopy for the post three-point loading tests.

The expected failure mode of a GFRP specimen during a 3-point loading is expected to be matrix/fibre breaking followed by multiple delaminations until the ultimate failure of the specimen. As per the literature review, matrix and fibre breakages affect the material Young's Modulus which degradation will not be reported in this chapter; instead, the focus will be on the most common type of defects known in composites: the delamination. As reported in Chapter 3 (Literature Review) when the transmitted S_0 mode ($S_{0\text{transmit}}$) interacts with the delamination, it is partially reflected ($S_{0\text{reflect}}$), transmitted ($S_{0\text{transmit}}$) and also converted into an A_0 mode ($A_{0\text{delamination}}$). The hypothesis is that the amplitude ratio between $A_{0\text{delamination}}$ and $S_{0\text{transmit}}$ could indicate the presence of a delamination and correlate with the extent of this defect. The ultrasonic wave parameters which will be monitored during the experiments are the peak-to-peak amplitude. The three-point loading investigation was conducted in three phases:

- Phase 1 consisted in collecting data pre-loading using the Thickness Shear PZT element as transmitter and the PSV-3D Laser Vibrometer as receiver
- Phase 2 consisted in carrying out guided wave testing pre-, during and post loading, using the Thickness Shear PZT elements as transmitter and receiver.

- And Phase 3 consisted in repeating Phase 1, i.e., collecting data post-loading using the Thickness Shear PZT element as transmitter and the PSV-3D Laser Vibrometer as receiver

6.2 Experimental protocol

6.2.1 Specimen manufacture

The plate which was tested for dispersion curves and transducer directionality in Chapter 4 was originally 4000 mm long and 2000 mm wide. A section of 1000 mm long and 2000 mm wide was extracted from that plate in order to produce as many beams as possible for the three-point loading tests. The GFRP beams used for the tests were 1000mm long, 40 mm wide, and still 4.5 mm thick. These beams were still made of 6 layers of fibres orientated at $[\pm 45^\circ]_6$ and arranged in twill weave pattern.

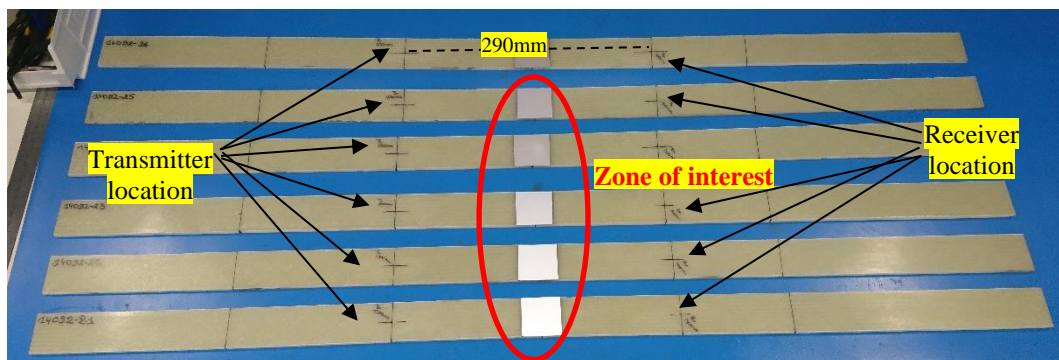


Figure 71 GFRP beams

6.2.2 Scanning Laser Vibrometry pre-loading and pre-damage insertion - Phase One

Before the three-point loading tests were carried out, the PSV-3D laser was used to scan the $20 \times 20 \text{ mm}^2$ area (highlighted in Figure 71 with reflective tape) around the predicted location of the highest stress levels i.e. where the load was applied. This “Phase One” test was carried out for detecting any potential (manufacturing) defects which might exist in that area. As reported

in the literature review and in Chapter 5, the scanning vibrometer has delamination detection capabilities.

Although results in Chapter 4 demonstrated that the MFC would be the most suitable for testing composites, PZT element were used here instead because these and the Teletest Transducers are most commonly used with the Teletest unit. These tests would allow creation of baseline results for any future experiments which would include any other transducers than the Thickness Shear PZT element/Teletest transducers. Also, the MFC could not be used due to previous research work showing that their coupling to the material may be affected during fatigue tests. The actuator PZT element was attached at 150 mm from the centre of the GFRP coupon (and centre of the area of interest) using super glue. It was driven with a 5-wave cycle signal enclosed in a Hanning window. The range of the excitation frequency was reduced from 66-130kHz to 106-130 kHz because of the length of the sample. Lower excitation frequencies would have caused overlap of the S_0 with the A_0 mode. A sweep frequency was carried out with an increment of 8kHz. The data acquisition was conducted with the PSV-3D with similar parameters to those selected for the transducer directionality experiment. Further details of “Phase One” experiment is shown in Figure 72.

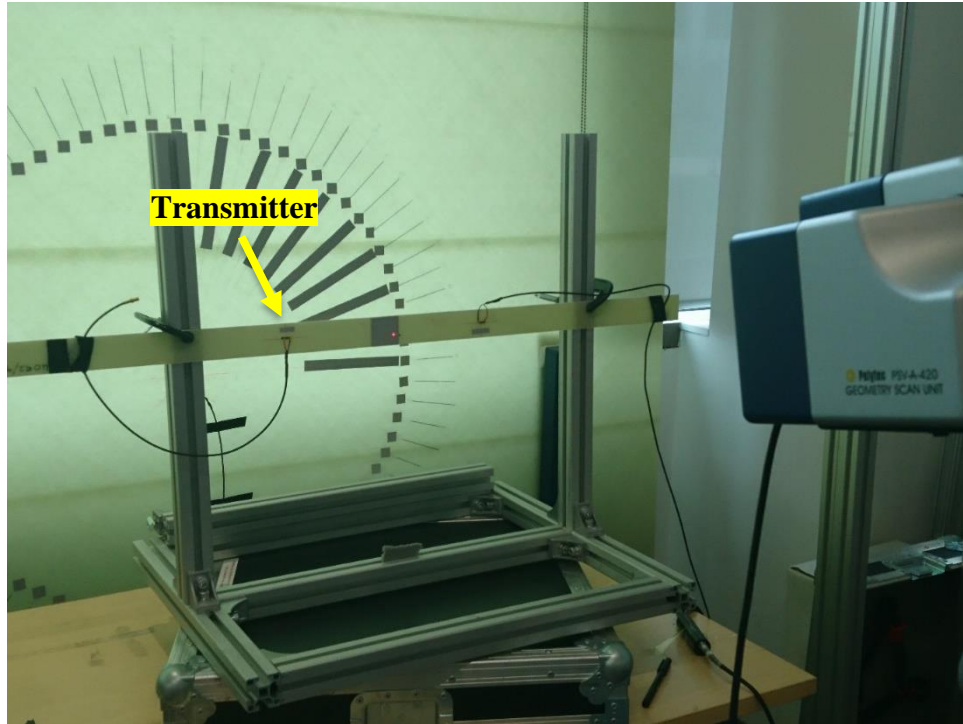


Figure 72 Phase One and Phase Three Test Set Up

6.2.3 Guided wave testing pre-, during and post loading– Phase Two

Sweep frequency, control sample and Guided wave testing pre-loading

The following step also consisted in scanning the coupon pre- three-point loading test but this time, using another PZT element as receiver instead of the PSV-3D laser. This was to allow recording of another baseline data for the guided wave testing during three-point loading. For this test, the receiver was placed on the other side of the area highlighted with reflective tape and at 140mm from the centre of the GFRP beam, making the overall distance between the transmitter and receiver equal to 290 mm. While the MK3 Teletest unit was used to drive the Thickness Shear PZT element in “Phase One”, the MK4 Teletest unit was used in Phase Two. The excitation signal in the pre-loading phase was the same as described in “Phase One”, a 5-wave cycle signal enclosed in a Hanning window with excitation frequency ranging from 106 to 130kHz by step of 8kHz. Pitch-catch tests were carried out. The outcomes of the pre-loading

phase are used as baseline data for the results for the three-point loading phase, which is described in the following sub-section.

Guided Wave testing during three-point loading

The first step of the three-point loading phase consisted in determining the maximum bending force for these GFRP coupons. The experiment was designed following the ASTM standard D7264/D7264M which was released for specimens 13.00 mm wide and 4.00 mm thick. The standard also recommended using a span-to-thickness ratio of 32:1, 16:1, 20:1, 40:1 or 60:1.

Because the movement of the coupon was restricted by the three-point loading test jig, the smallest support-span length was targeted, which was the closest the rollers could get - 76 mm – which is close to the 16:1 span-to-thickness ratio.

The speed of testing was determined following the D790 Standard Test Methods and was found to be 12mm/min. The initial three-point loading test was carried out on three samples (for repeatability) without any transducers attached. The results showed that the average maximum force, leading to complete failure of the beam, was 2.77 kN. With this force, the beam had reached a maximum displacement of approximately 12 mm. The second step of the three-point loading phase consisted in determining the speed of testing. For the purpose of carrying out GWT during the three-point loading, the speed of testing was reduced down to 4mm/min to allow slow growth of the failure modes.



Figure 73 Set-up of three-point loading test

Guided Wave testing post loading

GWT during post loading stage consisted of collecting data as soon as the load was released from the GFRP beam. Deflections, from 3 to 8 mm with an increment of 1 mm, were initially investigated. Three samples were tested for each of these displacements for test repeatability purposes.

Table 2 Specimen ID set for deflection from 3 to 8mm

Deflection (mm)	Specimen ID
0	14092/10 – Control machine
3	14092/9; 14092/11; 14092/12
4	14092/13; 14092/14; 14092/15
5	14092/16; 14092/17; 14092/18
6	14092/19; 14092/20; 14092/21
7	14092/22; 14092/23; 14092/24
8	14092/25; 14092/26; 14092/27

Control sample

While all specimens were tested with GWT during three-point loading, a controlled sample was also undergoing GWT in parallel with the specimens. The control sample was located outside the three-point loading test rig. Results from the controlled sample were necessary because if

changes in the guided wave data were observed from samples under loading but not from the controlled sample, it would mean that these changes were due to the material properties being compromised during the three-point loading phase.

6.2.4 Scanning Laser Vibrometry post loading – Phase Three

Phase Three is exactly the same as Phase One but post three-point loading.

6.2.5 Validation techniques

Three additional NDT techniques were used on the GFRP beams, during and post three-point loading phases, for comparison purpose with guided wave testing. These techniques were:

- Visual inspection post three-point loading
- X-ray micro-computed tomography post three-point loading
- Acoustic Emission during three-point loading

6.3 Results and discussion

6.3.1 Scanning Laser Vibrometry pre-loading and pre-damage insertion - Phase One

The Vibrometry test results for the pre-loading stage are shown in **Figure 74 - Figure 76**. These results show the surface velocity of the material against a specific point in time (vertical red line). While Figure 74 and Figure 76 exhibit similar results, **Figure 75** shows higher surface velocity which could possibly have been caused by factors such as the coupling of the transducer/reflective tape and the existence of flaws. The principle behind the research work reported in this chapter is that these will be used as baseline data which will be compared against the results obtained post three-point loading tests, in order to assess whether damage growth (if any) can be monitored.

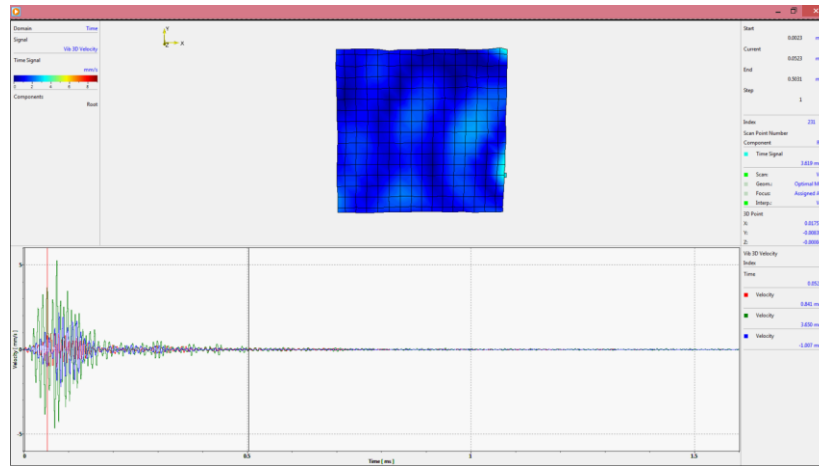


Figure 74 Test results for Beam no.14092/9 for 106 kHz excitation frequency

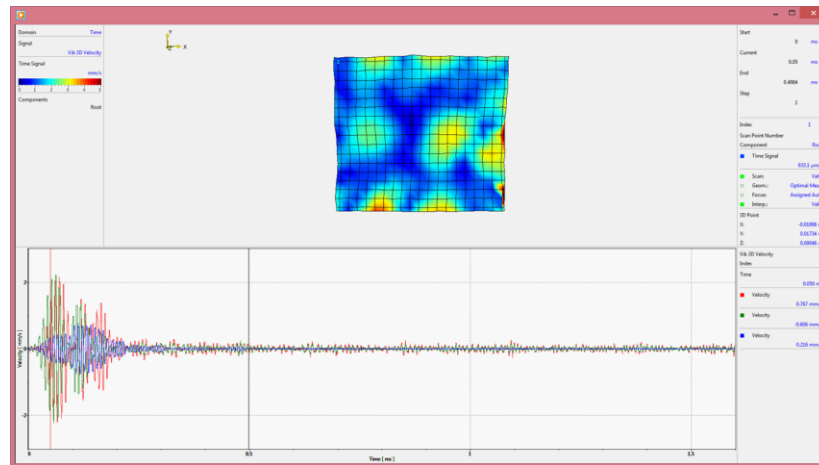


Figure 75 Test results for Beam no.14092/11 for 106 kHz excitation frequency

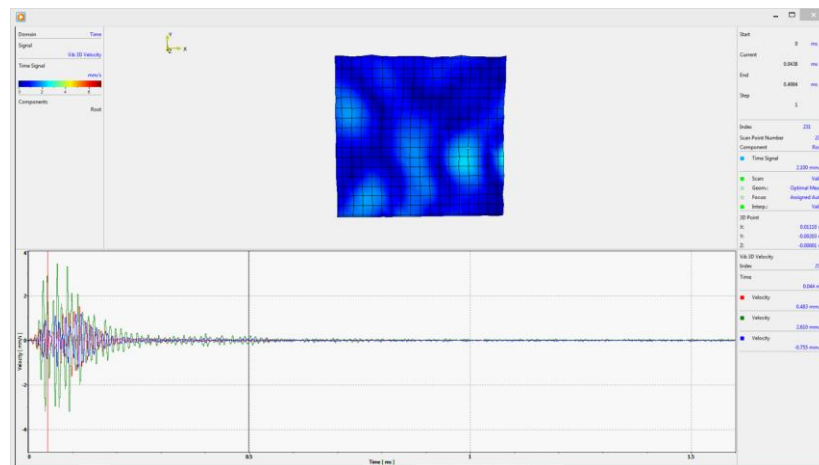


Figure 76 Test results for Beam no.14092/12 for 106 kHz excitation frequency

6.3.2 Guided wave testing pre-, during and post loading – Phase Two

Sweep Frequency

A sweep frequency was carried out from 106 to 130 kHz, with an increment of 8 kHz, on each of the coupon pre, during and post three-point loading. Test results (**Figure 77 - Figure 80**) showed that 130kHz (**Figure 80**) was the most suitable frequency as it showed the best signal resolution. Therefore, the remaining data analysis was focussed on the 130kHz excitation frequency.

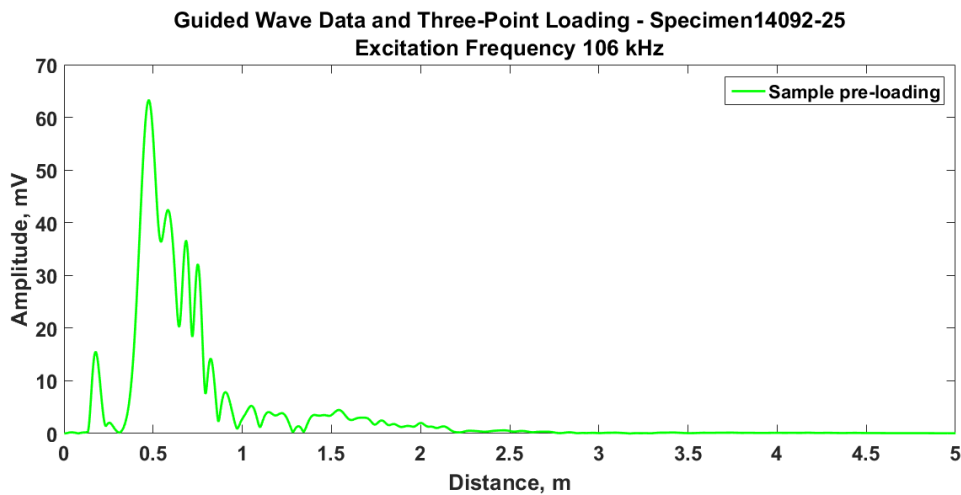


Figure 77 Data collected pre three-point loading – Specimen 14092-25 – 106kHz

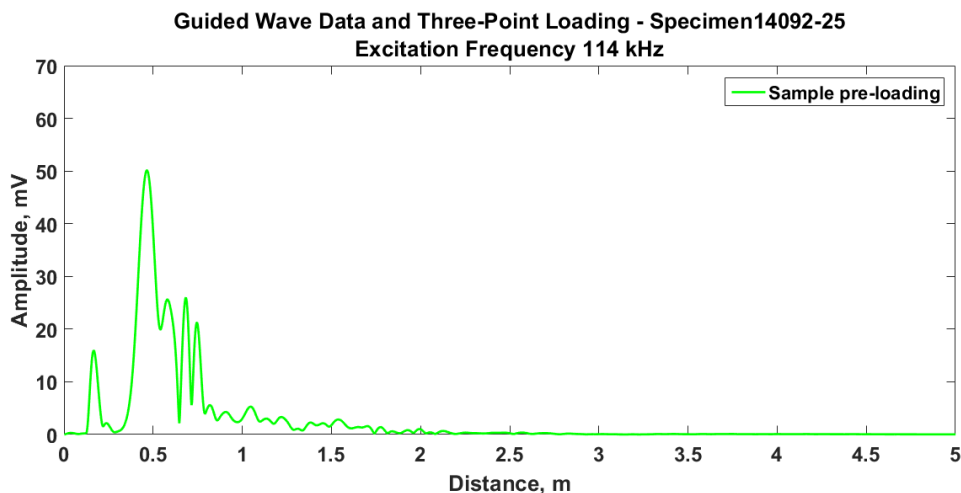


Figure 78 Data collected pre three-point loading – Specimen 14092-25 – 114kHz

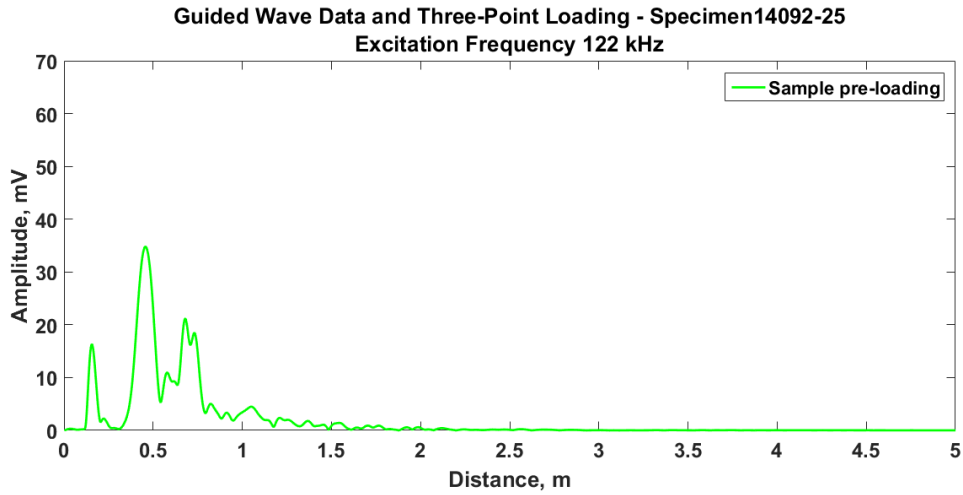


Figure 79 Data collected pre three-point loading – Specimen 14092-25 – 122kHz

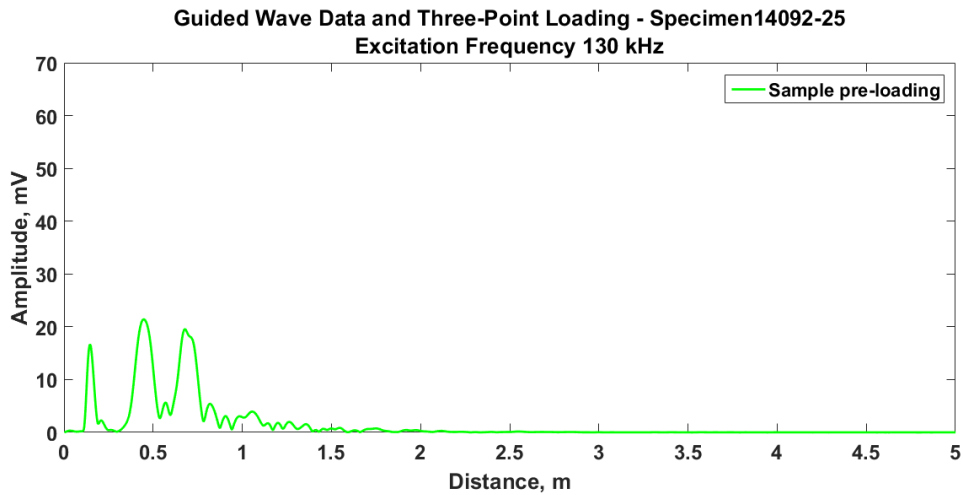


Figure 80 Data collected pre three-point loading – Specimen 14092-25 – 130kHz

Control sample

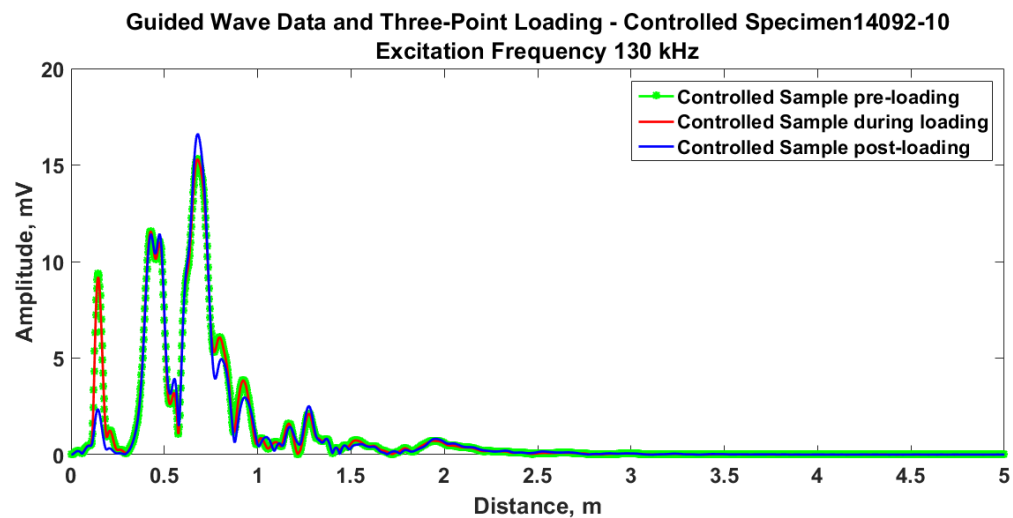


Figure 81 Control Specimen 14092/10 during loading of Specimen 14092/25

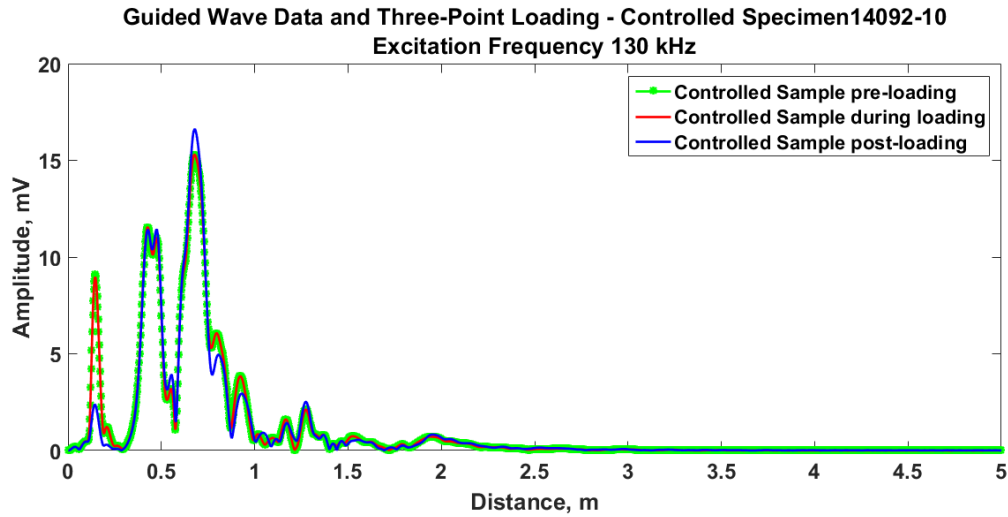


Figure 82 Control Specimen 14092/10 during loading of Specimen 14092/26

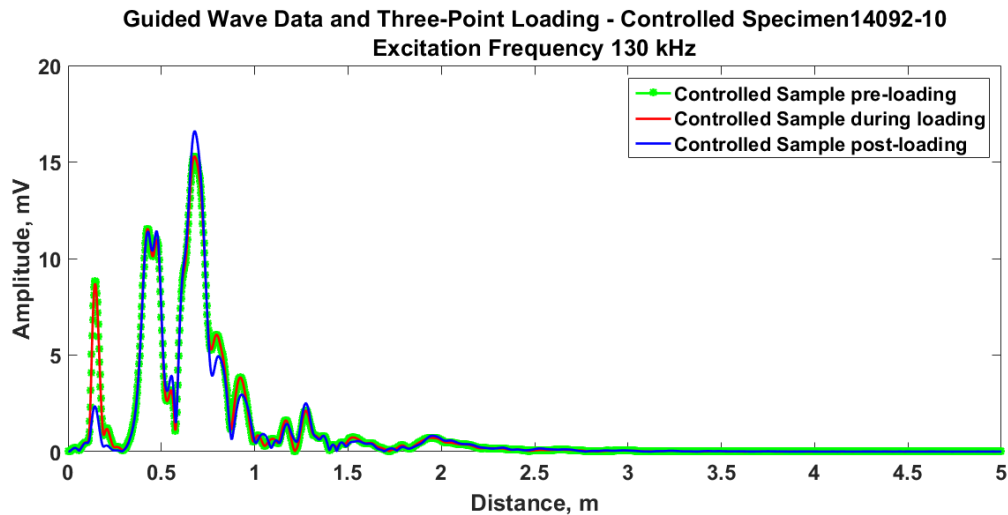


Figure 83 Control Specimen 14092/10 during loading of Specimen 14092/27

Figure 81 - Figure 83 showed that the guided wave data from the controlled sample were stable during loading of the other GFRP beam specimens.

Guided Wave Testing pre-, during and post loading

The raw data showed in **Figure 84**, were processed using a MatLab scriptfile in order to obtain the results from testing specimens 14092/25 (**Figure 85 - Figure 88**). As reported in Chapter 4, up to four wave modes were identified in the frequency range 66-130kHz. From the fastest

to the slowest wave mode, these were the S_0 , SH_{02} , SH_{01} and A_0 modes. These wave modes were further identified in the raw data (**Figure 84**).

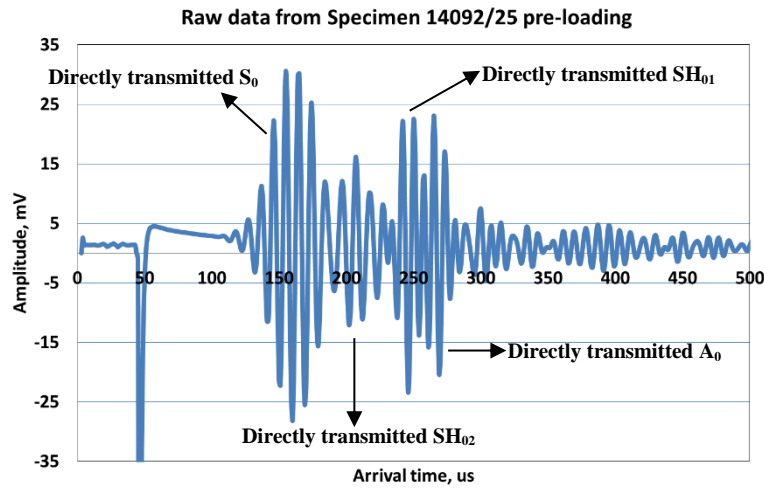


Figure 84 Raw data from Specimen 14092/25 pre loading - 130kHz

The velocity of the four wave modes in the GFRP beam were established from the raw data: 2612 m/s for the S_0 , 1542 m/s for SH_{02} , 1277 m/s for SH_{01} and 1178 m/s for the A_0 . All guided wave data collected pre-during-post three-point loading were processed using MatLab to make it easier to pick at differences in signals between the three stages of loading. The MatLab scriptfile used for data processing allowed peak amplitudes to be plotted relative to four known velocities. For example, data displayed in **Figure 85** assumed that all wave modes in the raw data has the velocity of S_0 mode. While all wave modes were correctly identified, the only correct distances from the transmitter are the ones for the peak amplitudes related to S_0 and its reflections. In **Figure 86**, it can be observed that all peak amplitudes were shifted to left because they were plotted in relation to a slower wave mode (SH_{02}) than the S_0 and so on. In all the following figures (**Figure 85 - Figure 88**), the interest was focussed on the peak amplitude of the directly transmitted wave, where the distance scale (x-axis) was relative to its own velocity. This meant (i) in **Figure 85**, the focus was on the directly transmitted S_0 ; (ii) on the directly transmitted SH_{02} in **Figure 86**; (iii) on the directly transmitted SH_{01} in **Figure 87** and on the

directly transmitted A_0 in **Figure 88**. The very first peak amplitude observed in **Figure 85** - **Figure 88** originated from the electronic unit (MK4 Teletest) and was not considered during analysis.

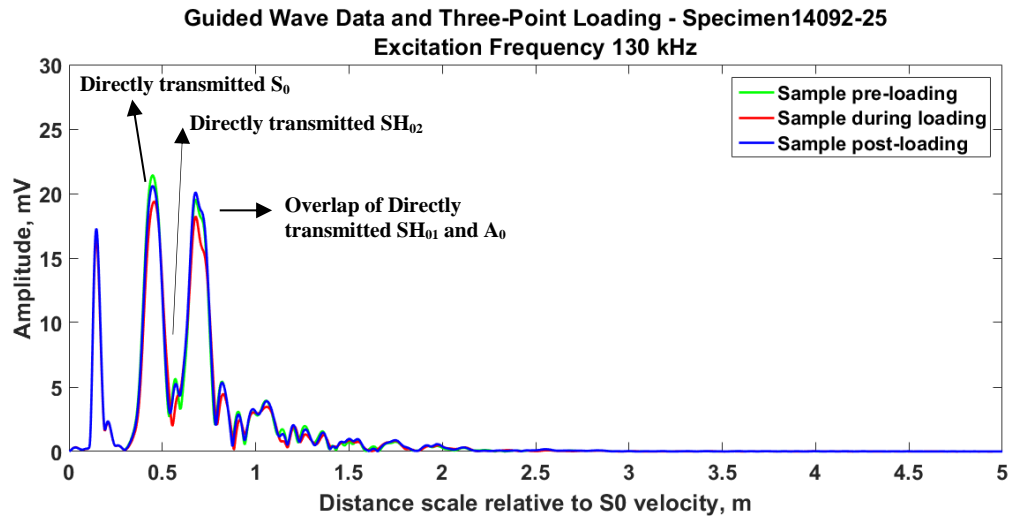


Figure 85 Pre-during-post loading GW data relative S₀ velocity - 8 mm deflection

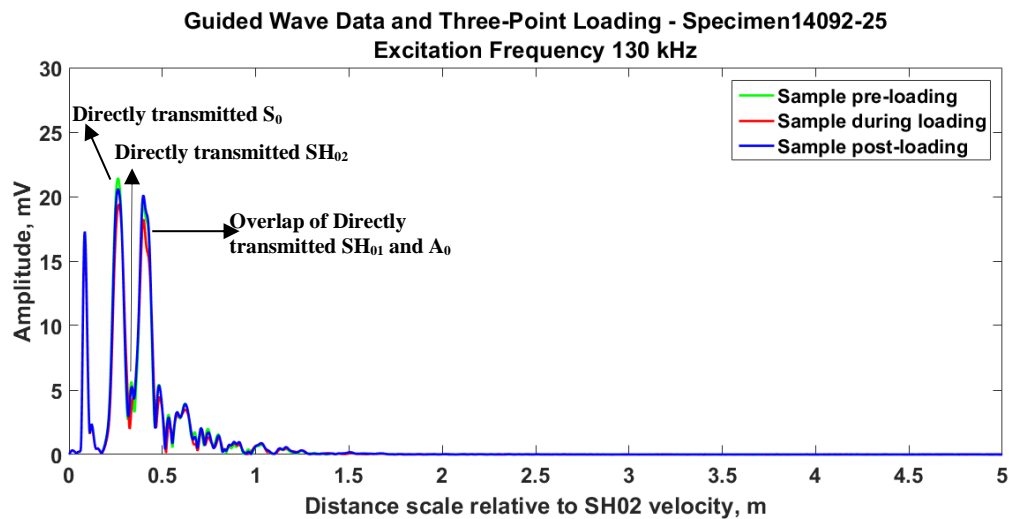


Figure 86 Pre-during-post loading GW data relative SH₀₂ velocity - 8 mm deflection

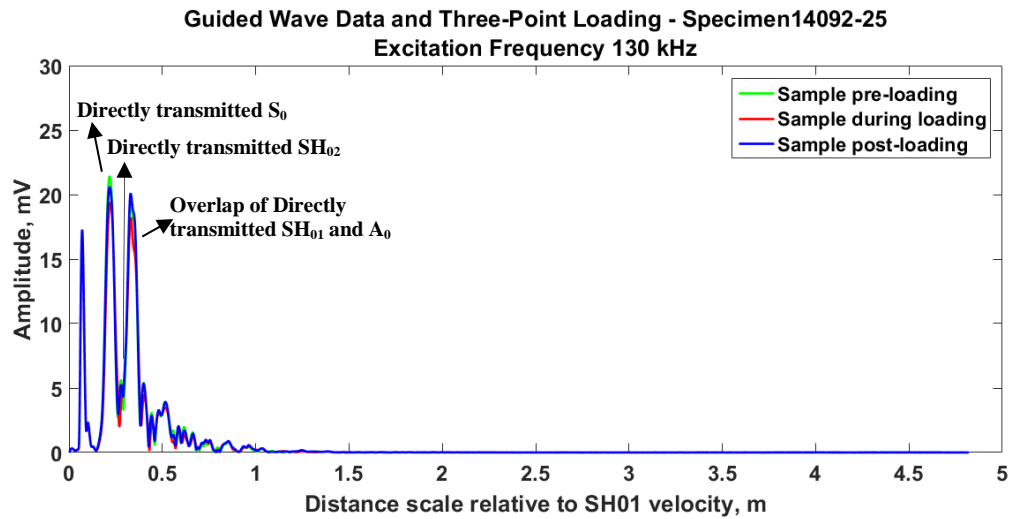


Figure 87 Pre-during-post loading GW data relative SH₀₁ velocity - 8 mm deflection

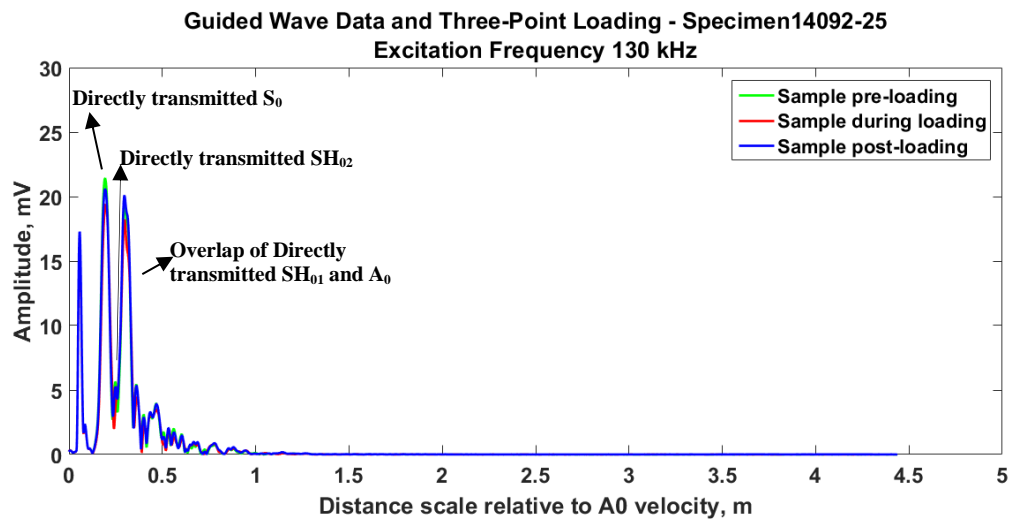


Figure 88 Pre-during-post loading GW data relative A₀ velocity - 8 mm deflection

Results show that directly transmitted S₀, SH₀₁ and A₀ encountered amplitude drops during loading with the amplitudes returning close to its pre-loading value after the load was removed. Not so much could be said about the SH₀₂ at this stage because, it was relatively very small compared with the other modes; therefore, it was difficult to assess from results showed in **Figure 85 - Figure 88**.

6.3.3 Baseline subtraction approach to damage detection

In order to assess whether the “amplitude drop” was only due to the bending of the material, Additional GFRP beams were further tested for deflection from 9 until their complete failure (12 mm deflection as reported earlier).

Table 3 Specimen ID set for deflection from 9 to 12mm

Deflection (mm)	Specimen ID
9	14092/28
10	14092/29
11	14092/30
12	14092/31

Only one GFRP beam was tested for each of these additional deflections. To determine whether there was a trend in all data collected, the differences in signal pre and post loading were plotted against all deflection and for all samples. A trend was assessed for each of the four wave modes. These results are shown in **Figure 89 - Figure 92**. Obviously, the biggest the amplitude drop was post loading, the biggest the difference was in signal pre-post loading.

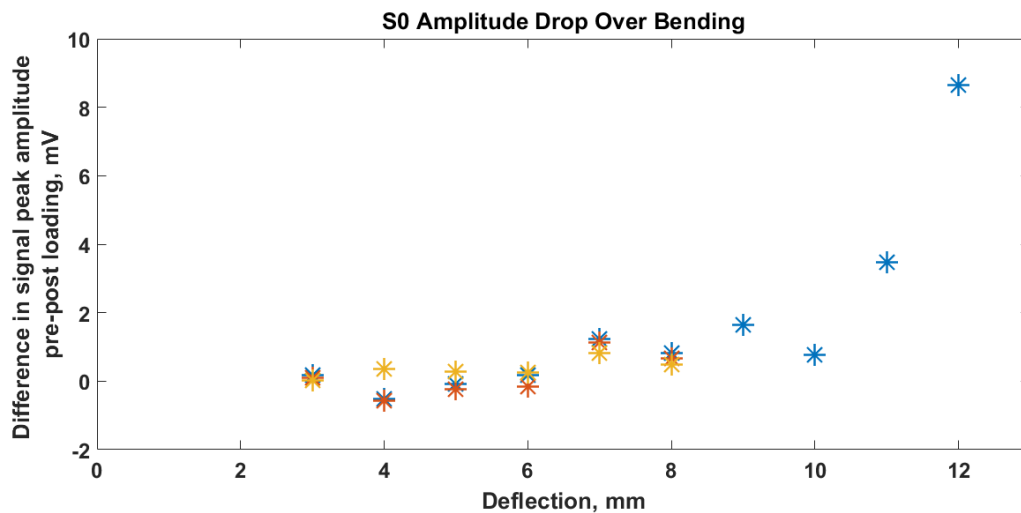


Figure 89 S₀ Amplitude Drop over Bending

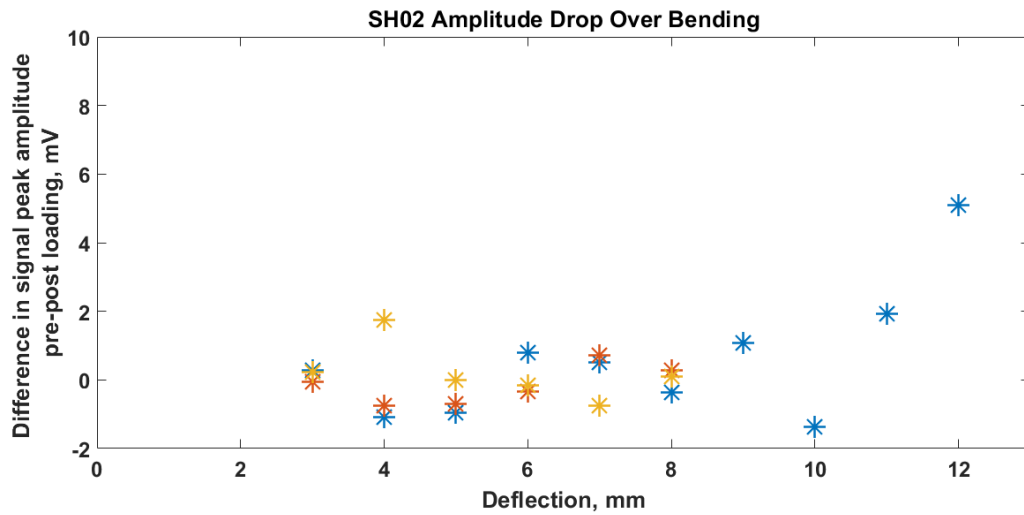


Figure 90 SH₀₂ Amplitude Drop over Bending

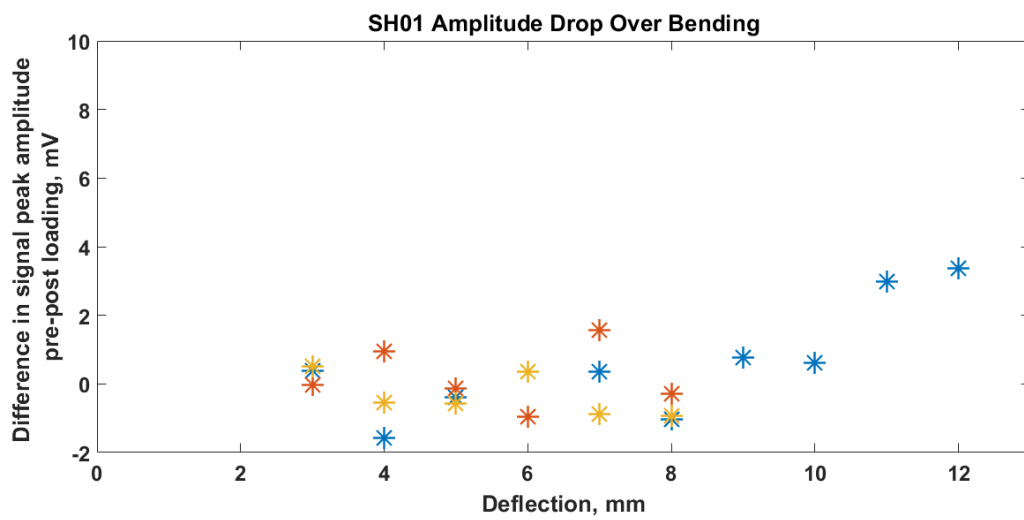


Figure 91 SH₀₁ Amplitude Drop over Bending

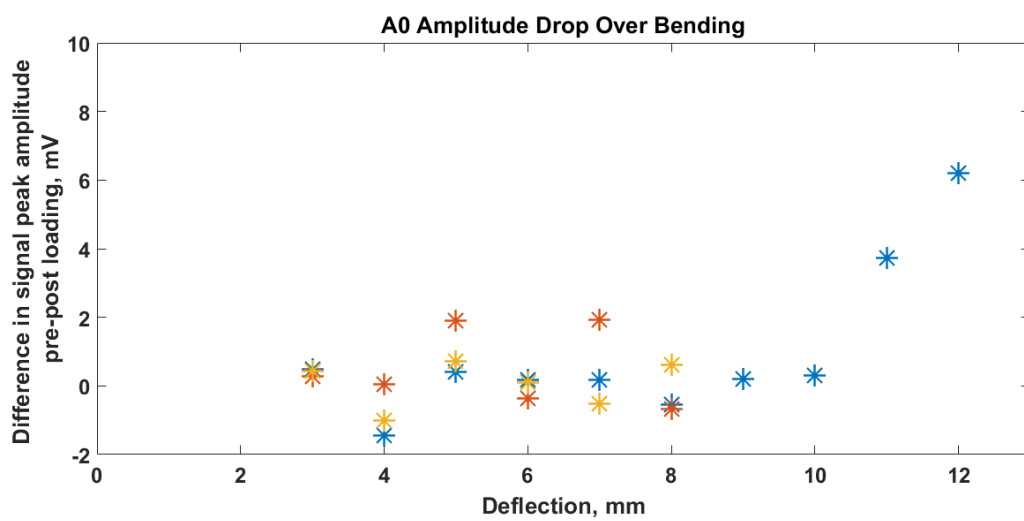


Figure 92 A₀ Amplitude Drop over Bending

Results show that for an excitation frequency of 130 kHz, the amplitude of the directly transmitted S_0 , SH_{02} and A_0 dropped linearly from the 11 mm deflection mark. This behaviour was not that obvious for the SH_{01} mode. This could have been caused by a poor separation between the A_0 and SH_{01} modes (**Figure 84**) which overlapped at several instances, making it difficult to detect the peak amplitude of the SH_{01} .

6.3.4 Scanning Laser Vibrometry post loading – Phase Three

Vibrometer testing was further carried out post loading, in order to compare results with guided wave testing. The focus was on the specimen subjected to the 8 mm deflection. Test protocol was the same as the one described by “Phase One” experimental protocol. In comparison with the pre loading data, the post loading results show increased amplitudes but nothing obvious which would indicate the presence of cracks and delamination.

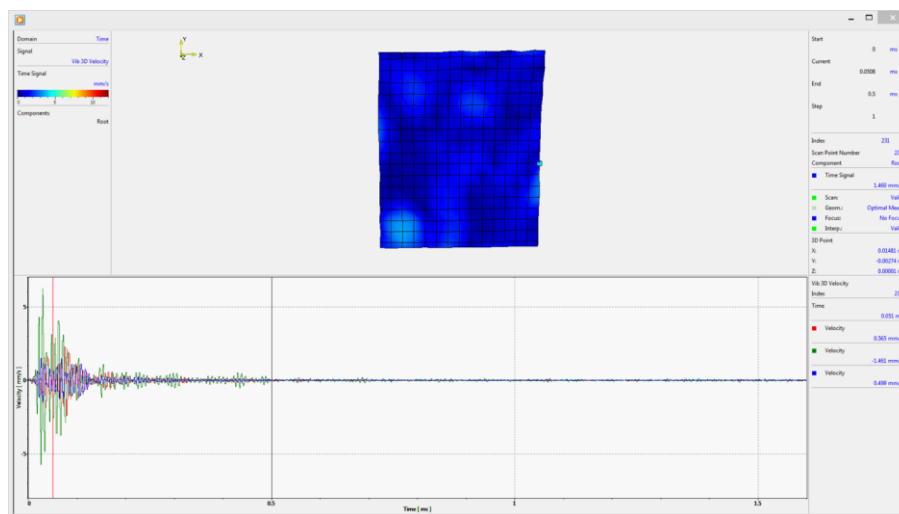


Figure 93 Vibrometry testing pre three-point loading

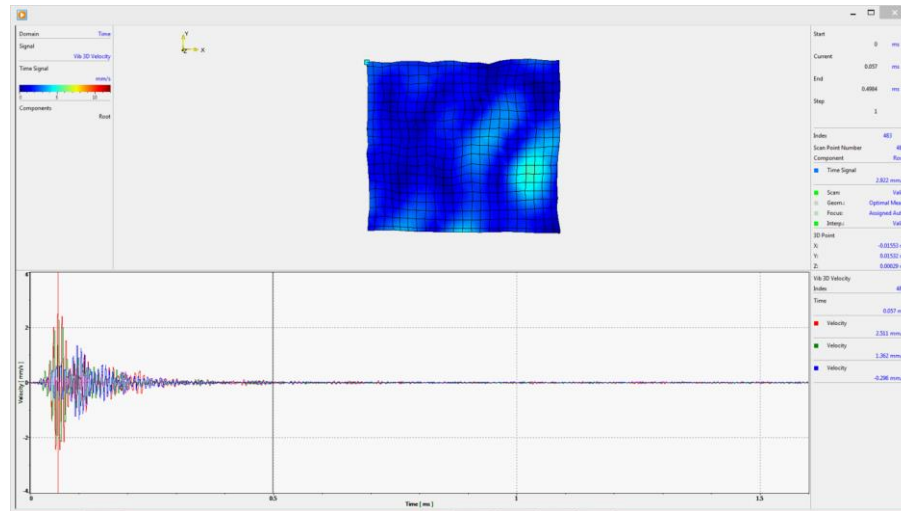


Figure 94 Vibrometry testing post three-point loading for 8 mm deflection

6.3.5 Validation techniques

Visual inspection

Figure 95 showed the inner and outer bends of specimen 14092/25 and 26, post loading at a deflection of 8 mm. **Figure 96** showed results from specimens 14092/28-31, post loading at 9, 10, 11 and 12 mm deflection respectively.

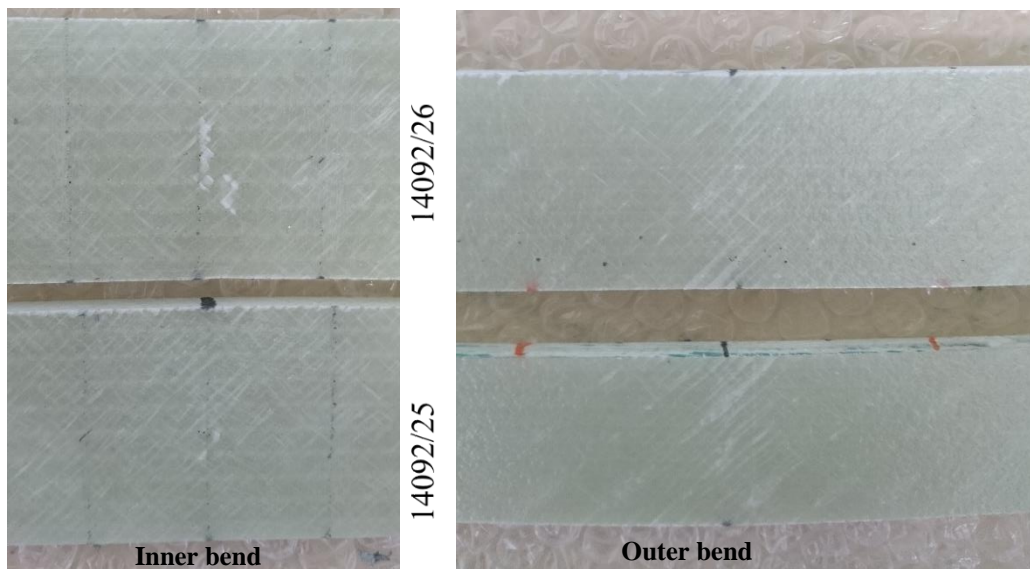


Figure 95 Visual inspection of specimen 14092/25-26

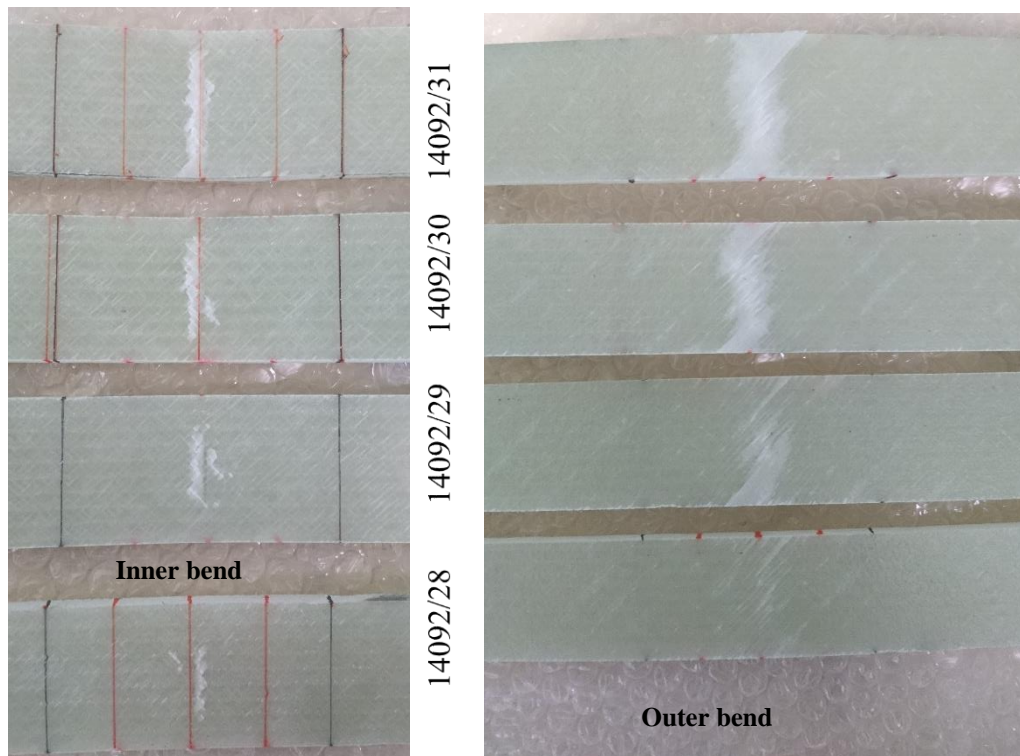


Figure 96 Visual inspection of specimen 14092/28-31

It can be observed that no critical surface changes occurred at the 8 mm deflection stage. For specimen 14092/28, the outer bend is not so different from 14092/25-26 while its inner bend showed a little more change to the surface. But at this point still, nothing critical is observed. Significant changes started arising for the 10 mm deflection result, where it can be observed that a layer was pulling away. From that point, the damage got worse until complete failure (Specimen 14092/31).

X-ray micro-computed tomography post three-point loading

Specimen no 14092/27, which was subjected to the 8 mm displacement, has its length reduced to 100 mm, in order to fit in the ZEISS Xradia 5xx Versa X-Rays machine. The specimen was placed 69 mm from the source and 51 mm from the detector which magnification was set at 0.4X. The acceleration voltage was 50kV for an exposure time of 4 seconds. The resolution was set to the lowest possible which was 40 μm for this machine. The test set-up for the X-ray micro-computed tomography is depicted **Figure 97** and results are shown in **Figure 98**.

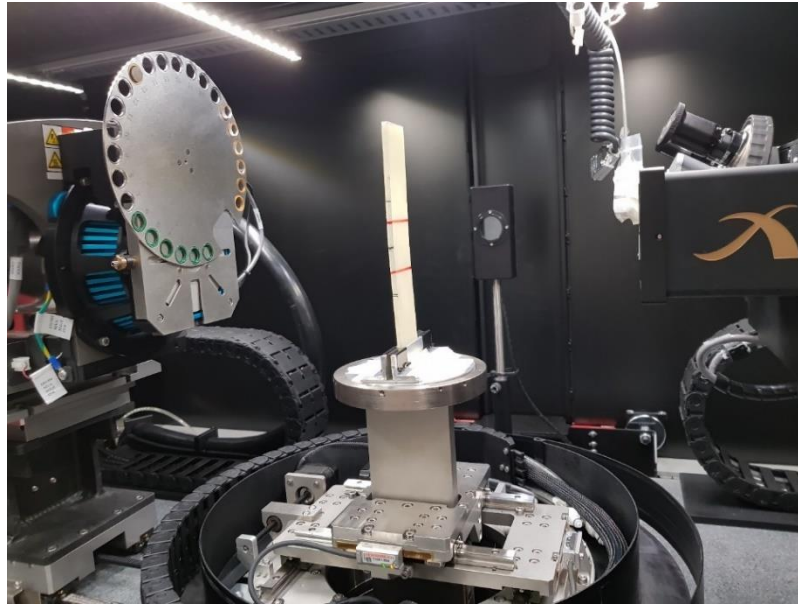


Figure 97 Test set-up for X-ray tomography of Specimen 14092/27 - post loading

The results show the health condition of few layers through the thickness of the GFRP beam. It can be observed that the X-ray tomography has not picked any defects post the three-point loading of Specimen 14092/27 for a deflection of 8mm.

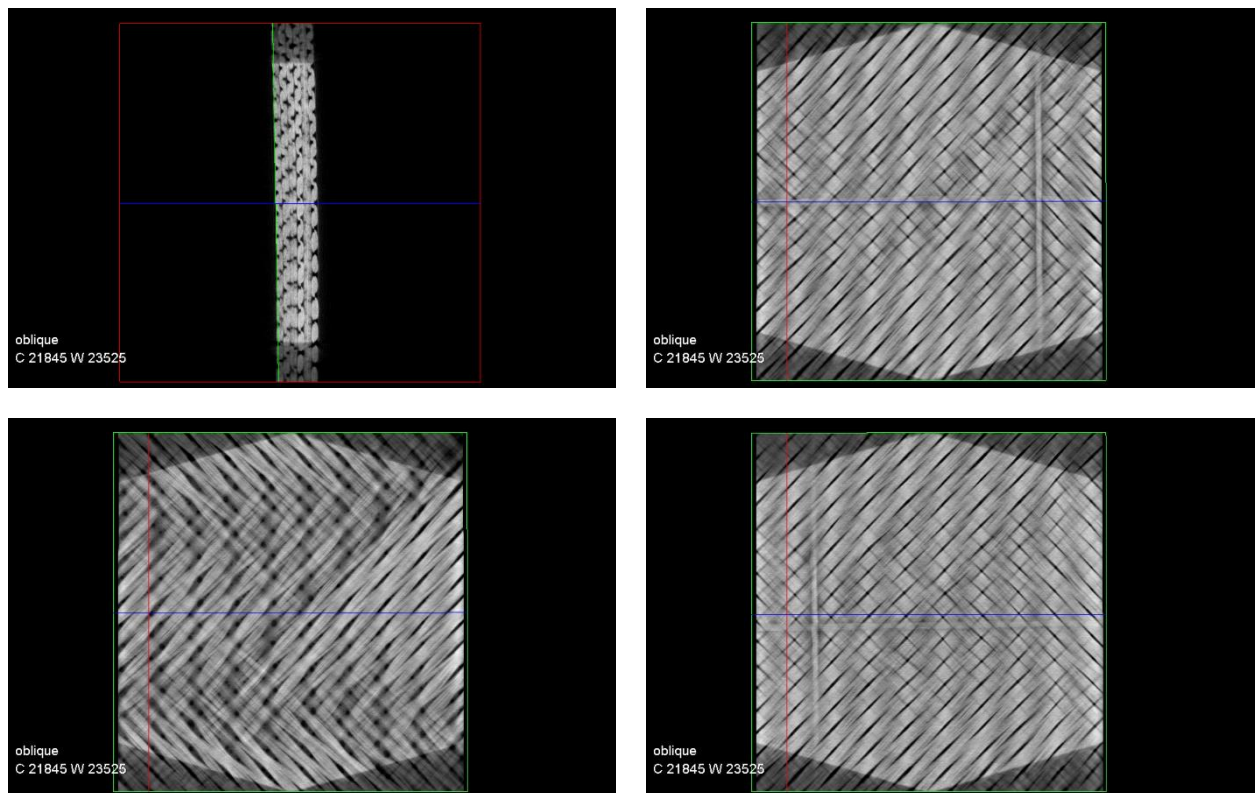


Figure 98 X-ray tomography results for Specimen 14092/27 - post loading

Acoustic Emission during three-point loading

The sensitivity of AE technique was investigated for the 8 mm deflection. Tests were carried out by Jialin Tang ^[174] who was also studying defect detection in composite materials but using Acoustic Emission equipment. She used the Vallen AMSY-6 data acquisition system and two VS150-RIC sensors. These sensors have a frequency bandwidth of 100-450kHz and a frequency response of 150 kHz. The first AE sensor was placed 100 mm from the predicted source of energy (the loading point). The second sensor was placed 200 mm from the source. Preliminary tests showed that the testing speed of 4mm/min was too fast for the AE test; therefore, the speed of testing during for three-point loading was reduced to 1 mm/min (instead of 4mm/min for the guided wave testing).

Tang ^[174] explained that damage could be detected through frequency domain analysis. She reported that the literature suggested that matrix cracking generated signals of frequency contents of 30–150 kHz. Delamination and debonding transmitted signal of frequency contents of 200-300 kHz while fibre breakage/pull out would create signals of frequency contents above 300 kHz. Based on her test results, she suggested that during the three-point loading test for 8 mm deflection, the AE sensors had detected fibre breakage, matrix cracking and delamination.

6.4 General discussion

Before carrying out the GWT of the GFRP beams during 3-point loading, it was necessary to set some pre-requisites. The first was the baseline results obtained from testing the beams with the EddyFi Teletest and with the Laser Vibrometer, which had reliably detected delamination, as reported in Chapter 5. Examples of baseline results obtained for the Vibrometer are shown in Figure 74-Figure 76. The data were collected from three separate and healthy samples. Examples of baseline results obtained with the Teletest are shown in Figure 77-Figure 80. These results emerged from the sweep frequency tests carried out from 106 to 130 kHz (by step of 8

kHz) on a healthy sample as well. These results further demonstrated that the most suitable test frequency was 130kHz, as it showed the best signal resolution. The second pre-requisite was to use a control sample to ensure that any unusual recorded data was solely due to material condition health. Test results (Figure 81-Figure 83) revealed that the data from the controlled sample were stable throughout the loading test. With these pre-requisites at hand, the GWT of GFRP beams during 3-point loading could begin. The destructive testing consisted in loading 1000*40*4.5mm GFRP beams from displacement load of 3 to 12 mm with an increment of 1mm. Guided wave data were collected in three stages: pre, during and post three-point loading tests. The data collected (Figure 84) pre-loading showed that the S_0 , A_0 and SH_0 (SH_{01} and SH_{02}) were detectable, as reported in Chapter 4. The 3-point loading tests were carried out in two stages: the first one consisted in loading the beams from displacement load of 3 to 8mm with an increment of 1mm. The results are shown in Figure 85-Figure 88. The second stage consisted in loading the beams from displacement load of 9 to 12mm with an increment of 1mm. Figure 89-Figure 92 show the overall results from applying a baseline subtraction method to the guided wave data collected pre- and post-loading from displacement load of 3 to 12mm.

The expected failure mode of a GFRP specimen during a 3-point loading is: matrix/fibre breaking followed by several delaminations, then more matrix/fibre breakage and delaminations leading to ultimate failure of the specimen. As reported in the literature, such damage (especially the delamination) will cause a drop in the amplitudes of the S_0 mode, caused by either mode conversion, wave reflection and refraction. It was further reported that delaminations located mid-plane have an impact on the A_0 mode. These results were from experiments conducted in a laboratory environment where defects were designed and inserted in the material. It was observed in the literature that 3-point loading was used to achieve the controlled creation of realistic defects in PMCs samples and so the same approach was used

here, in order to obtain more realistic results. The behaviour of not only the S_0 and A_0 modes were observed here, but also the performance of the SH_{01} and SH_{02} modes during various three-point loading tests. The ultrasonic wave parameters which were monitored during the GWT experiments were the peak-to-peak amplitude of the wave modes detected. Figure 85-Figure 88 revealed that signal amplitudes dropped during the first stage of three-point loading (3-10 mm deflection) and then returned as close as possible to the pre-loading amplitudes. This behaviour was not observed in the control sample therefore, it can be assumed that the ‘Amplitude Drop’ is linked to the condition health of the material. By applying the baseline subtraction method (across all data collected) between peak signal amplitudes recorded at the pre- and the post loading phase, the “Peak Amplitude Drop Over Bending” (Figure 89-Figure 92) demonstrated that S_0 , A_0 and SH_{02} wave modes showed sensitivity to damage but only toward the end life of the material, i.e. from 11 mm displacement, which is when the GFRP beam reached 85% of the maximum bending it could withstand. At 130 kHz, the resolution limit for the S_0 , A_0 and SH_{02} were 10mm, 4.5mm and 6mm respectively. Therefore, defects such as cracks (matrix and fibres) will not be detected as the technique here will not be fit for defects smaller than 4.5mm. The lack of additional amplitude peaks during the loading stage of the material confirmed that no mode conversion had occurred. But this doesn’t mean that delaminations haven’t occurred. But, if delaminations were formed during the displacement load of the material between 3 and 10 mm at least, it is more likely that they were significantly smaller than 4.5mm; the technique here was for a minimum defect size of 4.5mm. The test results here showed that focussing on mode conversion or wave reflection might be the wrong approach when it comes to structural health monitoring. In real life, it will be difficult to find out what defects are being formed during service, therefore it will be difficult to provide qualitative information on the defect itself. Instead of focussing on the specific behaviour of each individual ultrasonic wave mode

interacting with defects, results here showed that it will be enough to focus on signal amplitudes only, as the onset and growth of the defects will be expected to cause changes in the mechanical properties of the composite material; therefore, any wave amplitude will be expected to be affected as wave amplitudes are known to be linked to the mechanical properties of the material. The fact that signal amplitudes dropped and returned as close as possible to the pre-loading amplitudes up to 10 mm deflection might indicate that the GFRP beam was in its elastic deformation state; but when wave amplitudes dropped significantly until failure from the 11 mm deflection, this showed that the material was in its plastic deformation state, which was further confirmed by visual inspection.

6.5 Conclusion

Results have shown that GWT could be used for structural health monitoring of polymer matrix composites. Test results have shown that GWT showed sensitivity to structural issues when the component had reach at least 85% of the maximum force it could withstand. Results also showed that not only the technique was not better than visual inspection but GWT would not give operators enough warning and possible time to react, before imminent failure of the structure.

Chapter 7 CONCLUSION

7.1 Thesis Summary and Conclusion

NDT techniques such as Acoustic Emission, Computed Tomography, Leak Testing, Shearography, Strain Measurement, Thermography, Ultrasound and Visual Inspection are listed as established inspection techniques for composites in the standard ASTM E2533 – 09. This showed that guided wave testing is not recognised yet as a valid NDT technique for composites. Therefore, the main objective of this thesis was to assess guided wave for inspection and structural health monitoring purposes. The focus was on the Glass Fibre Reinforced Polymer (GFRP) material types which are widely used in major industry sectors. For example, the shells from wind turbine blades are made of $\pm 45^\circ$ GFRP panels. Since composites have gradually replaced metals in weight sensitive industry sectors, research work on inspection techniques for this type of material have also increased, including research on guided waves testing of composites. Due to the complexity of wave propagation in composites (caused by the material anisotropic nature), researchers had mostly limited their investigation within a frequency range where the fewest number of wave modes could exist in the material. These were the fundamental Lamb waves (S_0 and A_0). The literature showed that they were various ways these wave modes could be used for the detection of defects such as:

- Delamination (including impact-induced) which was detected by (i) monitoring the amplitude and velocity of the S_0 and A_0 modes from direct transmission, (ii) detecting the A_0 converted from the transmitted S_0 and (iii) monitoring the S_0 retransmitted by the delamination.
- Cracks detected via monitoring the amplitude and velocity of A_0 mode from direct transmission.
- Thermo-oxidative ageing by using reconstruction of elastic moduli through the S_0 and A_0 wave velocities

- And disbond by using leaky nature of the S_0 and A_0 modes.

In this thesis, three transducers were tested against 4.5mm thick $\pm 45^\circ$ GFRP plate, which had similar fibre lay-up with the one used in shell panels from wind turbine blades. These transducers were the Thickness-shear PZT elements, the Teletest Transducer (Thickness-shear PZT elements commercially manufactured within an assembly) and the M2814 Macro Fibre Composite (MFCs) transducers. The goal was to determine their directionality in an $\pm 45^\circ$ GFRP plate and to compare their performance with each other before moving to the inspection of a $[0/90]_{16}$ GFRP laminate and the health monitoring of $\pm 45^\circ$ GFRP beams during three-point loading. Test results showed that three wave modes were detectable in the frequency range 66-130 kHz: the S_0 , A_0 , and the faster and slower wavefront of the SH_0 modes, respectively called SH_{02} , SH_{01} in this thesis and, as reported by Hernandez ^[172]. Results further demonstrated that as long as the transducers were in line with the orientation of the fibres, the S_0 mode was less scattered than the other three wave modes. Therefore, the S_0 mode remained the most suitable ultrasonic wave mode for inspection of these woven GFRP materials. It was also demonstrated that MFC transducers showed stronger signal amplitudes than the Thickness-shear PZT elements and Teletest transducers.

The MFC transducer was then used to detect a 25*15mm piece of paper which was inserted in a GFRP plate. The plate was tested within a frequency range corresponding to the frequency response of the MFC for this specific GFRP plate: 40-80kHz. Results showed that the MFC picked the paper insert but only from the surface closest to the defect, unlike reports in literature where defects such as delaminations were detected from both surfaces of inspection. Results also showed that MFC transducers can be used for inspection purposes and they do not require to be permanently mounted to test composite components.

Guided wave testing was further assessed during the three-point loading tests which were conducted until complete failure of the GFRP beams. Guided wave testing was carried out pre, during and post loading and four ultrasonic waves were detected: the S_0 , SH_{02} , SH_{01} and A_0 wave modes. Test results showed that the amplitudes of the S_0 , SH_{02} and A_0 dropped during loading and reverted back to their pre-loading amplitude once the load was removed. In order to efficiently assess the sensitivity of guided wave against damage occurring during three-point loading, the difference in signal between pre and post loading was plotted. Results showed that at some point through the life of the specimen (85%), the post loading signal amplitude did not return to its pre-loading value but instead, dropped even further until complete failure of the beam. Guided wave testing was sensitive to damage occurring during three-point loading but only toward the end of life of the GFRP beams.

7.2 Contribution to knowledge

The thickness-shear PZT elements and Teletest transducers discussed in this thesis, have never been evaluated against GFRP plates. This is because since 1997, these transducers were exclusively used on metallic structures. This thesis offers for the first time, the directionality plots of the d_{51} Thickness-shear PZT elements when (a) mounted in parallel to the fibre orientation and (b) mounted off fibre direction in a woven $\pm 45^\circ$ GFRP plate. In composite materials, MFC sensors have stronger signal amplitudes than thickness-shear PZT elements and Teletest transducers; therefore, MFCs would be more suitable for inspection purposes because fewer of them would be needed to cover large areas in comparison with the use of thickness-shear PZT elements and Teletest transducers.

Test results reported in this thesis further showed that guided wave testing was sensitive to delamination/inclusion (simulated by a piece of paper) when it was located one-third away from the surface of inspection but not when it was located beyond mid-plane.

The NDT results from the three-point loading experiment showed that guided wave testing, vibrometry testing, and X-rays were inconclusive up to 8 mm deflection (67% of the deflection required to cause ultimate failure). Therefore, these techniques will not be suitable for inspection up to that point. The AE technique detected events consistent with damage events at a deflection of 8 mm but as these occurred during loading, further work is required to demonstrate these were not generated by the bending machine. The Guided wave technique did not detect anything major anomaly until the point where the structure showed irreversible changes (from 11 mm deflection onwards). These results confirm that Guided waves have successfully detected damage before complete failure of the GFRP beam and the results were validated with the Visual Inspection. These results demonstrate that guided wave testing can be used as a warning tool to an imminent failure.

7.3 Future Work

Thickness-shear PZT elements/Teletest transducers directionality in GFRP plates

Directionality plots for the MFC M2814-P1, Thickness-shear PZT elements and Teletest transducers could be plotted against other GFRP plates with different lay-up than the one studied in this thesis (biaxial). The frequency range of interest will be increased to enable study of higher order modes. The new material of interest would be unidirectional and multidirectional laminates. This study will provide a full picture of the directionality of these three transducers in composites, which would aid transducer selection for the inspection of a range of composite applications. These additional tests would be conducted on a large plate (4000 mm long and 4000 mm wide at least) to prevent ultrasonic wave modes from overlapping. It is recommended that the 3D vibrometer should be used as the receiver as this thesis showed that it was an effective receiver for this type study.

Transducer design for Disbond detection in Wind Turbine Blades

It was reported in the literature that the lack of disbond enabled energy leakage from one component to another. This information can be used to monitor the energy flowing from the shell to the spar cap. By placing a transducer array on the shell and spar cap beam, the length and width of the disbond could be measured: the transducers mounted on the shell will allow measuring of the disbond by recorded the amplitudes of the received signals until they stop leaking into the spar cap. By placing transducers across the spar cap, the size of the disbond can be potentially measured by the lack of leakage into spar cap.

Transducer array design for damage detection during fatigue of composite materials

It will also be interesting to repeat to review the three-point loading experiment on a specimen much larger than the one tested in this thesis. This will enable the study and design various transducer arrays to enhanced preferred wave modes and cancel the unwanted ones. A larger sample would require a specifically designed three-point loading test rig to be built. The speed of testing will be reduced to 1 mm/min to promote slower damage growth than the one studied in this thesis.

REFERENCES

1. ASTM-E2533-09, 'Standard Guide for Non-destructive Testing of Polymer Matrix Composites Used in Aerospace Applications'.
2. Karbhari, V.M. (2013). *Non-destructive evaluation (NDE) of polymer matrix composites*. Woodhead Publishing.
3. Russell-Floyd R., Phillips M.G. (1988) 'A critical assessment of acousto-ultrasonics as a method of non-destructive evaluation for carbon-fibre-reinforced thermoplastic laminates', *NDT International*, Volume 21, Number 4, pp.247-257.
4. Guo N., Dia P. (1993), 'Lamb wave propagation in composite laminates and its relationship with acousto-ultrasonics', *NDT & E International*, Volume 26, Number 2, pp.75-84.
5. ASTM-E976-15, 'Standard Guide for Determining the Reproducibility of Acoustic Emission Sensor Response'.
6. Hsu N. N., Breckenridge F. (1981), 'Characterization of acoustic emission sensors', *Materials Evaluation* 39, pp. 60–68.
7. Irving P., Soutis C. (2014). *Polymer composites in the Aerospace Industry*. Woodhead Publishing.
8. Kim H. G., Lee D. G. (2002), 'Dielectric cure monitoring for glass/polyester prepreg composites', *Composite Structures* 57, pp. 91–99.
9. Jol H.M. (2009), *Ground Penetrating Radar: Theory and Applications*. Elsevier Science.
10. U.S Department of Transportation, Federal Aviation Administration, Flight Standards Service, (2008). *Aviation Maintenance Technician Handbook*.
11. U.S Department of Transportation, Federal Aviation Administration, Flight Standards Service, (2012). *Aviation Maintenance Technician Handbook – Airframe*, Volume 1.
12. Cawley P. (1987), 'The sensitivity of the mechanical impedance method of non-destructive testing', *NDT International*, Volume 20, Number 4, pp. 209-215.

13. Bergoglio M., Mari D. (2012), 'Leak rate metrology for the society and industry', *Measurement* 45, pp. 2434-2440.
14. Singh R. (2012), *Applied Welding Engineering: Process, Codes and Standards*. Butterworth-Heinemann.
15. Calcatelli A., Bergoglio M., Mari D. (2007), 'Leak detection, calibrations and reference flows: Practical example', *Vacuum* 81, pp. 1538-1544.
16. Steckelmacher W., Tinsley D.M. (1962), 'Thermal conductivity leak detectors suitable for testing equipment by overpressure or vacuum', *Vacuum*, Volume 12, Issue 5, pp.153-159.
17. Holland S.D., Roberts R., Chimenti D.E., Song J.H. (2006), 'An ultrasonic array sensor for spacecraft leak direction finding', *Ultrasonic* 45, pp.121-126.
18. Hung Y.Y. (1999), 'Applications of digital shearography for testing composite structures', *Composites: Part B* 30, pp.765-773.
19. 'RSflite Composite Solution Overview' retrieved from <https://sonatest.com/products/specialised-products/rsflite>
20. 'Laser Shearography Solution' retrieved from <https://www.dantecdynamics.com/solutions-applications/solutions/laser-shearography-ndt/>
21. 'In-Service Testing of Aircrafts' retrieved from <https://www.automationtechnology.de/cms/en/in-service-testing-of-aircrafts-ntms-boeing-airbus/>
22. 'Thermal Wave Imaging Applications' retrieved from <https://www.thermalwave.com/applications/>
23. 'MoviTHERM Composite Check Solution' retrieved from <https://movitherm.com/solutions/non-destructive-testing/composite-check/>
24. 'Curlin Air System' retrieved from <https://www.ndtstystems.com/curlin-air>

25. 'Hydrastar Robotic Inspection System' retrieved from <https://www.industrial.ai/inspection-technologies/automated-ut-systems/composite-inspection/krautkramer-hydrastar>
26. 'Instruments for ultrasonic inspection of aerospace components' retrieved from <https://www.innerspec.com/en-gb/integrated/applications/volumetric-inspection/composites-and-forgings/>
27. 'Nondestructive Bond Testing for Aircraft Composites' retrieved from <https://www.olympus-ims.com/en/applications/non-destructive-bond-testing-aircraft-composites/>
28. 'BondHub II' retrieved from <https://www.ndt-systems.com/bond-testing-cscan>
29. 'Bondascope 3100' retrieved from <https://www.ndt-systems.com/bondascope-3100>
30. 'Non-destructive inspection for FRP and composite assets' retrieved from <https://utcomp.com/inspection-for-frp-composite-assets/>
31. 'Thickness Measurement of Aerospace Composites' retrieved from <https://www.olympus-ims.com/en/applications/aerospace-composites/>
32. 'EddyFi Technologies for Composite Defect Inspection Applications' retrieved from <https://eddyfi.com/en/application/composite-defects>
33. Drury J. C. (November 2004), 'NDT fundamentals - Ultrasonics – Part 12. Fundamentals of ultrasonic phased arrays', *Insight*, Vol. 46, no 11, pp.650-652.
34. 'Guided Wave Pipeline Inspection System' retrieved from <https://eddyfi.com/en/product/focus>
35. Schwartz M. M. (1983), *Composite Materials Handbook*. McGraw Hill Higher Education
36. Hull D. (1981), *An Introduction to Composite materials*. Cambridge University Press.
37. Daniel I. M., Ishai O. (2006), *Engineering Mechanics of Composite Materials*. Oxford University Press

38. Wang R., Zheng S., Zheng Y. (2011), *Polymer matrix composites and technology*. Woodhead Publishing.
39. 'Composite Glossary' retrieved from <http://www.netcomposites.com/glossary>
40. Tenney D. R., Davis J. G., Pipes R. B., Johnston N. (2009), 'NASA Composite Materials Development: Lessons Learned and Future Challenges'.
41. Drury J. C. (November 2004), 'NDT fundamentals - Ultrasonics – Part 1. Basic principles of sound', *Insight*, Vol. 46, no 11, pp.650-652.
42. Rose J. (1999), *Ultrasonic waves in solid media*. Cambridge University Press.
43. Haig A. G., Mudge P., Balachandran W. (2008), 'Advanced transducer development for long range ultrasonic inspection systems', *Proceedings of the 2008 Conference for the Engineering Doctorate in Environmental Technology*.
44. Zhang L., Mudge P., Amira A., Balachandran W. (2012), 'Improved performance of Guided Wave Ultrasonic Testing for long range inspection of pipelines using multi-channel systems', *Proceedings of the 3rd gas Processing Symposium*, pp 249-256.
45. Lowe M.J.S., Alleyne D.N., Cawley P. (1998), 'Defect detection in pipes using guided waves', *Ultrasonic* 36, pp. 147-154.
46. Liu Z., Zhao J., Wu B., Zhang Y., He C. (2010), 'Configuration optimization of magnetostrictive transducers for longitudinal guided wave inspection in seven-wire steel strands', *NDT&E International* 43, pp.484-492.
47. Raisutis R., Kazys R., Mazeika L., Zukauskas E., Samaitis V., Jankauskas A. (2014), 'Ultrasonic guided wave-based testing technique for inspection of multi-wire rope structures', *NDT&E International* 62, pp. 40–49.
48. Wilcox P., Evans M., Pavlakovic B., Alleyne D., Vine K., Cawley P., Lowe M. (June 2003), 'Guided wave testing of rail', *Insight Vol 45*, No 6, pp.413-420.

49. Rose J. L., Avioli M.J., Mudge P., Sanderson R. (2004), 'Guided wave inspection potential of defects in rail', *NDT&E International* 37, pp. 153–161.
50. Plant Integrity LRUT Level 1 course, Section 2 (2010), *Introduction to Ultrasonic Guided Waves*, pp. 8.
51. Birt E. A. (May 1998), 'Damage detection in carbon-fibre composites using ultrasonic Lamb waves', *Insight Vol. 40*, pp.335-339.
52. Lu Y., Ye L., Su Z., Yang C. (2008), 'Quantitative assessment of through thickness crack size based on Lamb wave scattering in aluminium plates', *NDT&E international* 41, Issue 1, pp. 59-68.
53. 'Disperse Program information' retrieved from <https://www.imperial.ac.uk/non-destructive-evaluation/products-and-services/disperse/>
54. Pol C. B., Banerjee S. (2013), 'Modeling and analysis of propagating guided wave mode in laminated composite plate subject to transient surface excitations', *Wave Motion* 50, pp. 964-978.
55. Wilcox P., Lowe M., Cawley P. (2001), 'The effects of dispersion on long-range inspection using ultrasonic guided waves', *NDT&E international* 34, pp. 1-9.
56. Bird J. O., May A. J. C. (1994), *Mathematics for Electrical Technicians*, p.361. Taylor & Francis.
57. Lee J. (1999), 'Plate waves in multi-directional composite laminates', *Composite Structures* 46, pp. 289-297.
58. 'Wavemaker Specifications' retrieved from <https://www.guided-ultrasonics.com/wavemaker/>
59. 'MsS guided wave system' retrieved from <http://www.gwanalysis.com/mss.html>
60. 'UltraWave LRT System' retrieved from <https://www.olympus-ims.com/en/ultrawave-lrt/>

61. Rhee S., Lee J. K., Lee J. J. (August 2007), 'The group velocity variation of lamb wave in fibre reinforced composite plate', *Ultrasonics* 47, pp.55-63.
62. Percival W J, Birt E A (1997), "A study of Lamb wave propagation in carbon-fibre composites", *INSIGHT Vol 39*, No 10, pp. 728-735.
63. Wang L., Yuan F. G. (2007), 'Group velocity and characteristic wave curve of Lamb waves in Composites: Modelling and experiment', *Composites Science and Technology* 67, pp. 1370–1384.
64. Kudela P., Zak A., Krawczuk M., Ostachowicz W. (2007), 'Modelling of wave propagation in composite plates using the time domain spectral element method', *Journal of Sound and Vibration* 302, pp. 728–745.
65. APC International Ltd (2011), *Piezoelectric ceramics, principles and applications, second edition*. APC International, Ltd.
66. Zagzebski James A. (1996), *Essentials of Ultrasound Physics*. Elsevier-Health Sciences Division.
67. J. Van Randerat, R. E. Settrington (1974), *Piezoelectric Ceramics*. Mullard Publication.
68. 'Hysteresis Loop Information' retrieved from <https://www.nded.org/EducationResources/CommunityCollege/MagParticle/Physics/HysteresisLoop.htm>
69. Blomme E., Bulcaen D., Declercq F., October 2002, 'Air-coupled ultrasonic NDE: experiments in the frequency range 750 kHz–2 MHz', *NDT & E International*, Volume 35, Issue 7, Pages 417-426.
70. Akbari-Mousavia S. A. A., Barrett L. M., Al-Hassanib S. T. S. 20 June 2008, 'Explosive welding of metal plates', *Journal of Materials Processing Technology*, Volume 202, Issues 1–3, Pages 224-239.

71. Mountassir L., Bassidi T., Nounah H., (2019) ‘Experimental study of the corrosion effect on the elastic properties of steel plates by ultrasonic method’, *Physica B: Condensed Matter* 557, pp. 34–44.
72. Khalili P., Cawley P., (2018) ‘The choice of ultrasonic inspection method for the detection of corrosion at inaccessible locations’, *NDT and E International* 99, pp. 80–92.
73. Caleyó F., Alfonso L, Espina-Hernandez J H and Hallen J M (2007), ‘Criteria for performance assessment and calibration of in-line inspections of oil and gas pipeline’, *Meas. Sci. Technol.* 18, pp. 1787–1799.
74. Barbian A., Beller M., Hartmann S., Schneider U. (2011), ‘High Resolution Ultrasonic In-Line Inspection: Added Value and Special Applications’, *6th Pipeline Technology Conference 2011*
75. Uzelac Neb I., Reber K., Belter M., Barbian O. A. (2003), ‘Ultrasonic In-Line Inspection of Pipelines, New Generation of Tools’, *Rio Pipeline Conference Exposition 2003*, held in October, 22-24, Brazil, Rio de Janeiro
76. Lalithakumari S., Pandian R. (2019), ‘Pre processing of ultrasonic signals austenitic stainless steel weld at high temperature’, *Materials Today: Proceeding* (2019).
77. Kurashkin K., Mishakin V., Rudenko A. (2019), ‘Ultrasonic Evaluation of Residual Stresses in Welded Joints of Hydroelectric Unit Rotor Frame’, *Materials Today: Proceedings* 11, pp. 163–168.
78. Tabatabaeipour M., Hettler J., Delrue S. and Van Den Abeele K. (2015), ‘Nondestructive Ultrasonic Inspection of Friction Stir Welds’, *Physics Procedia* 70, pp. 660 – 663.
79. Tabatabaeipour S.M., Honarvar F. (2010), ‘A comparative evaluation of ultrasonic testing of AISI 316L welds made by shielded metal arc welding and gas tungsten arc welding processes’, *Journal of Materials Processing Technology* 210, pp. 1043–1050.

80. Chassignole B., El Guerjouma R., Ploix M.-A., Fouquet T. (2010), ‘Ultrasonic and structural characterization of anisotropic austenitic stainless-steel welds: Towards a higher reliability in ultrasonic non-destructive testing’, *NDT&E International* 43, pp. 273–282
81. Shakibi B., Honarvar F., Moles M.D.C., Caldwell J., Sinclair A. N. (2012), ‘Resolution enhancement of ultrasonic defect signals for crack sizing’, *NDT&E International* 52, pp. 37–50
82. Lin X., Chen G., Li J., Lu F., Huang S., Cheng X. (2018), ‘Investigation of acoustic emission source localization performance on the plate structure using piezoelectric fiber composites’, *Sensors and Actuators A* 282, pp. 9–16.
83. Pascoe J.A., Zarouchas D.S., Alderliesten R.C., Benedictus R. (2018), ‘Using acoustic emission to understand fatigue crack growth within a single load cycle’, *Engineering Fracture Mechanics* 194, pp. 281–300
84. D’Angela D., Ercolino M. (2019), ‘Acoustic Emission Entropy as a fracture-sensitive feature for realtime assessment of metal plates under fatigue loading’, *Procedia Structural Integrity* 18, pp. 570–576.
85. Maleki A., Saeedifar M., Najafabadi M. A., Zarouchas D. (2019), ‘The fatigue failure study of repaired aluminum plates by composite patches using Acoustic Emission’, *Engineering Fracture Mechanics* 210, pp. 300–311.
86. Owen J., Ducker E., Huggan M., Ramsey C., Neville A., Barker R. (2019), ‘Design of an elbow for integrated gravimetric, electrochemical and acoustic emission measurements in erosion-corrosion pipe flow environments’, *Wear* 428–429, pp.76–84
87. Li S., Song Y., Zhou G. (2018), ‘Leak detection of water distribution pipeline subject to failure of socket joint based on acoustic emission and pattern recognition’, *Measurement* 115, pp. 39–44.

88. Leuker W., Jax P., Streicher V. (1988), 'Verification of Erosive Leakage of In-bed Heat Exchange Surfaces in a Fluidized Bed Combustion Plant by Means of Acoustic Emission', *Non-Destructive Testing*, Pages 3033-3041.
89. Han Y., Zhang S., Zheng S., Zhu W., Zhang B. (2006), 'Failure analysis and acoustic emission tests of an in-service waste heat boiler', *Engineering Failure Analysis 13*, pp.683–697.
90. Wang K., Zhang X., Hao Q., Wang Y., Shen Y. (2019), 'Application of improved least-square generative adversarial networks for rail crack detection by AE technique', *Neurocomputing 332*, pp. 236–248.
91. Zhang X., Hao Q., Wang K., Wang Y., Shen Y., Hu H. (2018), 'An investigation on acoustic emission detection of rail crack in actual application by chaos theory with improved feature detection method', *Journal of Sound and Vibration 436*, pp.165-182.
92. Hao Q., Zhang X., Wang K., Shen Y., Wang Y. (2018), 'A signal-adapted wavelet design method for acoustic emission signals of rail cracks', *Applied Acoustics 139*, pp. 251–258
93. Zhang X, Zou Z., Wang K., Hao Q., Wang Y., Shen Y., Hu H. (2018), 'A new rail crack detection method using LSTM network for actual application based on AE technology', *Applied Acoustics 142*, pp.78–86.
94. Zhang X., Cui Y., Wang Y., Sun M., Hu H. (2018), 'An improved AE detection method of rail defect based on multi-level ANC with VSS-LMS', *Mechanical Systems and Signal Processing 99*, pp. 420–433.
95. QIU L., YAN X., LIN X., YUAN S. May 2019, 'Multiphysics simulation method of lamb wave propagation with piezoelectric transducers under load condition', *Chinese Journal of Aeronautics*, Volume 32, Issue 5, Pages 1071-1086.

96. Mohabuth M., Kotousov A., Ng C. T. and Rose L. R. F. (2018), 'Implication of changing loading conditions on structural health monitoring utilising guided waves', *Smart Materials and Structures*, Volume 27, Number 2.
97. Cho H., Hasanian M., Shana S., Lissenden C. J. (2019), 'Nonlinear guided wave technique for localized damage detection in plates with surface-bonded sensors to receive Lamb waves generated by shear horizontal wave mixing', *NDT and E International* 102, pp. 35–46.
98. Yeung C., Ng C. T. (2019), 'Time-domain spectral finite element method for analysis of torsional guided waves scattering and mode conversion by cracks in pipes', *Mechanical Systems and Signal Processing* 128, pp. 305–317.
99. Niu X., Duan W., Chen H., Marques H.R. (2019), 'Excitation and propagation of torsional T(0,1) mode for guided wave testing of pipeline integrity', X. Niu et al. / *Measurement* 131, pp. 341–348.
100. Duana W., Kanfoud J., Deere M, Mudge P., Gan T. H. (2018), '***Spectral subtraction and enhancement for torsional waves propagating in coated pipes***', *NDT and E International* 100, pp. 55–63.
101. Kirby R, Zlatev Z, Mudge P. (2012), 'On the scattering of torsional elastic waves from axisymmetric defects in coated pipes', *J Sound Vib* 2012;331, pp. 3989–4004.
102. Kirby R, Zlatev Z, Mudge P. (2013), 'On the scattering of longitudinal elastic waves from axisymmetric defects in coated pipes', *J Sound Vib* 2013;332, pp. 5040–5058.
103. Løvstad A., Cawley P. (2011), 'The reflection of the fundamental torsional guided wave from multiple circular holes in pipes', *NDT&E International* 44, pp. 553–562
104. Carandente R., Cawley P. March 2012, 'The effect of complex defect profiles on the reflection of the fundamental torsional mode in pipes', *NDT & E International*, Volume 46, Pages 41-47.

105. Setareh M., Saffar-Avval M., Abdullah A. (2019), 'Experimental and numerical study on heat transfer enhancement using ultrasonic vibration in a double-pipe heat exchanger', *Applied Thermal Engineering* 159, 113867
106. Evans M., Lucas A., Ingram I. (2018), 'The inspection of level crossing rails using guided waves', *Construction and Building Materials* 179, pp. 614–618.
107. Ramatlo D. A., Wilke D. N., Loveday P. W. (2018), 'Development of an optimal piezoelectric transducer to excite guided waves in a rail web', *NDT and E International* 95, pp.72–81.
108. Narayanan M.M., Kumar A., Thirunavukkarasu S., Mukhopadhyay C.K. (2019), 'Development of ultrasonic guided wave inspection methodology for steam generator tubes of prototype fast breeder reactor', *Ultrasonics* 93, pp. 112–121.
109. Rose J. L., Ditri J. J., Pilarski A., Rajana K. and Carr F. (1994), 'A guided wave inspection technique for nuclear steam generator tubing', *NDT& E International*, Volume 27, Number 6.
110. Baltazar A., Hernandez-Salazar C. D., Manzanares-Martinez B. (2010), 'Study of wave propagation in a multiwire cable to determine structural damage', *NDT&E International* 43, pp. 726–732
111. Zhang P., Tang Z., Lv F. and Yang K. (2019), 'Numerical and Experimental Investigation of Guided Wave Propagation in a Multi-Wire Cable', *Appl. Sci.*, 9, 1028.
112. Malo Peces S., Livadas M., Selcuk C., Gan T.-H., and Mares C. (2016), "Wave Scattering Analysis in an ACSR Cable Using Piezoelectric Transducers", *EWSHM-8th European Workshop on Structural Health Monitoring*, 2016.

113. Malo S., Livadas M., Tan S.-M., Kanfoud J., Gan T.-H., Mares C. (2018), ‘Long Range Guided Wave Propagation Experimental Analysis in Overhead Power Line Cables under Different Axial Load Levels’, *Modern Practice in Stress and Vibration Analysis (MPSVA)*.
114. Liu M., Zeng Z., Xu H., Liao Y., Zhou L., Zhang Z., Su Z. (2017), ‘Applications of a nanocomposite-inspired in-situ broadband ultrasonic sensor to acousto-ultrasonics-based passive and active structural health monitoring’, *Ultrasonics* 78, pp. 166–174.
115. Chrysochoidis N. A., Assimakopoulou T. T. and Saravanos D. A. (2015), ‘Nonlinear wave structural health monitoring method using an active nonlinear piezoceramic sensor for matrix cracking detection in composites’, *Journal of Intelligent Material Systems and Structures*, Vol. 26(15), pp. 2108–2120.
116. Wilson C. L. and Chang F. K. (2016), ‘Monitoring fatigue-induced transverse matrix cracks in laminated composites using built-in acousto-ultrasonic techniques’, *Structural Health Monitoring*, Vol. 15(3), pp. 335–350.
117. Barile C., Casavola C., Pappalettera G., Vimalathithan P. K. (2019), ‘Acousto-ultrasonic evaluation of interlaminar strength on CFRP laminates’, *Composite Structures* 208, pp. 796–805.
118. Memmolo V., Park Y.J., Lilov M., Monaco E., Ricci F. (2018), ‘Preliminary acousto-ultrasonic investigation for multi-parameter transducer self-diagnostic system in composites’, *Composite Structures* 202, pp. 1229–1238.
119. Smithard J., Norman P., Van Der Velden S., Powlesland I., Jung G., Rajic N. and Galea S. (2017), ‘The Acousto Ultrasonic Structural health monitoring Array Modulen (AUSAM+) for Damage Detection in Structures’, *Procedia Engineering* 188, pp. 448 – 455

120. Michaels J. E. (2016), '9: Sparse array imaging with guided waves under variable environmental conditions, Structural Health Monitoring (SHM) in Aerospace Structures', Pages 255-284.
121. Clarke T., Simonetti F., Cawley P. (2010), 'Guided wave health monitoring of complex structures by sparse array systems: Influence of temperature changes on performance', *Journal of Sound and Vibration* 329, pp. 2306–2322
122. Croxford A. J., Moll J., Wilcox P. D., Michaels J. E. (2010), 'Efficient temperature compensation strategies for guided wave structural health monitoring', *Ultrasonics* 50, pp. 517–528.
123. Putkis O., Dalton R.P., Croxford (2015) A.J., 'The influence of temperature variations on ultrasonic guided waves in anisotropic CFRP plates', *Ultrasonics* 60, pp 109–116.
124. Chen X., Michaels J. E., Lee S. J., Michaels T. E. (2012), 'Load-differential imaging for detection and localization of fatigue cracks using Lamb waves', *NDT&E International* 51, pp.142–149.
125. Yu L., Tian Z. (2015), 'Case study of guided wave propagation in a one-side water-immersed steel plate', *Case Studies in Non Destructive Testing and Evaluation* 3, pp. 1–8.
126. Moll J., Fritzen C.-P. (2012), 'Guided waves for autonomous online identification of structural defects under ambient temperature variations', *Journal of Sound and Vibration* 331, pp. 4587–4597.
127. El Mountassir M., Mourot G., Yaacoubi S., Maquin D. (2018), 'Damage detection and localisation in pipeline using sparse estimation of ultrasonic guided waves signals', *IFAC*, Pages 941-948.

128. McKeon P., Yaacoubi S., Declercq N. F., Ramadan S., Yaacoubi W. K. (2014), 'Baseline subtraction technique in the frequency–wavenumber domain for high sensitivity damage detection', *Ultrasonics* 54, pp. 592–603.
129. Tan K. S., Guo N., Wong B. S. (1995), 'Experimental evaluation of delamination in composite plates by the use of Lamb waves', *Composites Science and Technology* 53, pp. 77-84.
130. Tan K. S., Guo N., Wong B. S. and Tui C. G. (1995), "Comparison of Lamb waves and pulse echo in detection of near-surface defects in laminate plates", *NDT&E International*, Vol 28, No.4, pp. 215-223.
131. Toyama N., Takatsubo J. (2004), 'Lamb wave method for quick inspection of impact-induced delamination in composite laminates', *Composites Science and Technology* 64, pp. 1293-1300.
132. Yan G., Lu X. and Tang J. (2019), 'Guided Wave-Based Monitoring of Evolution of Fatigue Damage in Glass Fiber/Epoxy Composites', *Appl. Sci.*, 9, 1394.
133. Guo N., Cawley P. (1993), 'Lamb wave propagation in composite laminates and its relationship with acousto-ultrasonics', *NDT & E International*, Volume 26, Number 2, pp.75-84.
134. Staszewski W.J., Mahzan S., Traynor R. (2009), "Health monitoring of aerospace composite structures – Active and passive approach", *Composites Science and Technology* 69, pp.1678–1685.
135. Feng B., Ribeiro A. L., Ramos H. G. (2018), 'Interaction of Lamb waves with the edges of a delamination in CFRP composites and a reference-free localization method for delamination', *Measurement* 122, pp. 424–431.

136. Zhao G., Wang B., Wang T., Hao W., Luo Y. (2019), ‘Detection and monitoring of delamination in composite laminates using ultrasonic guided wave’, *Composite Structures* 225, 111161.
137. Kudela P., Radzienski M., Ostachowicz W. (2018), ‘Impact induced damage assessment by means of Lamb wave image processing’, *Mechanical Systems and Signal Processing* 102, pp. 23–36.
138. Wandowski T., Kudela P., Ostachowicz W.M. (2019), ‘Numerical analysis of elastic wave mode conversion on discontinuities’, *Composite Structures* 215, pp. 317–330.
139. Wandowski T., Kudela P., Malinowski P. and Ostachowicz W. (2019) "Guided wave mode conversion phenomenon in composite materials: numerical and experimental study", *Proc. SPIE 10972*, Health Monitoring of Structural and Biological Systems XIII, 109720N (1 April 2019);
140. Su Z., Yang C., Pan N., Ye L., Zhou L.-M. (2007), “Assessment of delamination in composite beams using shear horizontal (SH) wave mode”, *Composites Science and Technology* 67, pp.244–251.
141. Okabe Y., Fujibayashi K., Shimazaki M., Soejima h. and Ogisu T. , Published 24 September 2010, “Delamination detection in composite laminates using dispersion change based on mode conversion of Lamb waves”, IOP Publishing Ltd, *Smart Materials and Structures*, Volume 19, Number 11.
142. Hu N., Shimomukai T., Yan C., Fukunaga H. (2008), “Identification of delamination position in cross-ply laminated composite beams using S_0 Lamb mode”, *Composites Science and Technology* 68, pp.1548–1554.
143. Hu N. (2012), *Composites and their applications*. InTech

144. Munian R. K., Mahapatra D. R., Gopalakrishnan S. (2018), 'Lamb wave interaction with composite delamination', *Composite Structures* 206, pp. 484–498.
145. Gupta S., Rajagopal P. (2018), 'Effect of ply orientation and through-thickness position of delamination on the reflection of fundamental symmetric S0 Lamb mode in GFRP composite plate structures', *Ultrasonics* 90, pp.109–119.
146. Apalowo R.K., Chronopoulos D., Cantero-Chinchilla S. (2019), 'Wave interaction with nonlinear damage and generation of harmonics in composite structures', *Composite Structures* 230, 111495.
147. Ramadas C., Balasubramaniam K., Joshi M., Krishnamurthy C.V. (2011), 'Characterisation of rectangular type delaminations in composite laminates through B- and D-scan generated using Lamb waves', *NDT&E International* 44, pp.281-289.
148. Moreno E., Galarza N., Rubio B., Otero J. A. (2015), "Phase velocity method for guided wave measurements in composite plates", *Physics Procedia* 63, pp. 54-60.
149. Chiua W.K., Roseb L.R.F., Nadarajaha N. (2017), "Scattering of the fundamental anti-symmetric Lamb wave by a midplane edge delamination in a fiber-composite laminate", *Procedia Engineering* 188, pp.317 – 324.
150. Wang D., Ye L., Tang Y., Luc Y. (2012), "Monitoring of delamination onset and growth during Mode I and Mode II interlaminar fracture tests using guided waves", *Composites Science and Technology* 72, pp.145–151.
151. Memmolo V., Monaco E., Boffa N.D., Maio L., Ricci F. (2018), 'Guided wave propagation and scattering for structural health monitoring of stiffened composites', *Composite Structures* 184, pp. 568–580.
152. Munian R. K., Mahapatra D. R., Gopalakrishnan S. (2018), 'Lamb wave interaction with composite delamination', *Composite Structures* 206, pp. 484–498.

153. Shoja S., Berbyuk V., Boström A. (2018), ‘Delamination detection in composite laminates using low frequency guided waves: Numerical simulations’, *Composite Structures* 203, pp. 826–834.
154. Michalcová L. (2018), ‘Delamination growth analysis in mode I by means of Lamb waves’, *Materials Today: Proceedings* 5, pp. 26470–26475.
155. Panda R. S., Rajagopal P., Balasubramaniam K. (2018), ‘Rapid guided wave inspection of complex stiffened composite structural components using non-contact air-coupled ultrasound’, *Composite Structures* 206, pp. 247–260.
156. Rheinfurth M., Kosmann N., Sauer D., Busse G., Schulte K. (2012), “Lamb waves for non-contact fatigue state evaluation of composites under various mechanical loading conditions”, *Composites: Part A* 43, pp.1203–1211.
157. Sohn H., Dutta D., Yang J.Y., Park H.J., DeSimio M., Olson S., Swenson E. (2011), “Delamination detection in composites through guided wave field image processing”, *Composites Science and Technology* 71, pp. 1250–1256.
158. Gelebart Y., Duflo H., Duclos J. (2007), “Air coupled Lamb waves evaluation of the long-term thermo-oxidative ageing of carbon-epoxy plates”, *NDT&E International* 40, pp. 29–34.
159. Vishnuvardhan J., Muralidharan A., Krishnamurthy C.V., Balasubramaniam K. (2009), “Structural health monitoring of anisotropic plates using ultrasonic guided wave STMR array patches”, *NDT&E International* 42, pp. 193–198
160. Qing-Tian D., Zhi-chun Y. (2011), “Propagation of guided waves in bonded composite structures with tapered adhesive layer”, *Applied Mathematical Modelling* 35, pp.5369–5381.

161. Mustapha S., Ye L. (2014), “Leaky and non-leaky behaviours of guided waves in CF/EP sandwich structures”, *Wave Motion* 51, pp.905–918.
162. Habib F., Martinez M., Artemev A., Brothers M. (2013), “Structural health monitoring of bonded composite repairs – A critical comparison between ultrasonic Lamb wave approach and surface mounted crack sensor approach”, *Composites: Part B*, pp. 26–34 47.
163. Alleyne D., Cawley P. (1991), ‘A two-dimensional Fourier transform method for the measurement of propagating multimode signals’, *The Journal of the Acoustical Society of America* 89, 1159.
164. Apetre N., Ruzzena M. (2012), ‘Spectral and perturbation analysis for ultrasonic guided waves’, *Journal of Sound and Vibration*, Vol.331(24), pp.5358-5369.
165. Cunfu H., Hongye L., Zenghua L., Bin W. (2013), ‘The propagation of coupled Lamb waves in multi-layered arbitrary anisotropic composite laminates’, *Journal of Sound and Vibration* 332, pp. 7243–7256.
166. Masmoudi M., Castaings M. (2012), ‘Three-dimensional hybrid model for predicting air-coupled generation of guided waves in composite material plates’, *Ultrasonics* 52, pp. 81–92.
167. Delrue S., Abeelee K.V.D. (2012), ‘Three-dimensional finite element simulation of closed delaminations in composite materials’, *Ultrasonics* 52, pp. 315–324.
168. Barouni A.K., Saravanos D.A. (July 2012), ‘A semi-analytical layerwise wave propagation model for composite strips with piezoelectric actuators and sensors and capabilities of damage detection’, *6th European workshop on Structural Health Monitoring and 1st European Conference of the Prognostic and Health Management (PHM) society*.
169. Haig A G , Sanderson R M, Mudge P J, Balachandran W. (February 2013), ‘Macro-fibre composite actuators for the transduction of Lamb and horizontal shear ultrasonic

- guided waves', *Insight - Non-Destructive Testing and Condition Monitoring*, Volume 55, Number 2.
170. 'MFC P1 type' retrieved from <https://www.smart-material.com/MFC-product-P1.html>
171. 'MFC P2 type' retrieved from <https://www.smart-material.com/MFC-product-P2.html>
172. B. Hernandez-Crespo (2019), *Characterisation and Exploitation of Ultrasonic Guided Wave Modes for Structural Health Monitoring of Glass-Fibre-Reinforced-Polymer Structures*, PhD thesis.
173. <https://www.polytec.com/uk/>
174. J. Tang (2019), *Characterization of fatigue damage types in fibre reinforced composites utilizing pattern recognition techniques applied to acoustic emission signals*, PhD thesis.

APPENDIX

Appendix A – Polytec Scanning Vibrometer Instruction

The protocol for using the scanning vibrometer is as follows:

1. Before proceeding with any set-up, the operator needs to ensure that all test parameters potentially saved by a previous operator, are cleared. When this is complete, the operator can now upload the Vibrometer default settings.
2. Interferometry requires that the distance between the PSV-3D-400-M and the sample's surface is $0.99 \text{ meters} + n * 0.204 \text{ meters}$ where n is a positive integer. In order to determine these distances, the Top Laser Head must be (i) set to "Centre Beam" (**Figure 99**), (ii) as straight as possible and (iii) pointing toward the centre of the testing area.

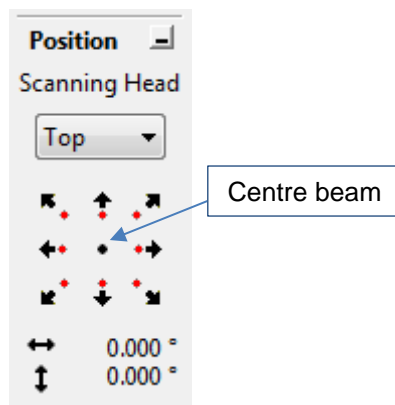


Figure 99 Setting Laser to Centre Beam

By clicking on "Geometry Point" from the "Scan" drop down menu, the vibrometer will then return its distance from the sample.

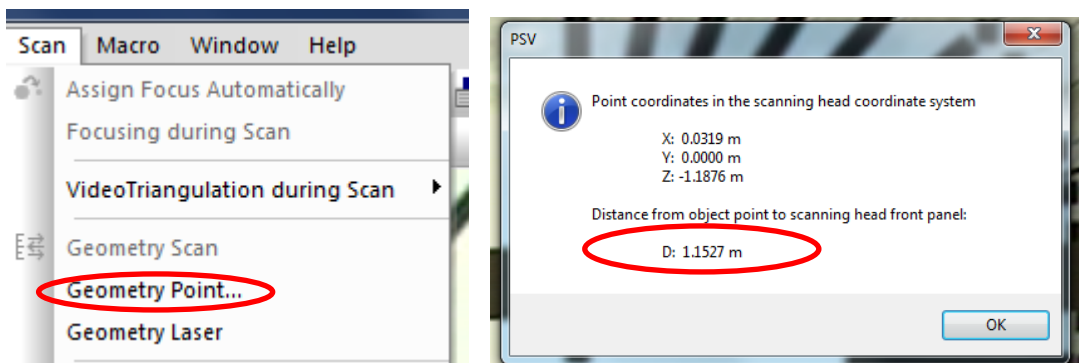
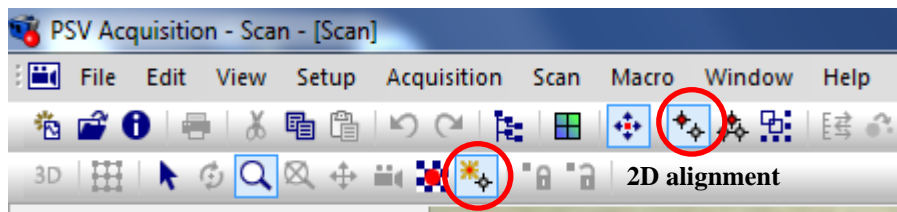


Figure 100 Geometry Scan Point

3. When the Top Laser head is set, the remaining two cameras (left and right) can be aligned. Like the Top Laser, the left and right must be as straight as possible and facing the area to be scanned. Ideally, the three cameras should form an equilateral triangle but if this cannot be achieved, the distances between them should remain as close as possible. The operator should ensure that the left/right laser are set to “Centre Beam”.
4. The next stage consists in carrying a 2D alignment for each laser. The goal is to select as many points as possible within the area to be tested. This is to ensure that the laser heads are always pointing and scanning the direction/point intended. Before starting the selection of points, the operator must select the 2D alignment automatic option.



“Auto” option

Figure 101 2D alignment step

5. The 3D alignment operation can start as soon as the 2D alignment is completed for each laser. This task consists in assigning coordinates to the inspection area. At least five points must be selected: the first point will be the origin; the second will represent a point on the x-axis; the third one allows to create the x-y axis and the last two will be arbitrary. It is recommended to set the operation to the “Auto” and to set each laser to “Auto Focus” before carrying out the task. The operator must ensure that the three lasers overlay as much as possible at each of these points. For health and safety reasons, the operator should always wear safety goggles when working near the lasers.

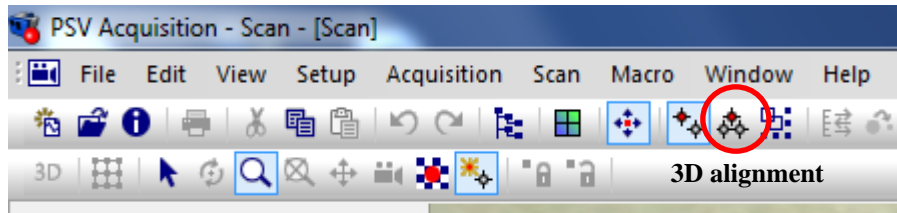


Figure 102 3D alignment step

The quality of the 3D alignment is evaluated by a set “Target”. The smallest the number is, the best the quality of the results.

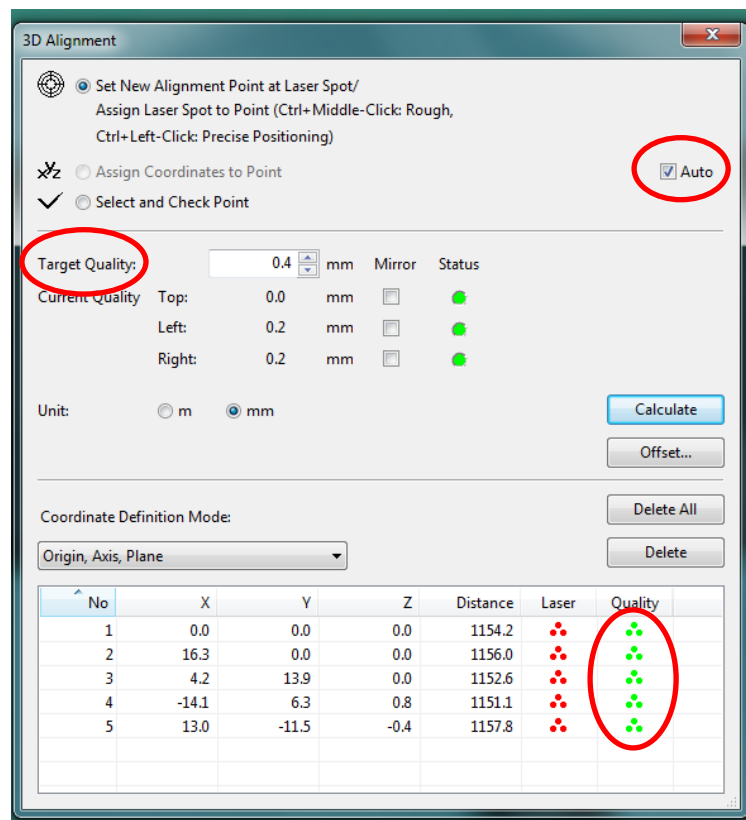


Figure 103 3D alignment Target Quality

- When the 2D/3D alignments have been successfully achieved, the operator can now move to defining the scan areas/points for data collection. As soon as this is complete, the “Geometry Scan” - which assesses the quality of the areas/points targeted for scanning - can be launched.

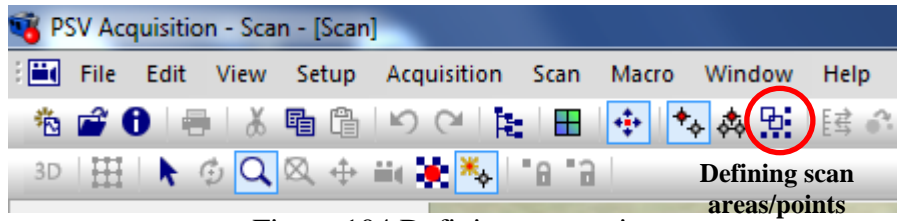
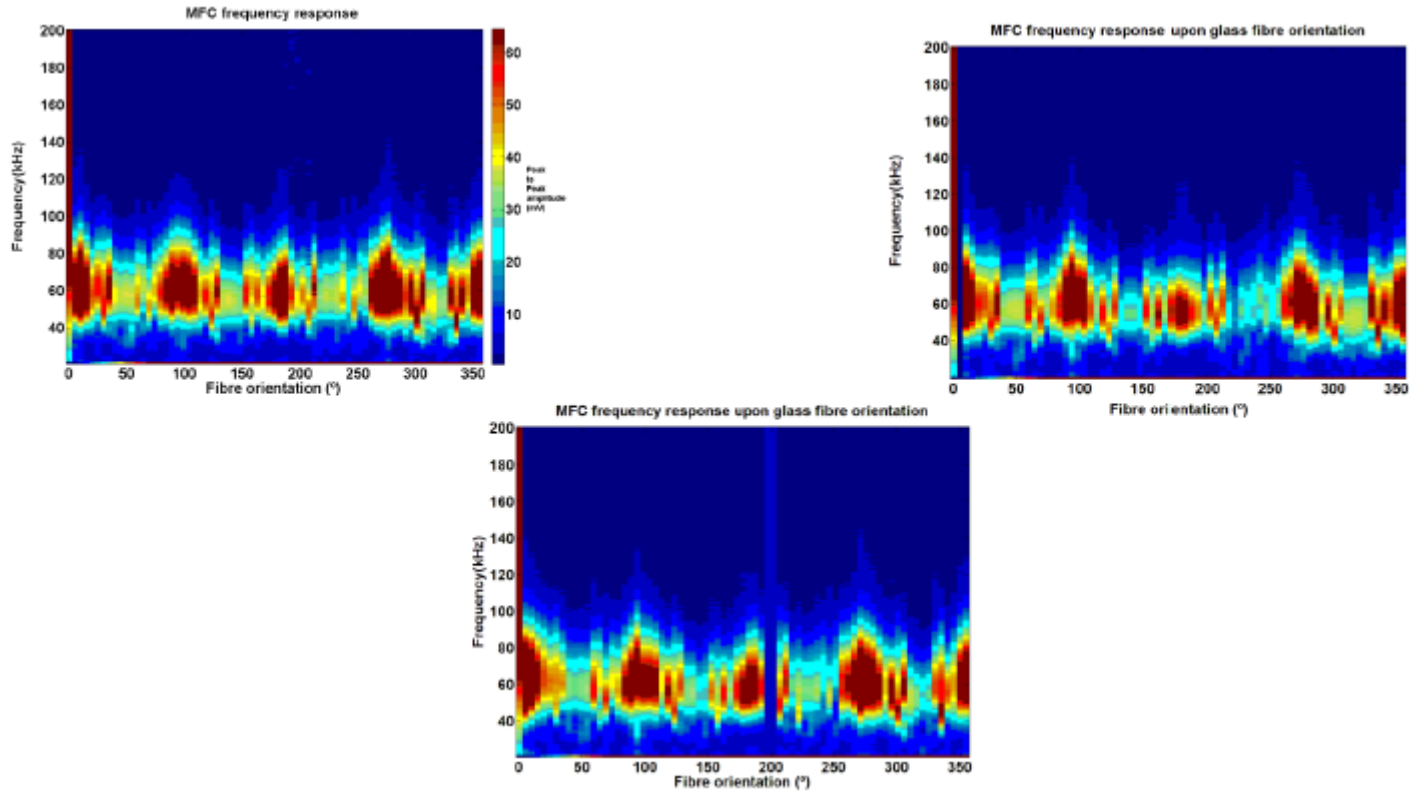


Figure 104 Defining scan points

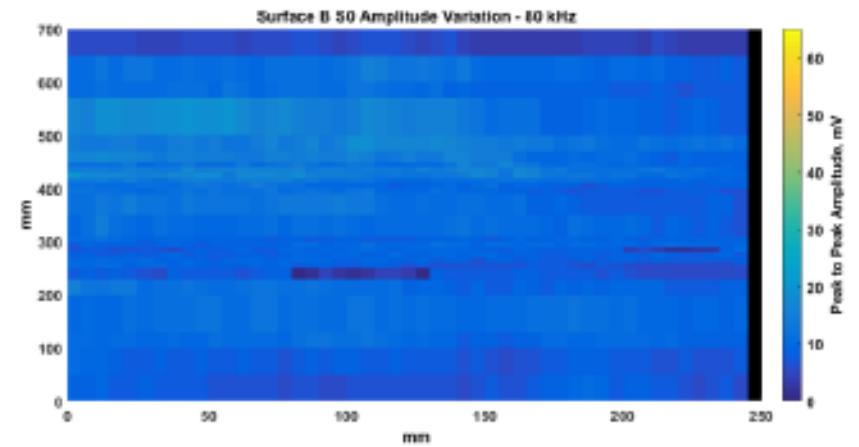
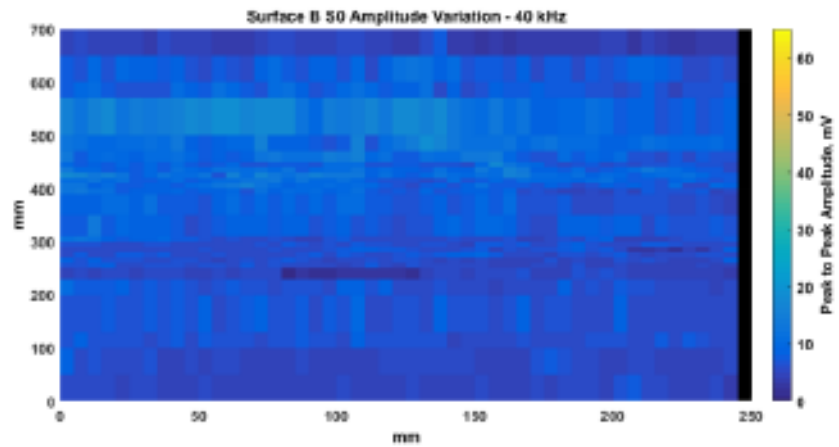
7. The final step consists in selecting test parameters, such as the averages, type of filters, sample frequency, resolution, source of the trigger and the type of Vibrometer controller.

Appendix B - MFC frequency response for $[0/90]_{16}$ GFRP circular plates



Appendix C - Images of the S_0 and A_0 modes interacting with the delamination from Surface B

Damage detection and excitation frequency 40kHz and 80 kHz: Surface B (furthest to delamination) - The S_0 mode



Damage detection and excitation frequency 40kHz and 80 kHz: Surface B (furthest to delamination) - The A_0 mode

